Measuring local properties of a Fermi gas in the BCS-BEC crossover

by

Tara E. Drake

B.S. Physics, University of Delaware, 2008

B.A. Music, University of Delaware, 2008

A thesis submitted to the

Faculty of the Graduate School of the

University of Colorado in partial fulfillment

of the requirements for the degree of

Doctor of Philosophy

Department of Physics

2015

This thesis entitled:
Measuring local properties of a Fermi gas in the BCS-BEC crossover
written by Tara E. Drake
has been approved for the Department of Physics

_____

Prof. Deborah Jin

_____

Prof. Eric Cornell

Date _____

The final copy of this thesis has been examined by the signatories, and we find that both the content and the form meet acceptable presentation standards of scholarly work in the above mentioned discipline.

Drake, Tara E. (PhD, Physics)

Measuring local properties of a Fermi gas in the BCS-BEC crossover

Thesis directed by Prof. Deborah Jin

This thesis presents experiments probing the physics of strongly interacting fermionic atoms in the BCS-BEC crossover. Ultracold atom experiments bring the ability to arbitrarily tune interatomic interactions, which allows for unprecedented access to the regime of strongly interacting physics. The majority of cold atom experiments, however, are carried out in an atom trap that imprints an inhomogeneous density on the cloud of atoms. Many phenomena, especially the signatures of phase transitions, are significantly modified by this non-uniform density. In this thesis, I present a novel imaging technique that allows us to probe a region of nearly homogeneous density within a larger, inhomogenenous cloud. Using this technique, I present new results for strongly interacting fermionic atoms, including the first measurements of the contact and the occupied spectral function of a homogeneous Fermi gas, and the first direct observation of the "textbook" momentum distribution of an ideal Fermi gas.

Dedication

For James, Marty, and Joe.

Acknowledgements

Nearly all of the work presented in this thesis was carried out by myself and two amazing physicists, graduate student Rabin Paudel and post doc Yoav Sagi. Rabin is possibly the most hardworking and the most patient person I know, and he has been an ideal co-worker. I truly could ask for no one better, and it will be difficult to begin on another project without him. Yoav brought his intelligence and inspiration to our group and kept us motivated through many difficulties. It was his vision that guided much of the work presented here, and we could not have accomplished what we did without him. I was incredibly lucky to have these two as labmates.

There have been several other graduate students with whom I have worked during my time at JILA. John Gaebler and Jayson Stewart were the graduate students on my project when I joined, and it was their idea that lead to our spatially selective imaging technique presented in this thesis. Roman Chapurin has been working with us for the last three years and will be taking the first experiments with the new apparatus. Ruth Bloom and Phil Makotyn, who both joined the Jin-Cornell group when I did, gave me their support and friendship during our mutual time here.

Debbie Jin has taught me a lot about being a scientist—how to get to the heart of a problem, when data has promise and when to change your approach, how to communicate my ideas and how to get others to communicate theirs. She has always pushed for the best I can give her, and I feel that all aspects of my work and career are better for her guidance.

Eric Cornell often acts as a second advisor for Debbie's students, and I am incredibly grateful for his presence. His understanding of complex phenomena in terms of simple physical pictures and his unshakable kindness make him the kind of physicist and person I would like to be.

Matt DeCamp was my advisor during undergrad and was the person to introduce me to experimental physics. I owe him thanks for his patience and infectious enthusiasm and for greatly influencing the decision to make physics my career.

Without Krista Beck, many of the graduate students in the Jin-Cornell group would be lost (or in some cases, stranded at DIA). She consistently lends us her help, from taking care of travel and scheduling to keeping us fed and caffeinated.

Lastly and never least, the electronic shop, computer, and machine shop staff at JILA are the life support system of the experiments here. I feel they deserve particular credit in the case of my lab, which seemed to need emergency resuscitation more than most. They saw us through a disaster involving the complete reconstruction of our electronics systems (special thanks to James Fung-A-Fat!), a mess of computer issues (thanks JR Raith and Jim McKown!), and finally the disassembly of our old apparatus and the construction of a new one (thanks especially to Hans Green, who helped us make our new sources, set up the new experiment, and coordinate our move!). Thanks also go to Beth Kroger, who, regardless of whether or not it was her responsibility, was always ready to solve our problems and go to bat for us.

Contents

Chapter

Chapter 1

Introduction

This thesis tells the story of recent work at JILA in the field of ultracold Fermi gases. The ability to create and study degenerate Fermi gases of atoms is less than two decades old, and in that time research in this area has grown from a small offshoot of the larger field of Bose-Einstein condensates to a huge community comprised of many groups around the world. Studying these gases gives us important insights into the basic quantum nature of matter, and the precision and controllability offered by ultracold gas experiments makes them very well suited for studying fundamental questions. In particular, the ability to arbitrarily tune interactions between particles allows unprecedented access to the regime of strongly correlated physics.

Even after a decade of research using ultracold strongly interacting Fermi gases and nearly a century of theoretical and experimental investigations of strongly correlated matter, there are basic questions about the nature of systems of strongly interacting particles that remain unresolved. This is due in part to the incredible richness and complexity of strongly correlated materials. In addition, many strongly correlated systems are notoriously difficult to control or access; a neutron star, for example, has this problem. Moreover, theoretical description of such complicated systems is a very challenging undertaking.

The community of ultracold Fermi gas experiments attempting to answer these questions has grown exponentially in the last few years and now includes more than 50 experiments worldwide. When I joined the JILA group in 2008, the technique of rf photoemission spectroscopy in ultracold atoms had just been developed [1]. The next year, Tan's Contact was introduced in the context of

ultracold atoms [2, 3], and in the year after, the equation of state of a strongly interacting Fermi gas was first measured [4, 5]. In the intervening time, new experiments around the world starting probing Fermi gases in novel geometries and using exotic atomic species [6, 7, 8]. This thesis covers a very small part of the progress in understanding the fundamental physics of strongly interacting fermions.

1.1   Strongly correlated fermions

1.1.1   Context: the nature of matter

All known particles can be divided into two groups based on their intrinsic total spin. Particles with integer spin (including zero spin) are classified as bosons and are generally the carriers of forces; they include the photon, which carries the electromagnetic force, the phonon, which quantizes motion, and the Higgs boson, which is linked to mass and the gravitational force. Particles with half-integer spin are classified as fermions. Electrons, protons, and neutrons, which are the constituents of visible matter, are all fermions.

The basic behavioral difference between fermions and bosons comes from the symmetry of their respective wavefunctions and is most easily seen in the character of their respective ground states. Identical bosons have wavefunctions that are symmetric under two-particle exchange, meaning that the total wavefunction will not change if any two bosons swap states. This has the effect that, at very low temperature, all bosons in a system of identical bosons will occupy the same energy state, which results in a "macroscopic wavefunction" of many particles called a Bose-Einstein condensate (BEC) (shown in figure 1.1a). Identical fermions, however, must form wavefunctions that are antisymmetric under exchange, and therefore no two identical fermions can share an energy state. At zero temperature, N identical fermions will occupy the N lowest energy states of the system, one fermion per state. The energy of the highest occupied state is called the Fermi energy (E_F) (shown in figure 1.1b). This fundamental difference between bosons and fermions underlies and explains many familiar physical phenomena—for instance, why electrons (fermions) in atoms
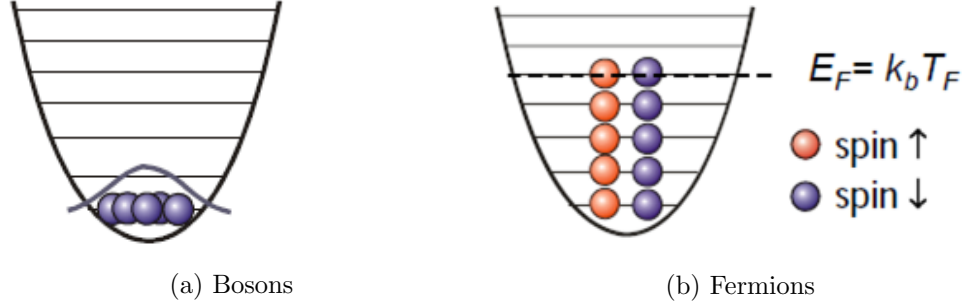
(a) Bosons   (b) Fermions

Figure 1.1: **The zero temperature ground states of bosons and fermions in a one-dimensional harmonic potential.** (a)The ground state of identical bosons is a macroscopically occupied single-particle wavefunction—a BEC. (b)N identical fermions in their ground state will occupy the N lowest energy states, one per state. Only distinguishable fermions can occupy the same state at the same time.

occupy multiple energy orbitals, resulting in the diversity of elements found in the periodic table, and why photons (bosons) can form massively occupied coherent states, as seen in lasers.

1.1.2   Interacting fermions in the wild

While the physics of non-interacting (ideal) fermions is well understood, "exotic" matter with interesting and useful properties often consists of fermions with very strong interparticle interactions. Strongly interacting fermions are crucial to our understanding of such phenomena as high temperature superconductivity, Landau Fermi liquids, and certain novel photovoltaics [9]. Fermions with very strong interactions are also the constituents of astrophysical phenomena such as neutron stars, the high density remnants of supernovae, and the quark-gluon plasma, which is the predicted state of matter in the universe after the Big Bang and just before the formation of protons and neutrons.

The direct study of many of these exotic systems is very challenging. Neutron stars are remote and not subject to scientific manipulation. Quark-gluon plasmas have been achieved in the Brookhaven Relativistic Heavy Ion Collider (RHIC) [10], but the short lifetime of the plasma and the lack of many available probes present challenges to understanding these plasmas. Even high–T_C superconductors, for which a large pool of experimental data has been collected since their

discovery in 1986, are very complex materials with multiple and possibly competing phases and non-trivial geometry, which makes identifying the underlying physics difficult [11, 12].

Theoretical description of fermions with very strong interactions also faces many challenges. While perturbative approaches have been shown to work very well for weak interparticle interactions, sufficiently strong interactions (as in the above phenomena) require a non-perturbative many-body approach. In some cases, a phenomenological theory that maps the complex, strongly interacting system onto a simpler system can be successful, such as Landau's Fermi liquid theory. However, in many cases, even a phenomenological understanding is elusive. For this reason, experimental measurements are very important to benchmark and guide theoretical progress.

The challenges and limitations listed above explain the need for a simple, controllable experimental system in which to investigate the behavior of strongly interacting fermions. At first, the study of cold, dilute gases of atoms may seem unrelated to the big, unanswered questions of high-T_C superconductivity and quark-gluon plasmas. It is true in many respects that relatively simple atomic physics experiments are not sufficient for gaining a complete understanding of these much more complex phenomena. However, the basic question underpinning these systems—how does an ensemble of fermions with very strong interactions behave?—remains open. Despite the simplicity and fundamental importance of the question, the answer is still a hotly contested area of debate. Experimental studies of ultracold Fermi gases are well positioned to answer this question.

1.2   Studying strong correlations in Fermi gases

The experimental realization of an ultracold Fermi gas occurred in 1999 [13], six years after the first BECs were realized in ultracold Bose gases [14, 15, 16]. Around the same time, the discovery of Fano-Feshbach resonances in atomic gases [17] added the ability to arbitrarily tune the strength and sign of the interactions between atoms. For a history of these developments in the field and particularly at JILA, one should read the PhD theses of Brian DeMarco and Cindy Regal [18, 19]. These two achievements (cooling to degeneracy and controlling interactions) were the two necessary ingredients for creating a strongly correlated, superfluid Fermi gas. The theory

that describes such a system is called the BCS-BEC crossover [20, 21, 22].

1.2.1   The BCS-BEC crossover

The ground state of interacting fermions is very different from the non-interacting case. Imagine an ensemble of fermions with an equal population of two spin states and with some interaction between fermions in the two spin states. In 1957, John Bardeen, Leon Cooper, and Bob Schrieffer ("BCS") showed that for such a system at zero temperature, even very weak attractive interactions would lead to pairing of the fermions about the Fermi surface [23]. These pairs, called, "Cooper pairs", are generally very large and loosely bound. However, their total spin is an integer value, and, being effective bosons, the pairs will condense to form a superfluid. This is the basic idea behind conventional, or BCS, superfluidity.

Starting with a BCS superfluid, imagine increasing the strength of the interactions between the two spin states. The Fermi surface will become broader, and more fermions will participate in the pairing. The pairs become more and more tightly bound, such that the pairs are more localized. For very strong interactions, the pair will become a tightly bound bosonic molecule, and the ground state of the system will be a superfluid Bose-Einstein condensate (BEC).

The BCS-BEC crossover unites these two types of superfluidity. As expressed above, the important variable for moving from a BCS superfluid of Cooper pairs to a molecular BEC is the strength of the interparticle interactions, which can be parameterized by a two-particle scattering length, a. Figure 1.2 shows the phase diagram of the BCS-BEC crossover. For all interaction strengths, the zero temperature ground state of the system is a superfluid of paired fermions. In essence, the crossover tells us that the ground state of interacting fermions is always a superfluid condensate—just like bosons!

The phase transition to a superfluid in the BCS-BEC crossover was first experimentally demonstrated in 2004 by Debbie Jin's group at JILA and again in the same year by Wolfgang Ketterle's group at MIT [25, 26]. Scientists working with ^{40}K at JILA and ^{6}Li at MIT were able to cool mixtures of two spins states of their atoms while simultaneously turning on strong interactions
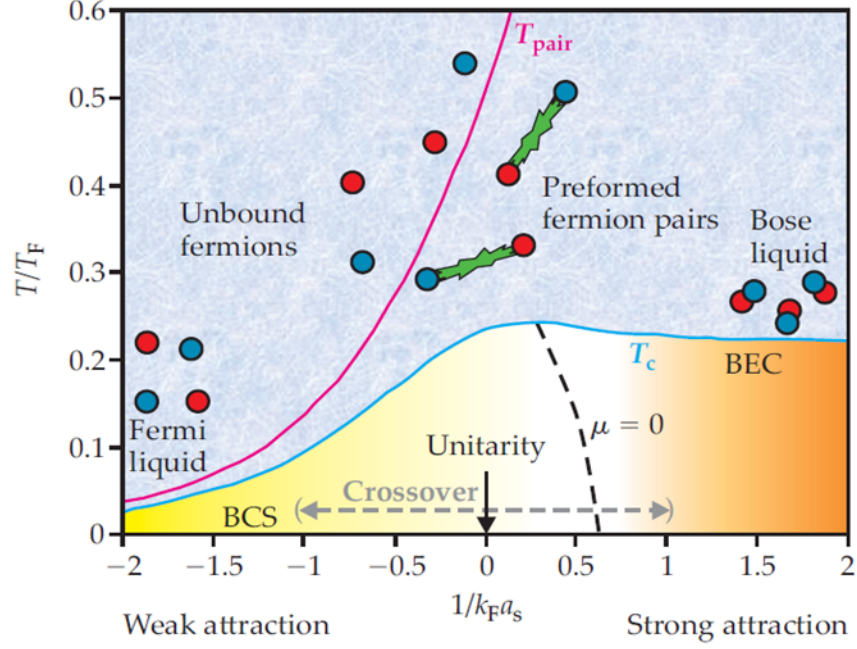
Figure 1.2: **Phase diagram of the BCS-BEC crossover, reproduced from Ref. [24].** In the leftmost (BCS) limit, the particles have a weak attractive interaction and form a superfluid of Cooper pairs below the critical temperature, T_C. In the rightmost (BEC) limit, bosonic dimers with large binding energies form above T_C and form a Bose-Einstein condensate below T_C. T_{pair} is a theoretical boundary delineating a crossover from a region of the normal phase that has pairs to a region without. The dashed $\mu = 0$ line shows the expected point at which the chemical potential crosses from positive (on the BCS side) to negative (as it is in the BEC limit).

between atoms in different spin states. An essential step forward for accessing the crossover regime was the discovery of magnetic Fano-Feshbach resonances, which allow experimentalists to use an external magnetic field to tune the scattering length that characterizes interparticle interactions to arbitrarily large values. Using these resonances, both groups were able to measure the expected superfluid phase diagram of the crossover (figure 1.3), and researchers at MIT further demonstrated superfluidity by rotating the gas and imaging vortices (figure 1.4).

The physics of the BCS-BEC crossover is universal, and should be observed in any group of strongly interacting fermions, regardless of the type of atom, or even whether the fermion is subatomic, as in the case of a neutron star, a quark-gluon plasma, or an electron in a crystal
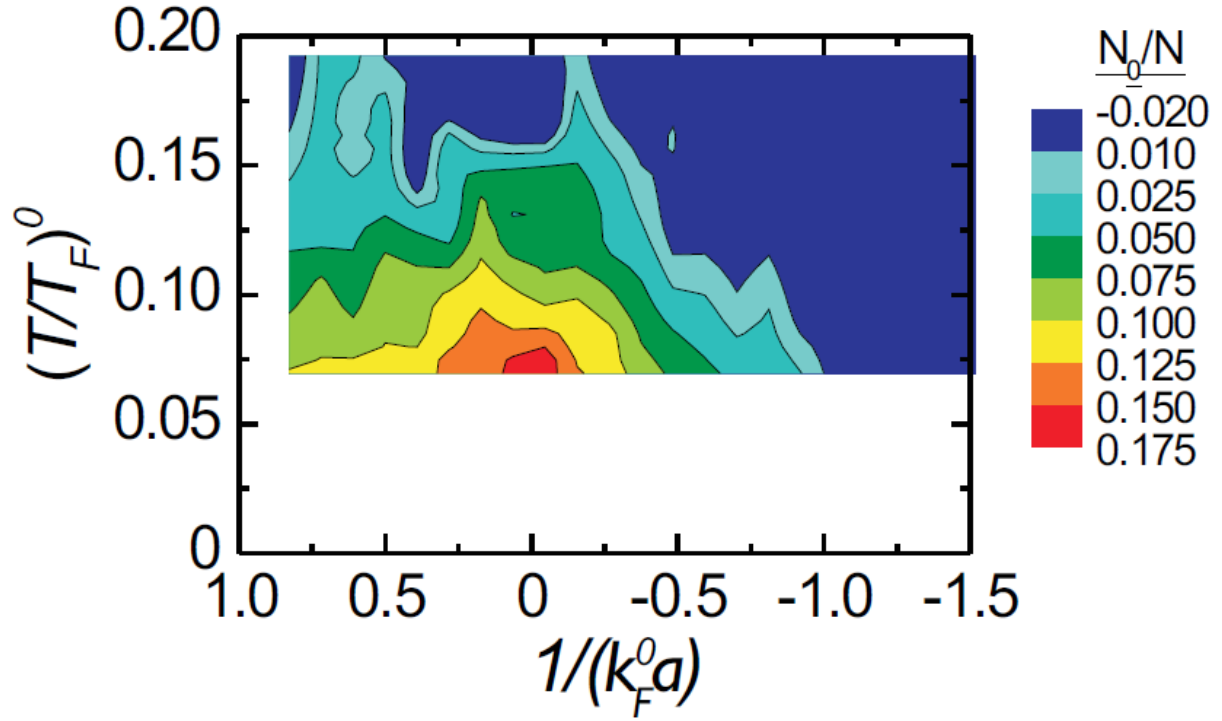
Figure 1.3: **Condensate fraction throughout the BCS-BEC crossover.** The contour plot shows the fraction of condensed atoms at various interaction strengths and temperatures. In this plot, the BCS limit is on the far right and the BEC limit is on the far left. $(T/T_F)^0$ and k_F^0 were taken from the initial conditions of the weakly interacting gas. Figure reproduced from Ref. [19].
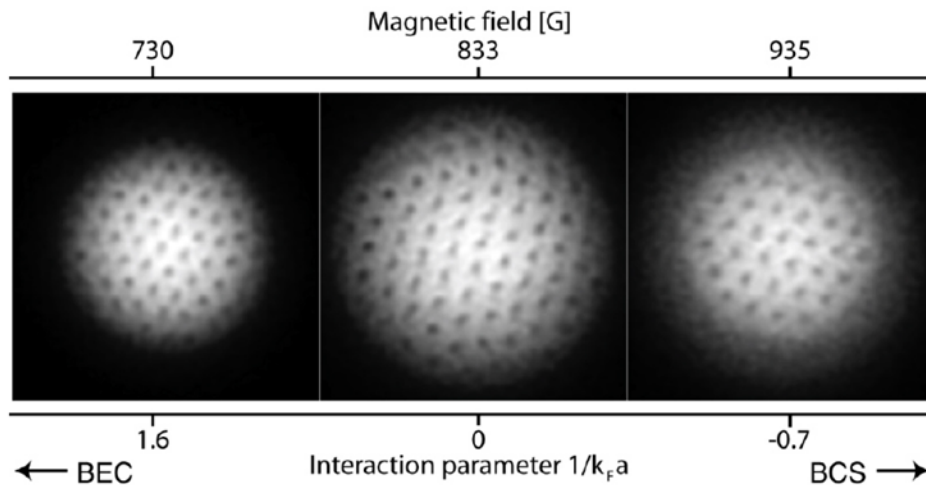
Figure 1.4: **Superfluidity seen throughout the crossover.** Reproduced from Ref. [27].

lattice [1] . The central region of the phase diagram, where $-1 \gtrsim (k_F a)^{-1} \gtrsim 1$, has the property that the two-particle scattering length, a, is as large as or larger than the average interparticle spacing, $(k_F)^{-1}$. (k_F is the Fermi wavevector and is related to the Fermi energy by $E_F = \frac{\hbar^2 k_F^2}{2m}$, where m is the atomic mass and $\hbar$ is Planck's constant.) In this region, the gas behaves much more like a liquid, exhibiting hydrodynamic flow and other collective effects of strong interactions. Gases at these scattering lengths are said to be in the "crossover regime." In this regime, the two-body scattering length is no longer sufficient to characterize the particles' behavior, and as the gas approaches $a = \infty$ ("unitarity") and zero temperature, the only relevant length scale remaining is the interparticle spacing. This regime of interactions is the most interesting for us to access, not only due to the universal behavior, but because these are the interaction strengths at which perturbation theory breaks down, and the behavior of the gas is difficult to predict. The crossover regime provides us the greatest chance to observe new physics and guide new theoretical description.

1.2.2 Our system

While the advent of hydrodynamic Fermi gases in the unitary regime has caused the original Fermi gas community to grow to include more exotic geometries and conditions, our lab has mainly stuck to the recipe originally set by the first JILA crossover studies—a gas of ^{40}K atoms in an equal mixture of two spin states with a Fano-Feshbach resonance controlling interactions. The clouds generally consist of 5–$30 * 10^4$ atoms at 0.1–$0.5 T_F$. The atoms are trapped in a 3D geometry using a crossed-beam optical dipole trap, and the final cloud has a cigar shape with a roughly 1:10 aspect ratio.

In order to cool the atoms to quantum degeneracy, we use a series of trapping potentials and cooling techniques. We first gather ^{40}K atoms in a magneto-optical trap using the LVIS loading technique developed at JILA [28]. We then load the atoms into a Ioffe-Pritchard magnetic trap in a cloverleaf configuration. We evaporatively cool in this trap by using a single microwave frequency

---

[1] The key assumption for this universality is that the scattering length, a, is much larger than the range of the physical interaction. For atoms, this requirement means that a should be much larger than the van der Waals length, r_0. For ^{40}K, $r_0 = 60$ Bohr radii, which is much smaller than a at the interaction strengths we investigate.

to remove the hottest atoms from the trap and letting the remaining atoms re-thermalize. When the atom gas temperature has reached about 6 μK, we load the atoms into the optical dipole trap, where the final evaporation occurs. The final temperatures reached are generally at or below 100 nK. Further details about the construction of the apparatus and about the magnetic trap are found in Brian DeMarcos thesis [18].

During the final stages of cooling in the dipole trap, we apply a uniform bias magnetic field to the atoms to bring them close to a Fano-Feshbach resonance. This both allows us to improve evaporation at the coldest temperatures and to set the interactions between the atoms when we perform our science, which gives us access to the crossover regime. The resonance for ^{40}K occurs at 202.2 G. It enhances interactions between two Zeeman states, $|F, m_F\rangle = |9/2, -9/2\rangle$ and $|F, m_F\rangle = |9/2, -/2\rangle$, where F is the total atomic spin, $F = 9/2$ is the lowest hyperfine state, and m_F is the projection onto the axis of the magnetic bias field. Loading into an optical dipole trap (as opposed to staying in a magnetic trap) allows us to prepare our atoms in these two spin states, which are not magnetically trappable. For more details about our optical dipole trap and the ^{40}K Fano-Feshbach resonance, see the theses of Cindy Regal and Jayson Stewart [19, 29].

1.2.3   Density inhomogeneity: an advantage or a disadvantage?

Confining atoms in a potential well is a necessary step to carrying out BCS-BEC crossover experiments (and many others types of atomic physics experiments as well). The most commonly used atom traps, whether magnetic, optical, or both, create a potential that approximates that of a harmonic oscillator. These bowl-shaped potentials allow for the high densities (10^{12} atoms per cm^3—"high" for a quantum gas) needed for the quantum degenerate regime. In such a potential, the spatial extent of the trapped gas depends on its total energy, with more energetic atoms traveling farther from the center of the trap. For a Fermi gas, even a T=0 cloud will have as many occupied energy states as there are atoms, due to Fermi statistics. This means that the atoms will be distributed non-uniformly, with the highest density of atoms at the trap center and the lowest densities at the edges of the bowl. This spread of densities is always present in trapped atom

experiments to some extent.[2]

This density inhomogeneity has important consequences. The energy scale of Fermi gases is E_F, the Fermi energy. This energy is directly determined by the density:

$$E_F = \frac{\hbar^2}{2m}(6\pi^2 n) \tag{1.1}$$

where m is the mass of the atom, $\hbar$ is Planck's constant, and n is the number density of atoms in a single spin state. Several other quantities depend on the Fermi energy in turn:

$$k_F = \frac{\sqrt{2mE_F}}{\hbar^2} \tag{1.2}$$

$$T_F = \frac{E_F}{k_B} \tag{1.3}$$

where k_F and T_F are the Fermi wavevector and temperature, respectively, and k_B is the Boltzmann constant.

Since all of these quantities depend upon the local density, they vary across the atom cloud. In a harmonic trap, for example, the condition $T/T_F = T_C$ (where T_C is the critical temperature of the superfluid phase transition) will only ever be true for a single ellipsoidal, equipotential surface. The atoms enclosed by that surface will be below the transition temperature, and the atoms outside will be above.

In some cases, the spread of densities in a harmonically trapped gas can be an advantage. From one spatially resolved image of the atom cloud, one can extract measurements at many densities. This has been particularly useful in recent measurements of the equation of state [4, 35, 5, 36].

Some measurements, however, cannot differentiate between signal that comes from the more dense center of the trap or the relatively dilute edges. Measurements done after the trapping

---

[2] In 2013, a group in Cambridge trapped a BEC in a uniform optical potential, or "box trap". This technique solved the problem of density inhomogeneity and has enabled the group to measure the dynamics of the BEC phase transition with great accuracy. A box trap for fermionic Li^6 atoms has very recently been demonstrated at MIT in the group of Martin Zwierlein. [30, 31, 32, 33, 34]
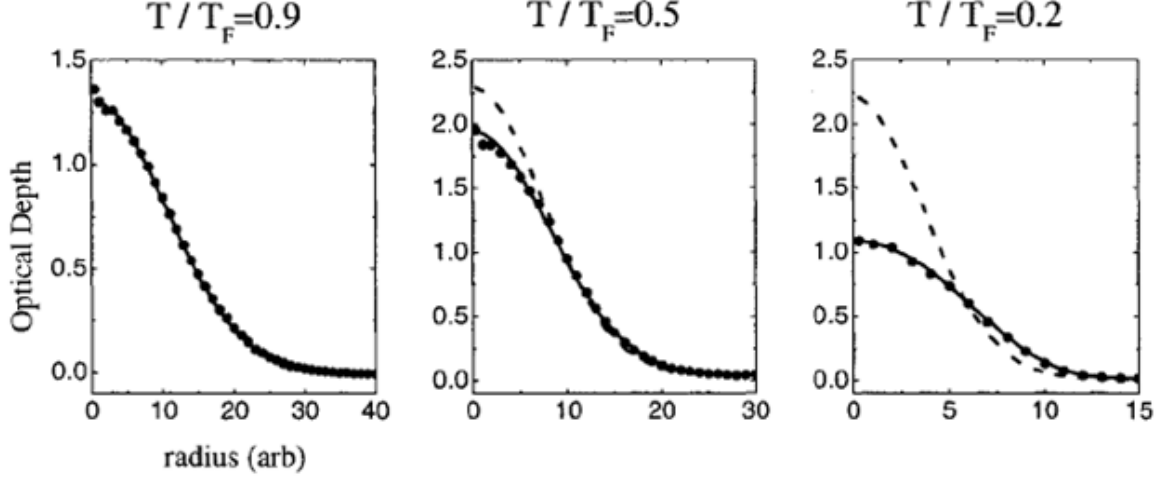
Figure 1.5: **Momentum distributions of weakly interacting fermions.** Images of fermionic atoms taken after a time of flight expansion from a harmonic trap reveal the momentum distribution. The distribution of momenta can be fit to determine T/T_F. The dashed line is the expected Boltzmann distribution for the same number of atoms. Note the lack of a sharp Fermi surface, even for the coldest clouds. Figure reproduced from Ref. [37].

potential has been turned off and the atoms have expanded for some time of flight are of this type. In this case, the quantity measured will reflect a sum over all the densities of the trap. If a sharp signal is expected at the transition temperature or at the Fermi surface, this "trap averaging" will broaden that signal, and even completely wash it out in some cases.

This effect of trap averaging has been present since the first measurements of a degenerate Fermi gas. Figure 1.5 shows the first evidence of Fermi degeneracy in ^{40}K. The expected momentum distribution for a non-interacting Fermi gas in a harmonic trap can be analytically determined as a function of T/T_F, and the data can be fit to determine the temperature. However, the spread in k_F throughout the cloud means that, instead of a sharp step the Fermi momentum, $\hbar k_F$, that gets sharper with decreasing temperature, even very cold clouds look nearly Gaussian in shape. In addition, while the momentum distribution of a non-interacting gas can be calculated, the momentum distribution of a Fermi gas with interactions is still an open question. In the case of the strongly interacting Fermi gas, recovering features washed out by trap averaging can prove impossible.

1.2.4   Imaging from a uniform density sample

The experiments within this thesis all have one thing in common. In each, we have taken pains to eliminate the effects of trap averaging and extract a signal that, to a good approximation, comes from a single density.

We do this not by creating a cloud with a single density, but by altering our measurement such that we only measure a small portion of the cloud at a time. This spatial selectivity is typically performed immediately after the atoms are released from the trap and before they have had a chance to expand in time of flight. In this way, our technique allows us to perform measurements of the momentum distribution of the atoms while retaining the knowledge of where in the trap the signal came from.

1.3   Contents

In this thesis, I will explain the work our group has done since developing spatially selective imaging. In some sense, the experiments presented here have largely already been carried out without the benefit of spatial selectivity. For each experiment, however, I will attempt to show how measuring a single density has enhanced our understanding of the physics of interacting fermions and uncovered new behavior that had been buried by trap-averaging.

In chapter two, I will present the spatially selective imaging technique. In chapter three, I will present the first experiments using spatially selective imaging, in which we probed an ideal Fermi gas and saw, for the first time, a sharp step in the momentum distribution of the gas. This chapter will also contain much of the work the we did to characterize this technique, which relied upon our knowledge of the form of the momentum distribution of a non-interacting gas. Chapter four presents measurements of the contact of a homogeneous Fermi gas at unitarity, including a few interpretations of the contact and why probing a single density is of particular importance for this measurement.

The next two chapters will focus on measurements of the occupied spectral function of a

strongly interacting Fermi gas using atom photoemission spectroscopy, which has been the largest focus of my PhD work. In chapter five, I will present the work we've done investigating the normal phase of the gas in the BCS-BEC crossover by preparing a gas just above T_C and varying the interaction strength. This chapter will also include a small introduction to crossover physics and a description of the interest and controversy surrounding the character of the normal phase. Chapter six will discuss our preliminary investigations focusing on how the spectral function of a normal phase gas changes with temperature.

Chapter 2

Spatially selective imaging

In this chapter, I present the details of our spatially selective imaging technique. This technique uses two Laguerre-Gaussian (LG) mode beams created from light tuned to an optical pumping transition. These ring-shaped beams are focused on our atoms along the z (axial) and y (vertical) directions and are carefully aligned such that they optically pump atoms from the low density regions at the edge of the cloud. The signal in our images comes from the atoms that were not optically pumped. These were at higher and more uniform density and can be approximated as coming from a homogeneous density gas. This technique is used in all the experiments that make up the main body of this thesis.

2.1   Laguerre-Gaussian mode beams

Laguerre-Gaussian spatial mode beams have recently been of interest to the ultracold atom community for their unique intensity and phase patterns. These beams have an intensity of zero at their center and are often called "donut" mode beams for their ring-shaped cross section. (Around the lab, we refer to our spatially selective imaging as the "donut beam technique", and in this thesis, I'll use these interchangeably.) This shape comes from a non-zero orbital angular momentum $l\hbar$, which is separate from the spin (polarization) of the photons and which results in a phase winding around the donut.

At the focus, the light intensity of a Laguerre-Gaussian mode beam with angular momentum

index, l, is given by

$$I(r) = \frac{2}{\pi l!} \frac{P}{w^2} \left(\frac{2r^2}{w^2} \right)^l e^{-\frac{2r^2}{w^2}} \tag{2.1}$$

where P is the total optical power, r is the radial coordinate transverse to the direction of beam propagation, and w is the waist. (LG beams can also have more than one radial node, which results in a spatial mode with several concentric rings. The number of radial nodes is given by a radial index, p. In equation 2.1, $p = 0$, and the beam profile has only one ring.) LG mode beams can be generated a variety of ways, depending upon the desired efficiency and mode purity [38, 39, 40, 41, 30].

We found that printing an absorptive diffraction pattern in chromium onto a glass slide was a cheap and quick solution that produced acceptable beams for our purpose. Figure 2.1 shows 3 such gratings and images of the resulting beams. The gratings show 1, 2, or 3 forked dislocations in the center of the pattern, which produce beams with an angular index of $l = 1$, 2, or 3, respectively. After printing, the width of a black line in each grating is 75 μm, and the total pattern extends over a 1 inch circular slide. A collimated laser beam, which is much smaller than the slide, is centered on the dislocation, and the diffracted order is imaged (bottom row in figure 2.1). [1]

2.2 Experimental setup of LG mode beams

Our spatially selective imaging technique involves the use of two donut-mode beams carefully focused and aligned onto our atoms. These beams are each created with a grating with angular index of $l = 2$. One beam is sent along the vertical (y) axis and another along the horizontal axis along the long direction of the optical trap (z-axis) (see figure 2.2). Both donut-mode beams propagate along the same axes as the 1064 nm optical trapping beams, and they are focused onto the atoms using the same lenses that focus the trapping beams. Figure 2.3 shows the path of the horizontal donut beam as it is first collimated to a 5.5 mm diameter waist, sent through the grating,

---

[1] It is important to note that, for our purposes, we care only about the intensity of the LG mode beam near its center—specifically that the intensity in the center reaches zero and that the "inner walls" of the beam follow equation 2.1. We do not care much about the phase properties or the mode purity beyond this, and one can see in figure 2.1 that we generate a small amount of intensity in $p \neq 0$ modes, leading to faint outer rings around the main ring.

$l = 1$ $l = 2$ $l = 3$
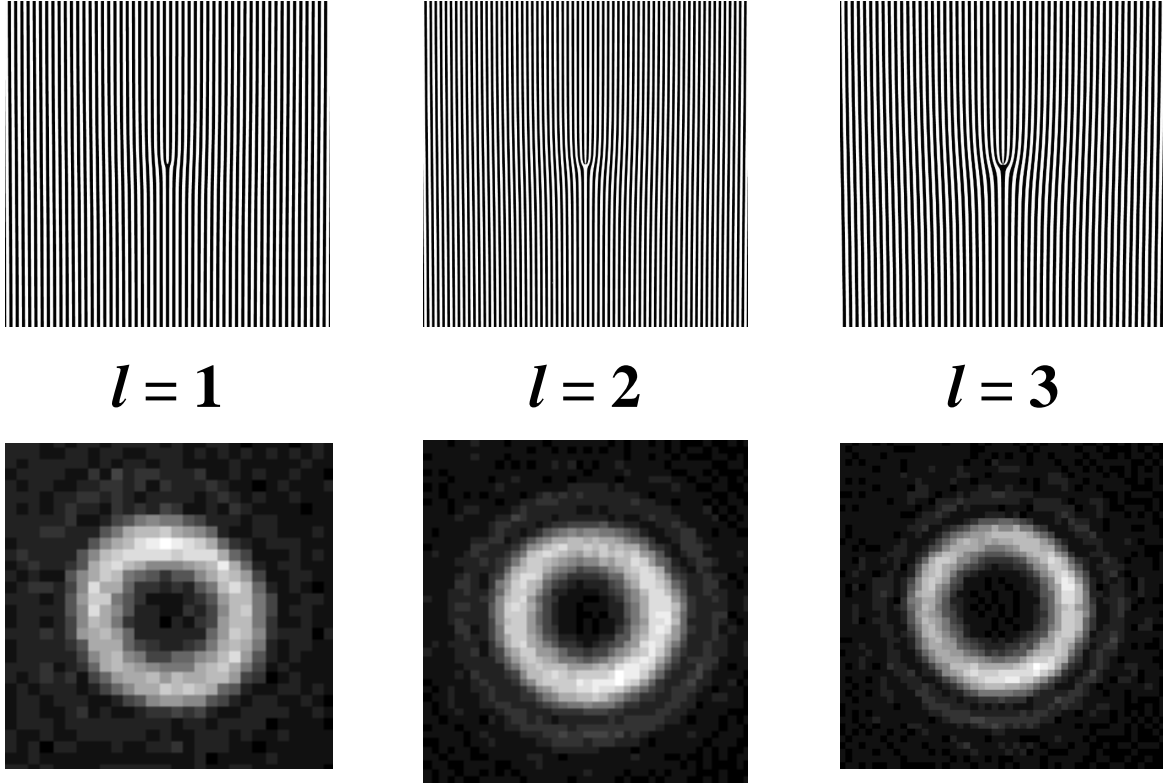
Figure 2.1: **Forked diffraction gratings.** These gratings have central dislocations that determine the angular index, l, of the Laguerre-Gaussian beam they create. The patterns on the top row were printed on glass slides, and the bottom row shows the resulting far field diffraction for each. Note that the LG beams with higher l have larger central holes with sharper inner edges.

reflected off a mirror with motorized control, and combined with the horizontal optical trap path using a dichroic slide. This beam is focused onto our atoms using a 200 mm lens. The vertical donut beam is similarly collimated, sent through a grating, focused on the atoms using a 250 mm lens, and then combined with the vertical optical trapping beam via a polarizing beamsplitter cube. The vertical donut beam is aligned onto the atoms by hand rather than by motorized micrometers, but we have found that the alignment of this beam is stable for months, while the horizontal donut beam must have its alignment checked before and after each data set. (A typical data set takes 2.5 hours.)
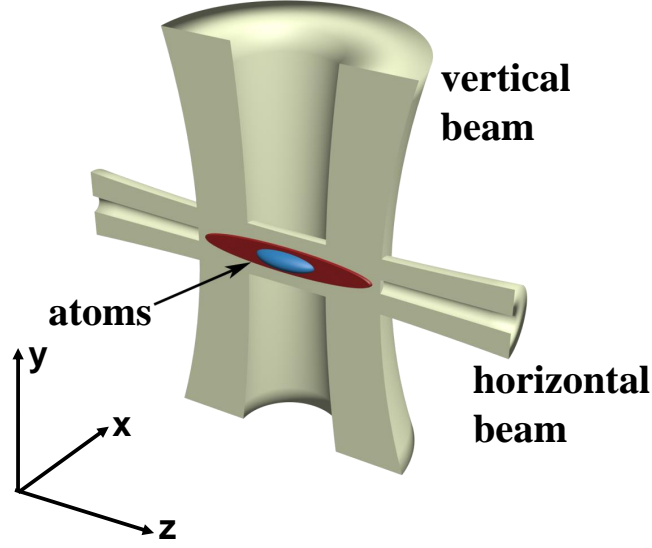
Figure 2.2: **Illustration of the two intersecting hollow light beams used to optically pump atoms at the edges of the trapped atom cloud.**

2.3 Optical pumping transitions

The spatially selective imaging technique works by optically pumping the edges of the atom cloud into a state invisible to our imaging such that only the central atoms at relatively uniform density are imaged.[2] The atoms that are optically pumped are shelved in the F = 7/2 hyperfine manifold during imaging, and only the atoms that remain in their original state in the F = 9/2 manifold are imaged. We have two optical pumping transitions that we generally use, depending on the initial state of the atoms and the choice of experiment.

Figure 2.4 shows the two optical pumping transitions utilized in this thesis. Transition **a**, used for the Fermi surface and homogeneous contact experiments (chapters 3 and 4), pumps atoms from the $|F, m_F\rangle = |9/2, -7/2\rangle$ hyperfine ground state to the $|F', m_F\rangle = |5/2, -5/2\rangle$ excited state. Transition **b** is used for photoemission spectroscopy experiments (chapters 5 and 6) and pumps

---

[2] The technique of using shaped optical pumping beams to select atoms for imaging has been used previously. For an example, see Ref. [42].
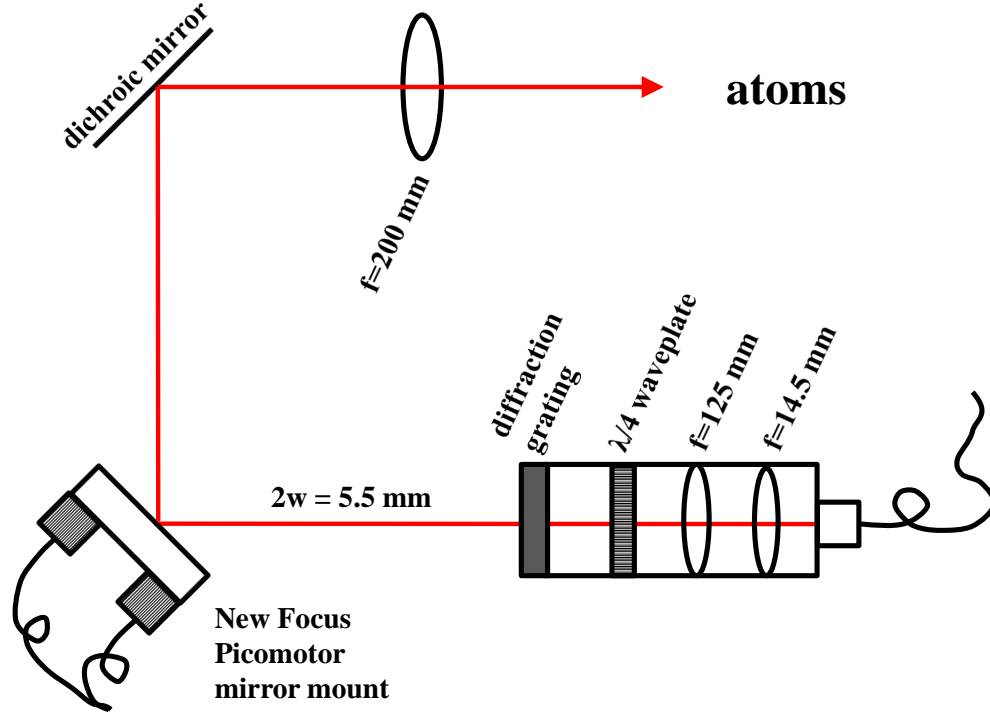
Figure 2.3: **Setup of the horizontal donut beam.** The horizontal donut-mode beam (propagating along the z-direction) is collimated to a 5.5 mm diameter before it is sent through a forked diffraction grating that gives the beam an $l = 2$ Laguerre-Gaussian mode in the far field.
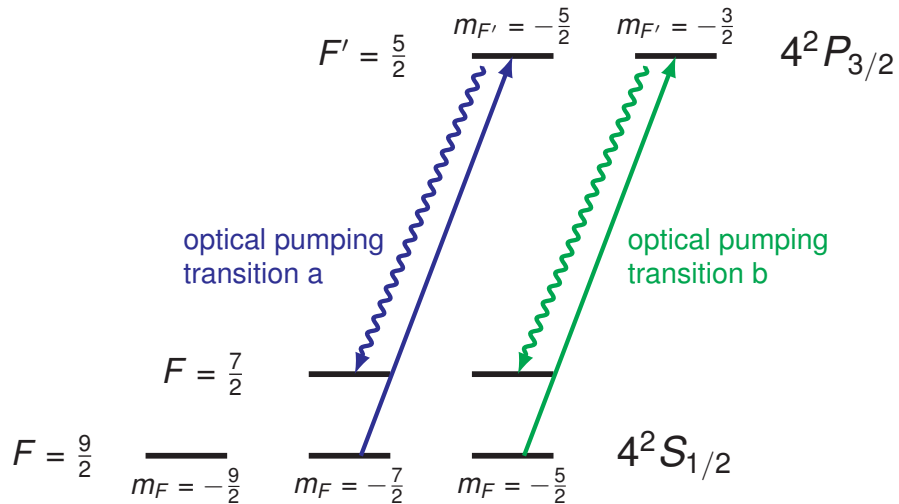
Figure 2.4: **Optical pumping transitions.** The straight lines indicate the two optical pumping transitions used in the donut beam technique. The squiggly lines indicate the most likely spontaneous decay path of an optically pumped atom.

atoms from the $|F, m_F\rangle = |9/2, -5/2\rangle$ hyperfine ground state to the $|F', m_F\rangle = |5/2, -3/2\rangle$ excited state. Further characterization of the details these two transitions, including the chance of an atom to return to the imaging state and the possibility of colliding with an optically pumped atom, are investigated at the end of chapter 3.

2.4   Fitting the LG mode beams
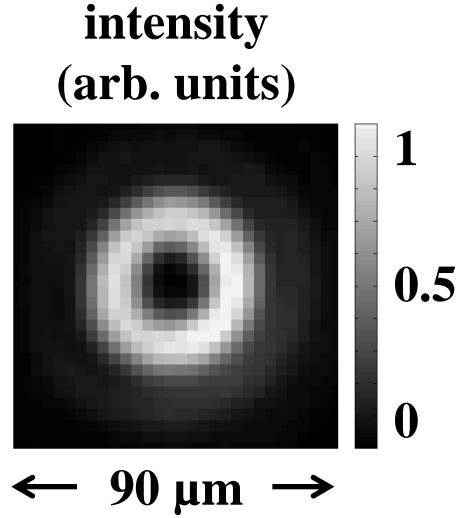
Figure 2.5: **Image of the horizontal donut beam at the atoms.**

As part of characterizing our LG beams, we image the beams at their focus, where they overlap with the atom cloud. The horizontal LG beam propagates along an imaging axis, so it is easy for us to image the beam at the atoms using the camera and imaging system already in place. Figure 2.5 shows a 2D cross section of the horizontal LG beam at the atoms. By fitting to find the center of the beam and finding the distance of each pixel from that center, we construct a profile of the intensity, $I(r)$, which can be fit to equation 2.1 (see figure 2.6). From this fit, we see that the horizontal LG beam is well approximated by an $l = 2$ mode beam with a waist of $w = 16.8\mu$m.

We also found the waist of the donut beam propagating in the vertical direction. Unlike the horizontal donut beam, the vertical donut beam removes signal along only the one axis (the z-axis, along which the cloud is longest). In other words, the vertical donut can be approximated
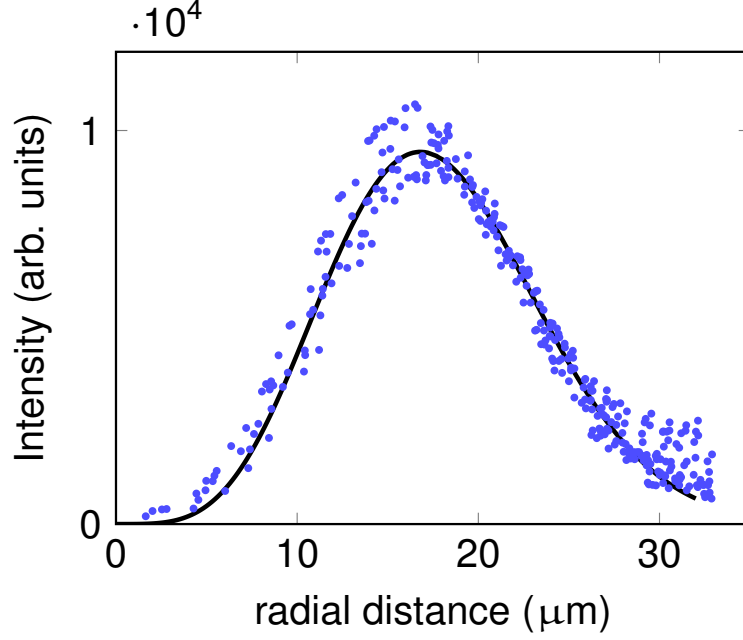
Figure 2.6: **Fitting the horizontal donut beam.**

by a one dimensional intensity profile, I(z), with two peaks of high intensity and a center going to zero intensity. (The horizontal beam is, in contrast, modeled as I(x,y).) We imaged the focus of the vertical donut beam using a beam profiling camera from DataRay Inc. (figure 2.7). Noticing that the beam was slightly elliptical and wanting to know the I(z) seen by the atoms (which was difficult to determine from our setup), we found the principal axes of the beam and plotted the perpendicular cross sections. Figure 2.8 shows the two perpendicular cross sections of the vertical donut beam. Both cross sections were fit to an $l = 2$ mode beam, and they returned waists of $w = 186\mu$m and $w = 151\mu$m, giving us lower and upper limits for the size of the vertical donut at the atoms.

We then decided to use our atoms themselves to measure the vertical donut size. Looking along the x-direction (perpendicular to the long direction of the trap), we took an image of the atoms in the trap with and without removing signal using the vertical donut (figure 2.9a). Summing along the y-direction, we calculated the removal as a function of z:

$$\text{Fraction of atoms not optically pumped(z)} = \frac{\text{Atoms imaged after pumping(z)}}{\text{Atoms imaged before pumping(z)}} \qquad (2.2)$$
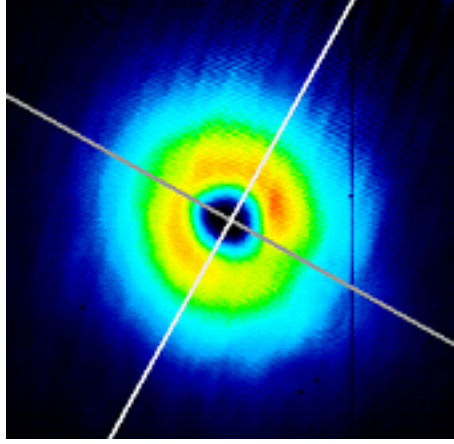
Figure 2.7: **Image of the vertical donut beam.** The cross hairs indicate the principal axes of the image and correspond to the two cross sections shown in figure 2.8. The line which is closer to horizontal corresponds to figure 2.8b, which we found the oriented along the z axis of the trap. The other cross hair is along the x axis. As z is the elongated axis of our cigar-shaped trap, and as the vertical donut beam has a waist of 186 μm, this beam only removes signal along the z-direction. This image was captured using a DataRay beam profiling camera and software.

The fraction of atoms left in the signal by the vertical donut beam is shown in figure 2.9b.

To determine the size from figure 2.9, we used a very simple model of optical pumping by the donut beam. In this model, we assumed that the probability for an atom to be optically pumped was proportional to $exp[-I(z)]$, where $I(z)$ is the intensity of the vertical donut along z, given by equation 2.1. The solid black line in figure 2.9b shows the expected fraction of atoms that remain in the imaging state based on this model. For this calculation, we use the measured profile of the atoms without optical pumping (figure 2.9) and subject them to removal by an $l = 2$ LG beam with a 186 μm waist. We see that this simple model reproduces the probability of the atoms to remain in the imaging state quite well, apart from a slight asymmetry on the right side of figure 2.9b. We believe that this asymmetry comes from a similar asymmetry in the vertical donut beam, seen in the inset of figure 2.8b. We do not expect a feature of this size to have much effect on the final measurements of the gas using the donut technique.
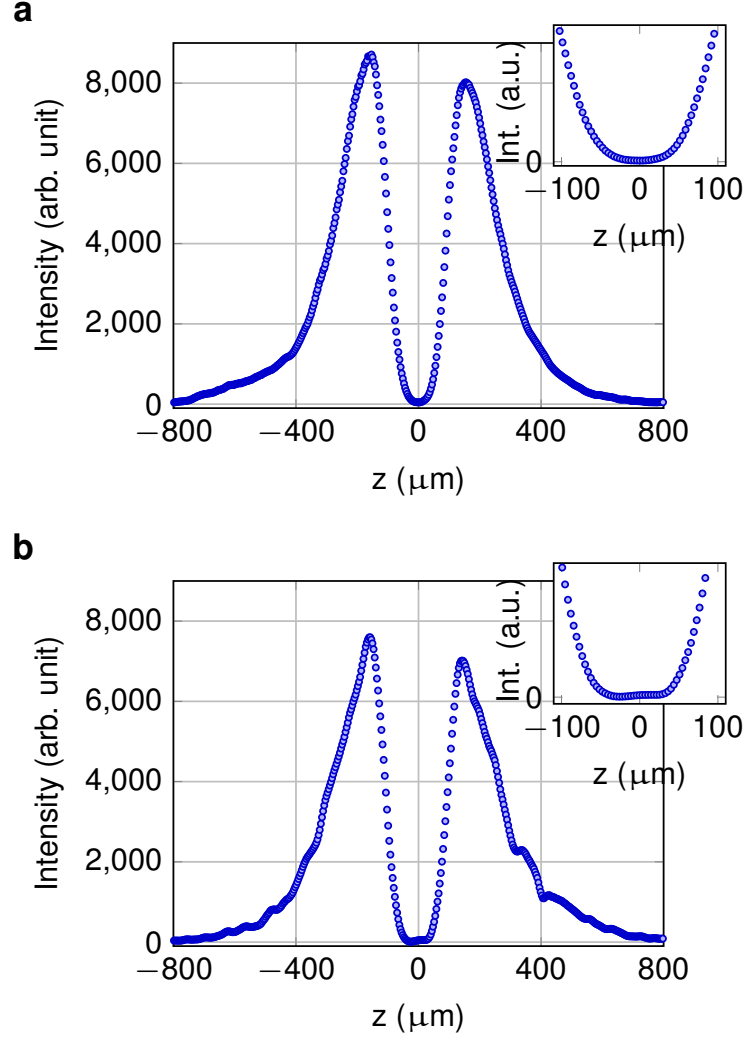
Figure 2.8: **Cross sections of the vertical donut beam.** These cross sections correspond to the crosshairs in figure 2.7. The insets zoom in on the zero intensity center of the beam. The inset of **a** was fit to an $l = 2$ LG beam with waist $w = 151\mu$m, and the inset of **b** fits to an $l = 2$ LG beam with waist $w = 186\mu$m. From our measured removal of signal in our atom cloud, we find that the atoms see an intensity profile closer to **b** (see figure2.9).

2.5   Aligning the LG beams onto the atom cloud

Properly aligning the donut-mode beams onto the atom cloud has two stages. For rough alignment, we image the cloud of atoms after optically pumping away signal with only one beam to make sure that the center of the cloud is in the same position and has the same optical depth (OD) as it does before signal is removed. As the donut beam is moved across the cloud, the number of
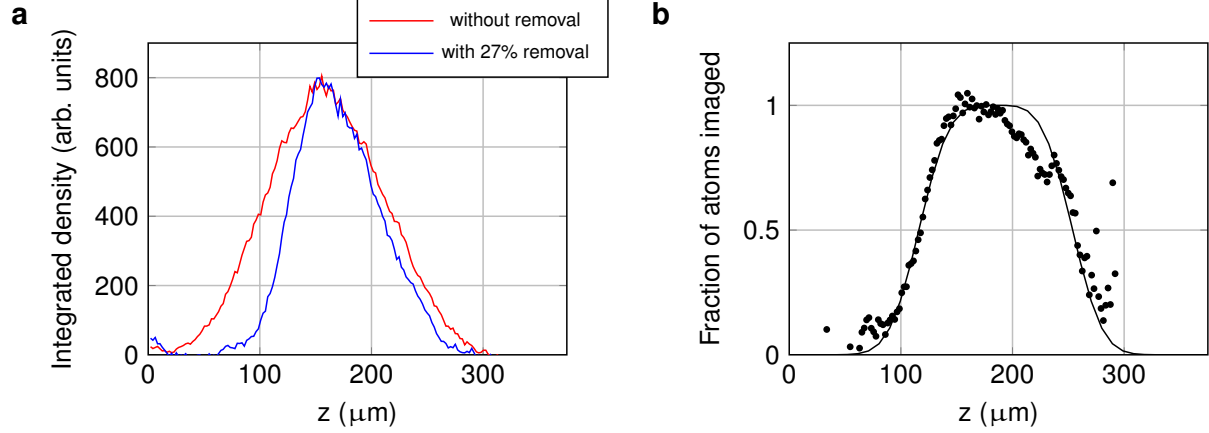
Figure 2.9: **The removal of signal by the vertical donut beam. a.** Density profiles before and after application of the vertical donut beam. Note that the number of atoms imaged in the center is unchanged, with signal only being removed from the cloud's edges. This shows good alignment of the donut beam onto the atoms. **b.** The fraction atoms remaining in the signal is shown as a function of z (dots). This is compared to a very simple model predicting the amount of removal from an $l = 2$ LG beam with a waist of 186 μm (black solid line). This model fits the data well. The slight asymmetry in the removal seen on the upper right side of the data comes from a slight asymmetry in the donut beam profile itself, just visible in figure 2.8b. This is further evidence that the cross section fit by a 186 μm waist corresponds to the correct intensity profile seen by our atoms.
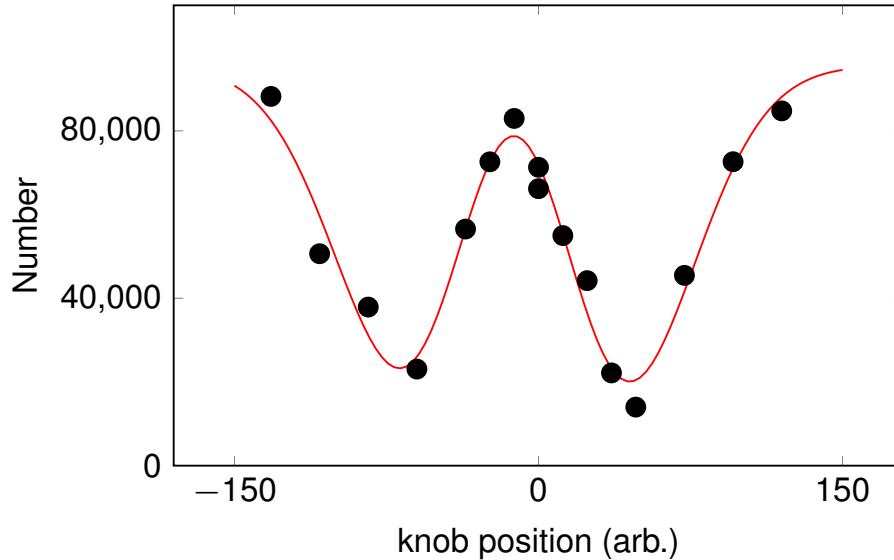
Figure 2.10: **Moving the donut beam across the atoms.** Here, we shift the position of the horizontal donut beam with respect to the cloud and measure how many atoms remain in the imaging state. We see two dips in atom number, corresponding to positions when either side of the "donut" crosses through the center of the trap. The beam is best aligned somewhere between these two dips, when the center of the atom cloud sits in the center of the LG beam.

atoms not optically pumped should have a "W" pattern, where the best alignment is found in the center of the W (figure 2.10).

Once we have established a rough alignment, we use the pendulum-like motion of atoms in the harmonic trap for fine alignment. By optically pumping at some time, t, before the trap is turned off, we can look for a "slosh" in the atoms that remain. This is not truly a slosh, as we have not given the atoms a directional kick; instead, it comes from the usual motion of atoms in a harmonic trap—atoms away from the center of the trap feel a restoring force towards the center. If the beam is selecting atoms at the edge of the trap, we measure a large oscillation in their center positions, but if the beam is perfectly centered, the center of the selected atom cloud should not change. (In either case, we also see a "breathe" in the atoms' width at twice the frequency.) We have found that aligning the horizontal (vertical) beam to minimize the center-of-mass motion in the radial (axial) direction results in very precise alignment. In addition, we often use this technique to measure the frequencies of the trap, as it is the most non-perturbative way we have found to do so. Figure 2.11 shows one such frequency measurement taken during donut alignment.

2.6   Summary

In terms of new experimental techniques, the spatially selective imaging was fairly simple to set up. A minimal number of optics were added to the system, the optical pumping frequencies were chosen, the shapes of the donut-mode beams were characterized, and the beams were carefully aligned onto the atoms.

In the next chapter, I present our first experiment with spatially selective imaging—the direct observation of the momentum distribution of a non-interacting Fermi gas. The rest of the characterization of the "donut beam technique" is discussed in the context of this experiment, including the possibility of collisions with optically pumped atoms, the validity of assuming our measurements are taken at a single density, and the development of a robust model for the removal of signal using this technique.

a

b
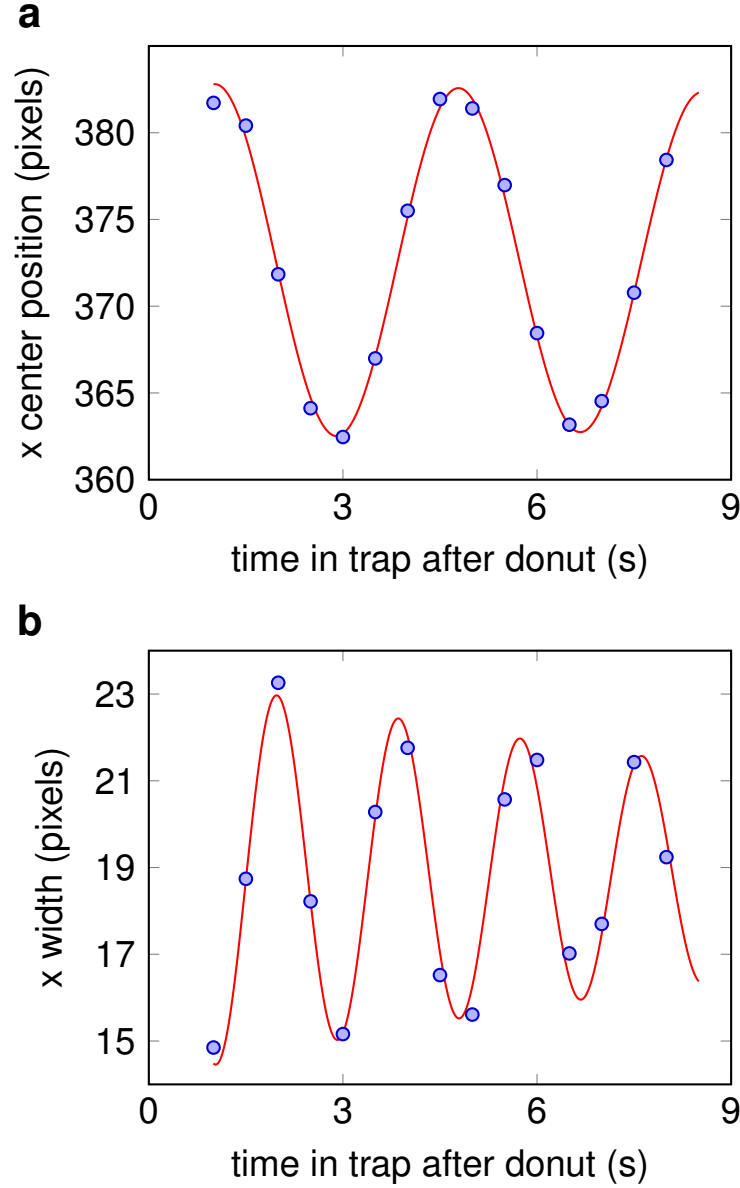
Figure 2.11: **Donut alignment technique. a.** When a hollow light beam is slightly misaligned from the center of the atoms, we observe a small center of mass oscillation in the visible sample as a function of time held in the trap after optical pumping. As a final alignment step, we minimize this oscillation. We have also found this to be a good way to measure the trapping frequency. In these data, we find the trapping frequency to be 266(2) Hz in the x-direction. **b.** We measure the width of the atom cloud in time of flight after some time held in the trap. We observe the in-trap pendulum-like oscillations of the atoms as they exchange potential and kinetic energy. This "breathe" oscillation occurs at twice the trapping frequency and is present even for a perfectly aligned beam.

Chapter 3

The ideal homogeneous gas: uncovering the Fermi step function

The first experiment carried out with our new spatially selective imaging technique was a measurement of the momentum distribution of an ideal (non-interacting) Fermi gas. This experiment revealed the iconic step in the momentum distribution of a degenerate Fermi gas. To our knowledge, this was the first time that the "textbook" momentum distribution of a Fermi gas was directly observed. In addition, the momentum distribution of an ideal Fermi gas is well understood, and our results allowed us to fully characterize the donut beam technique. Much of the content of this chapter was published in Ref. [43].

3.1   The momentum distribution of a homogeneous Fermi gas

The homogeneous Fermi gas is a widely used model in quantum many-body physics and is the starting point for theoretical treatment of interacting Fermi systems. The momentum distribution for an ideal Fermi gas is given by the Fermi-Dirac distribution:

$$n(k) = \frac{1}{e^{\left(\frac{\hbar^2 k^2}{2m} - \mu\right)/k_B T} + 1}, \tag{3.1}$$

where the $n(k)$ is the average occupation of a state with momentum $\hbar k$, m is the fermion mass, μ is the chemical potential, k_B is Boltzmann's constant, and T is the temperature. Surprisingly, to our knowledge, the momentum distribution of an ideal Fermi gas, with its sharp step at the Fermi momentum, $\hbar k_F$, has not previously been directly observed in experiments. One reason for this is that the vast majority of Fermi systems, such as electrons in materials, valence electrons in

atoms, and protons and/or neutrons in nuclear matter, are interacting. For ultracold atom gases, the interactions can be made very strong or very weak, and the momentum distribution can be directly probed.

3.2   Experiment sequence

We begin with a quantum degenerate gas of $N = 9 \times 10^4$ ^{40}K atoms in an equal mixture of the $|F, m_F\rangle = |9/2, -9/2\rangle$ and $|9/2, -7/2\rangle$ spin states, where F is the quantum number denoting the total atomic spin and m_F is its projection. The atoms are confined in an approximately cylindrically symmetric trap, created by two orthogonal 1075 nm beams, one with a $30\,\mu$m waist and one with a waist of $200\,\mu$m. We measure a radial trap frequency ν_r of 214 Hz and an axial trap frequency ν_z of 16 Hz. We take data at $B = 208.2$ G where the scattering length a between atoms in the $|9/2, -9/2\rangle$ and $|9/2, -7/2\rangle$ states is approximately $-30\,a_0$ [1], where a_0 is the Bohr radius. Here, the gas is very weakly interacting, with a dimensionless interaction strength of $k_F a = -0.011$.

Once we create an ideal Fermi gas, the sequence for spatial selection and probing the momentum distribution is as follows. We first turn off the trap suddenly and illuminate the atoms with the vertical donut beam, followed immediately by pulsing on the horizontal beam. The power in the beams is on the order of 10s to 100s of nW and is varied to control the fraction of atoms that are optically pumped out of the imaging state ($|9/2, -7/2\rangle$). Each beam is pulsed on for 10 to 40 μs, with the pulse durations chosen such that the fraction of atoms optically pumped by each of the two beams is roughly equal (within a factor of two). We then image the remaining atoms in the imaging state, usually after some time of flight.

In this experiment, we probe the $|9/2, -7/2\rangle$ spin component. The hollow light beams are resonant with the transition from the $|9/2, -7/2\rangle$ state to the electronically excited $|5/2, -5/2\rangle$ state (see figure 3.1). Atoms in this excited state decay by spontaneous emission with a branching ratio of 0.955 to the $|7/2, -7/2\rangle$ ground state and 0.044 to the original $|9/2, -7/2\rangle$ state. After releasing the trap and applying the hollow light beams, we allow the cloud to expand for 10 or 12 ms time of flight. To optimize the signal-to-noise ratio in the image, we use an rf π-pulse to transfer

4P_{3/2}
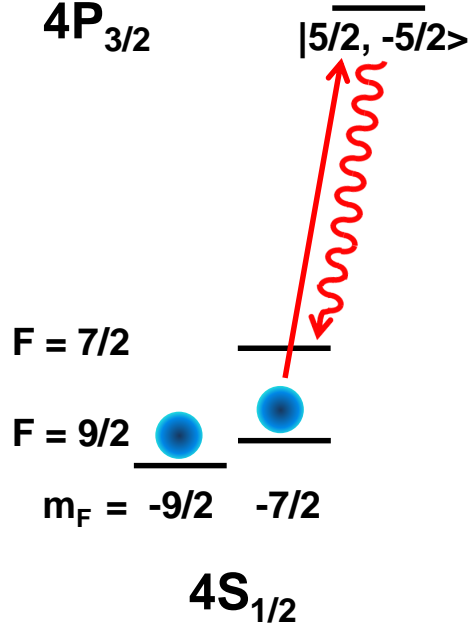
Figure 3.1: **Optical pumping transition driven by the LG mode beams.** Schematic level diagram showing the optical pumping transitions. The relevant states at $B = 208.2$ G are labeled with the hyperfine quantum numbers of the $B = 0$ states to which they adiabatically connect.

the remaining $|9/2, -7/2\rangle$ atoms to the $|9/2, -9/2\rangle$ state and then image with light resonant with the cycling transition. Just prior to this rf pulse, we clean out the $|9/2, -9/2\rangle$ state by optically pumping these atoms to the upper hyperfine ground state ($f=7/2$). The imaging light propagates along the z direction, and we apply an inverse Abel transform to the 2D image (assuming spherical symmetry in k-space) to obtain the 3D momentum distribution, $n(k)$.

3.3   Seeing the Fermi step

In figure 3.2, we show momentum distributions measured with and without using the hollow light beams. As shown in figure 1.5 and Ref. [13], the trap-averaged momentum distribution for the Fermi gas is only modestly distorted from the Gaussian distribution of a classical gas. The dashed
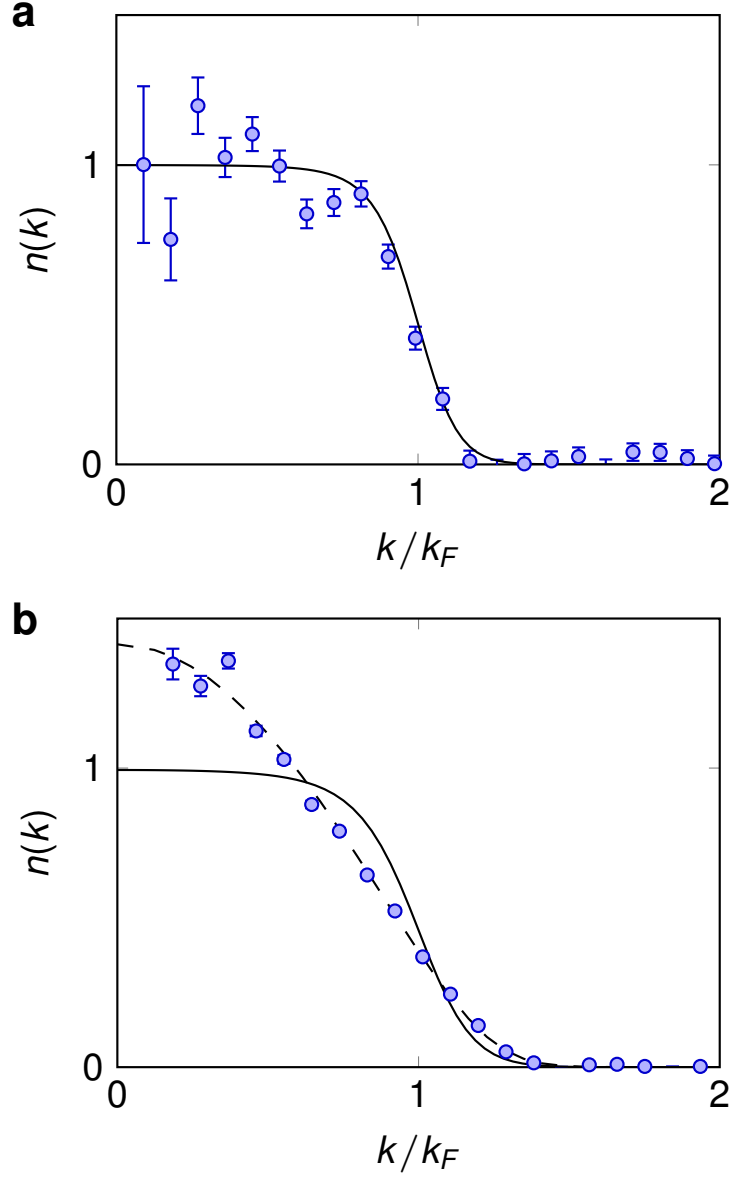
Figure 3.2: **Measured momentum distribution for a weakly interacting Fermi gas. a.** The momentum distribution of the central 16% of a harmonically trapped gas is obtained from the average of twelve images. This distribution has been normalized such that the area under the curve is equal to 1. The solid line shows a fit to a homogeneous momentum distribution, where T is fixed to the value obtained from the trap-averaged distribution and k_F is the only fit parameter. **b.** For comparison, I show the trap-averaged distribution, taken from an average of six images, with fits to the expected momentum distribution for an ideal gas in a harmonic trap (dashed line) and to the homogeneous momentum distribution (solid line).

line in figure 3.2b shows a fit to the expected momentum distribution for a harmonically trapped ideal Fermi gas, from which we determine the temperature of the gas to be $T/T_{F,\mathrm{trap}} = 0.12 \pm 0.02$.

Here, the Fermi temperature for the trapped gas is given by $T_{F,\text{trap}} = E_{F,\text{trap}}/k_B$, where $E_{F,\text{trap}} = h(\nu_r^2 \nu_z)^{1/3}(6N)^{1/3}$ is the Fermi energy for the trapped gas. After optical pumping with the hollow light beams so that we probe the central 16% of the atoms, the measured momentum distribution (part a of figure 3.2) has a clear step, as expected for a homogeneous Fermi gas described by equation 3.1.

For a sufficiently small density inhomogeneity, the momentum distribution should look like that of a homogeneous gas at some average density. To characterize this, we fit the normalized distributions to the prediction for an ideal homogeneous gas (solid lines), normalized in terms of k_F and T_F:

$$n(k/k_F) = \frac{k_F^{-3}}{\frac{1}{\zeta}e^{\frac{(k/k_F)^2}{T/T_F}} + 1}, \tag{3.2}$$

where ζ is the fugacity of a homogeneous Fermi gas, which is a function of T/T_F and given by,

$$Li_{3/2}(-\zeta) = \frac{-4}{3\sqrt{\pi}(T/T_F)^{3/2}} \tag{3.3}$$

To obtain the solid lines in figure 3.2a and b, we fix T/T_F to the value we measure for the trapped gas, which leaves only a single fit parameter, k_F, which characterizes the density. The momentum distributions are then plotted as a function of the usual dimensionless momentum, k/k_F. The momentum distribution of the central 16% of the trapped gas fits well to the homogeneous gas result, while the trap-averaged momentum distribution clearly does not.

3.3.1 Approximating our results as "homogeneous"

In order to quantify how well the measured momentum distribution is described by that of a homogeneous gas, we look at the reduced χ^2 statistic in figure 3.3a. The reduced χ^2 is much larger than 1, indicating a poor fit, for the trap-averaged data due the fact that the density inhomogeneity washes out the Fermi surface. As we probe a decreasing fraction of atoms near the center of the trap, χ^2 decreases dramatically and approaches a value of 1.6 for fractions smaller than 40%.

The single fit parameter k_F characterizes the density of the probed gas and should increase as we probe only those atoms near the center of the trap. Figure 3.3b displays the fit value k_F, in units
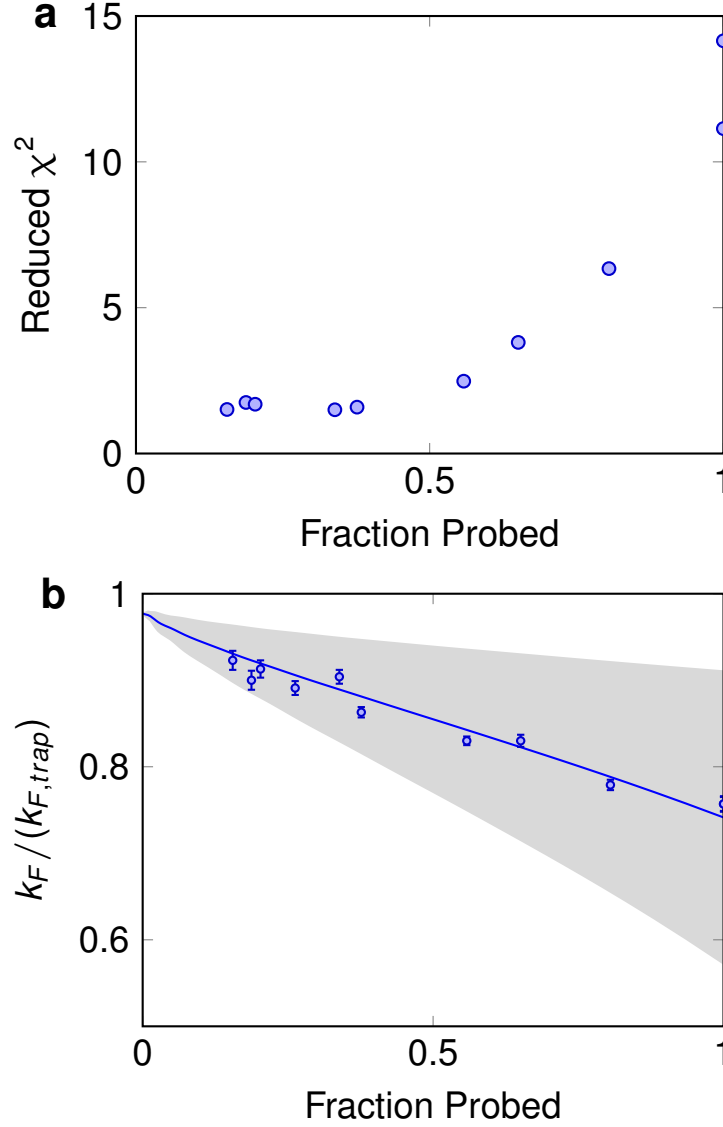
Figure 3.3: **Fit results as a function of the fraction of atoms probed.** (a) As the fraction of atoms probed is decreased, the reduced χ^2 for the fit to a homogeneous gas momentum distribution decreases dramatically and approaches a value of 1.6 for fractions less than 40%. The minimum χ^2 is limited by systematic noise in the image (i.e. fringes). (b) The best fit value of k_F increases as we increasingly probe only the atoms in the central (highest density) part of our trap. A model of the optical pumping by the hollow light beams yields an average local k_F indicated by the solid line. As an indication of the density inhomogeneity, the shaded region shows the spread (standard deviation) in k_F from the model.

of $k_{F,\text{trap}} = \sqrt{2mE_{F,\text{trap}}}/\hbar$. As expected, k_F increases as the fraction of atoms probed decreases.

We have developed a model of the spatially selective optical pumping by the hollow light beam, which I discuss in section 3.4. The model result for the average local k_F, $\langle k_F \rangle$, of the probed gas is
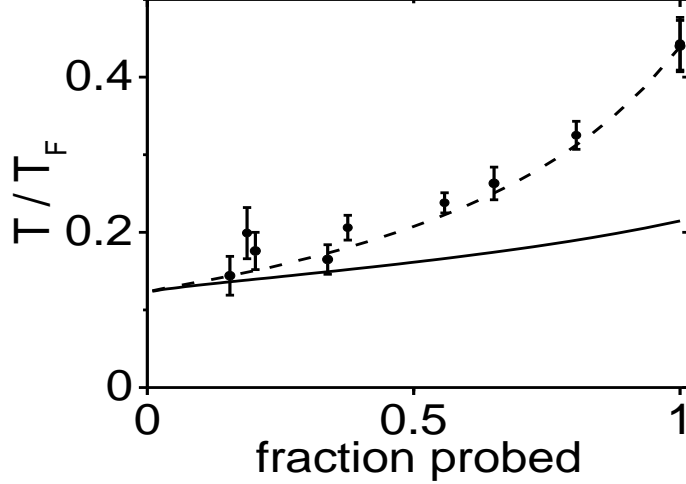
Figure 3.4: **Measured T/T_F vs the fraction of atoms probed.** We fit the measured momentum distribution to a homogeneous gas distribution with two free parameters, T/T_F and k_F. The plot shows the best fit value for T/T_F as a function of the fraction of atoms probed near the center of the cloud. The density inhomogeneity of the probed gas can result in a T/T_F that is much larger than that expected from the calculated average density of the probed gas (solid line). A sharp Fermi surface, characterized by a small fit T/T_F, emerges as the fraction of atoms probed decreases. The dashed line shows the result of fitting to model calculations of the probed momentum distribution, which agrees well with the data.

shown with the solid line in figure 3.3b, and we find that this agrees well with the fit k_F, even when the measured momentum distributions clearly do not look like that of a homogeneous gas. Using the model, we calculate the variance of the local k_F, $\delta^2 = \langle k_F^2 \rangle - \langle k_F \rangle^2$, and the shaded region in figure3.3b shows $\langle k_F \rangle \pm \delta$. In the region where the reduced χ^2 indicates that the measured $n(k)$ fits well that for a homogeneous gas (fraction probed < 40%), $\delta/\langle k_F \rangle < 0.08$.

3.3.2   How homogeneous is "homogeneous enough"?

An important question when we use our selective imaging technique is how selective we need to be for the results to be considered that of a "homogeneous" gas. This, of course, depends on the width of the features that one wishes to see. Since all of the signal originates from a gas confined in a smooth, harmonic potential, the only way to probe a perfectly homogeneous density is to probe only one atom. Instead, we hope to find a "sweet spot" for which we can reproduce sharp features but still have decent signal to noise.

Ideally, we'd like to measure features whose widths are determined by temperature or interactions and not significantly modified by any remaining spread in densities. For the ideal Fermi gas, this would mean that the width of the step in the momentum distribution will reflect the true T/T_F of the gas.

We can check this by fitting the results to a homogeneous gas distribution, with both k_F and T/T_F as fit parameters. For a gas with a completely homogeneous density, this fit returns the average temperature of the atoms. On the other hand, a large density inhomogeneity that washes out the Fermi surface because of a spread in the local values of k_F will result in an artificially high fit value for T/T_F. This can be seen in figure 3.4. The solid line shows the average $T/\langle T_F \rangle$ for the probed gas calculated using our model. Here, T is fixed and the dependence on the fraction probed comes from the fact that the average density, and therefore the average local T_F, increases as we probe a smaller fraction of atoms. The fit T/T_F approaches the average value from the model as we reduce the fraction of atoms probed, and for $\lesssim 40\%$ probed, the two are consistent within our measurement uncertainty. For the smallest fraction probed (data shown in figure 3.2), the best fit value is $T/T_F = 0.14 \pm 0.02$. As a check of the model, we can also calculate $n(k)$ for the probed gas and fit this to the homogeneous gas distribution; the results (dashed line in figure 3.4) agree well with the data.

From this data, we find that when probing 40% or less of the atoms, the observed momentum distribution is consistent with that of a homogeneous gas, where the width and position of the Fermi surface reflect the average temperature and density of the probed portion of the gas.

3.4   Modeling the signal removal

Even though the emergence of a sharp Fermi surface proves the effectiveness of our donut beam technique, a model describing the optical pumping is useful for understanding the remaining density inhomogeneity. While it might have been simpler if our donut beams had a perfectly sharp cut, eliminating all signal past a certain radius, we know that the inner walls of the LG beams have some finite width, and we can use the model to see how much this effects our final signal.

3.4.1   The model

In modeling the effect of optical pumping with the hollow light beams, we assume that only atoms that do not scatter a photon are probed. The probability to scatter zero photons from each beam at a particular location in the cloud is taken to be $P_i(\vec{r}) = \exp(-\gamma_i(\vec{r})\tau_i\sigma)$, where τ_i is the pulse duration and the subscripts $i = 1, 2$ denote the two hollow light beams. The photon flux is given by $\gamma_i(\vec{r}) = I_i(\vec{r})\lambda/(hc)$, where $I_i(\vec{r})$ is the position-dependent intensity, c is the speed of light, and $\lambda = 766.7$ nm is the wavelength. For the optical absorption cross section, we use $\sigma = 3\lambda^2\eta/(2\pi)$, where η is the branching ratio between the initial and final states. For the intensities, we use equation 2.1 with $l = 2$ and make the approximation that w is constant across the cloud.

Attenuation of the hollow light beam as it propagates through the atom cloud is observable in the long direction of the cloud (along z), and the effect of this can be seen in figure 3.5b. To include this effect, we consider the two hollow light beam pulses sequentially, and we assume that the number of photons absorbed locally equals the number of optically pumped atoms. Interestingly, the model predicts that the attenuation results in a smaller density variance in the probed gas when compared to a model that ignores attenuation but where we adjust the beam powers to probe the same fraction of the atoms. This effect is relatively small and decreases as one probes a smaller fraction of the gas. This can be seen in figure 3.5 where we show the measured momentum distribution for the central 38% of the atoms compared to three different models, each of which is adjusted to give the same probed fraction. The solid line is the model explained above, which includes attenuation, while the dotted line shows the result when we ignore the depletion of the hollow light beams. For comparison, the dashed line shows the expected distribution if one selects atoms in a cylindrical volume with sharp boundaries. All three of the models give similar results, which is good—it shows us that our technique is independent of any particular details of the optical pumping.

Although we see that our results are model independent, for the rest of this thesis, we choose to use the model that includes attenuation of both beams by the atoms, as we believe this provides
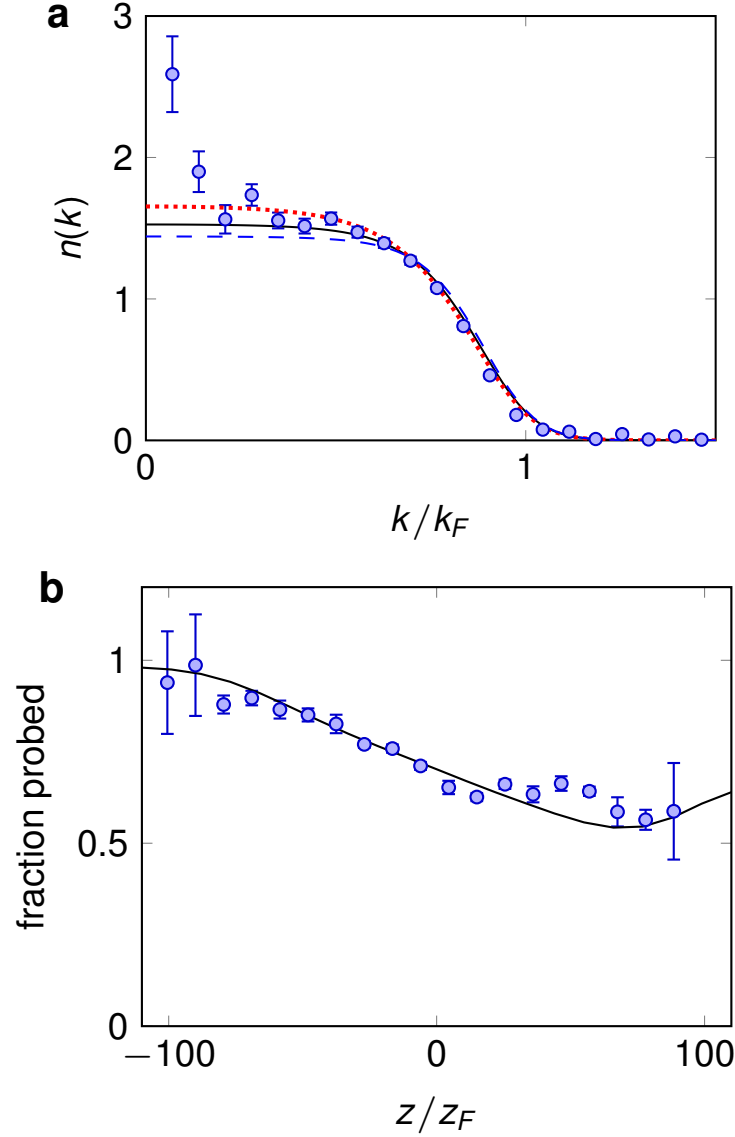
Figure 3.5: **Modeling the spatially selective optical pumping. a.** Comparison of the normalized momentum distribution of the central 38% of the atoms with three different models (dotted, solid, and dashed lines; see text). The data (circles) are obtained from an average of four images. We find that the attenuation of the hollow light beams (included in solid line model) does not strongly affect the predicted final momentum distribution when probing a small fraction of the gas. **b.** An image of the cloud is taken with a probe beam that is perpendicular to the long (z-) direction. The image is taken after only a short (1.3 ms) expansion so that we probe the spatial dependence of the density. We compared images with the horizontal hollow light beam and without any optical pumping in order to measure the fraction of atoms probed (circles) vs z/z_F, where $z_F = \sqrt{\frac{2E_{F,\text{trap}}}{m(2\pi\nu_z)^2}}$. For this data, the total fraction of atoms probed is 71%. The prediction of our model (solid line), which includes attenuation of the hollow light beam as it propagates through the cloud, agrees well with the data.
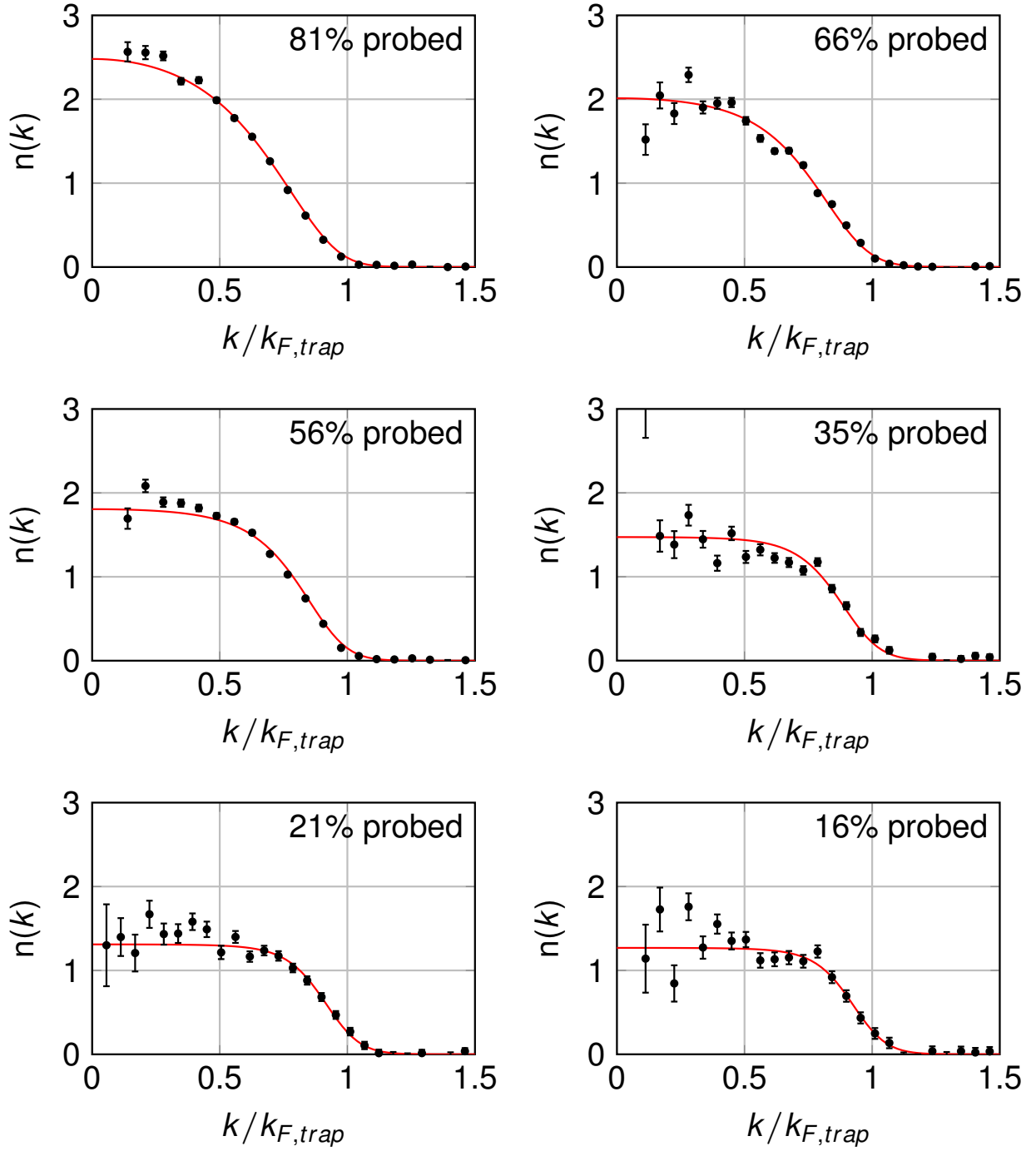
Figure 3.6: **Model of spatially selective optical pumping technique compared to data at six different donut beam powers.** The x-axis of these graphs are in units of the k_F of the trap, given by $k_{F,trap} = \frac{\sqrt{2mE_{F,trap}}}{\hbar}$, instead of being determined by fitting, as in figure 3.2.

the most correct physical description. Using the well-known phase space distribution of an ideal Fermi gas in a harmonic trap, we can make predictions for the momentum distributions of the Fermi gas given a certain amount of signal probed. Figure 3.6 shows data from six removals compared to the results from the model. The agreement is very good.

3.4.2 Collisions in time of flight

While we find our model of the donut beam technique reproduces our data very well, it does not take into account any collisions that may occur after the donut beam optical pumping. In the model, atoms that have been removed from the signal have no effect on the atoms that remain in the imaging state. This is how we hoped our technique worked, but it was important to verify whether this was indeed the case.

One of the main reasons for developing the donut beam technique was to be able to take measurements of a homogeneous sample after a time of flight expansion such that we get momentum information from a uniform density. As such, we tried to be extra careful to characterize the ways that the donut beam technique might interfere with accurately measuring the momentum of the gas. One such way would be if the atoms in the imaging state underwent collisions with atoms optically pumped to the dark state during time of flight expansion. This process could potentially destroy the momentum information we are trying to extract.

When imaging the momentum distribution of a non-interacting cloud, we use a magnetic Fano-Feshbach resonance to set the s-wave scattering length that parametrizes interactions between our two main spin states, $|9/2, -9/2\rangle$ and $|9/2, -7/2\rangle$, to -30 a_0. The number of collisions during expansion is negligible. (The collision rate is roughly three collisions a second for typical densities in the optical trap, while the expansion time is no more than 12 ms.) However, the optically pumped atoms in the F $= 7/2$ manifold could potentially interact with our $|9/2, -7/2\rangle$ atoms and scramble their momenta. To investigate this effect, we performed a Monte Carlo (MC) simulation of collisions on an atom cloud during a 10 ms expansion.

There are potentially two types of collisions that can change our signal, inelastic (or spin

changing) and elastic. The elastic scattering rate can be determined by the s-wave scattering length and the atomic velocity; for $a = 200a_0$ and $v_F = 0.0128$ m/s (where a_0 is the Bohr radius and $v_F = \frac{\hbar k_F}{m}$ is the Fermi velocity), the elastic scattering rate can be estimated to be $\Gamma_{el} = K_{elastic} * n$, where $K_{elastic} = (4\pi a)^2 * v_F = 1.8 \times 10^{-11} \text{cm}^3/\text{s}$. The inelastic scattering rate constant, calculated by John Bohn (personal communication, March 2012), is smaller but comparable—$K_{inelastic} = 8.5 \times 10^{-12}$ cm^3/s for $|9/2, -7/2\rangle$ colliding with $|7/2, -5/2\rangle$. (The optically pumped atoms can fall into other hyperfine states, but we expect all of the scattering rates to be similar.)

In the simulation, we calculate the effects of both elastic and inelastic collisions in a cloud with typical initial conditions and donut removal. First, we create an ensemble of roughly 100,000 atoms at T $= 0.12T_F$. Using a Monte Carlo technique, we assign three position and three momentum coordinates to each atom (x, y, z, k_x, k_y, k_z). Then, using our model of donut removal, we put 77% of the atoms at the cloud edges into the higher energy $F = 7/2$ hyperfine manifold. 23% of the atoms remain in the $|9/2, -7/2\rangle$ imaging state.

Once the distributions of positions, momenta, and spin states are set, we look for atoms in the imaging state that are close enough to an $F = 7/2$ atom to undergo a collision. If the atoms are close enough (we check all particles that are closer than 40% of the cloud's Thomas-Fermi radius), we calculate their probability to collide (either elastically or inelastically) based on their relative positions and velocities. Still using Monte Carlo, we decide whether the atoms collide based on that probability. If the collision is elastic, we recalculate the momenta of the two atoms and allow them to remain in the simulation; if the collision is inelastic, they are removed from the signal. After calculating the collisions, we let the atoms move in free space (no confining potential) for a small amount of time compared to the collision rate. After that motion, we use the new momenta and positions of the atoms to move them for another time step and recalculate the probability to collide. This process continues for 10 ms of time of flight expansion.

In the simulation, we find that 7% of those atoms left in the imaging state will undergo an elastic collision during expansion and roughly 2% will undergo spin-changing collisions (and be lost from the signal). Figure 3.7 shows a single simulated momentum distribution of our cloud extracted
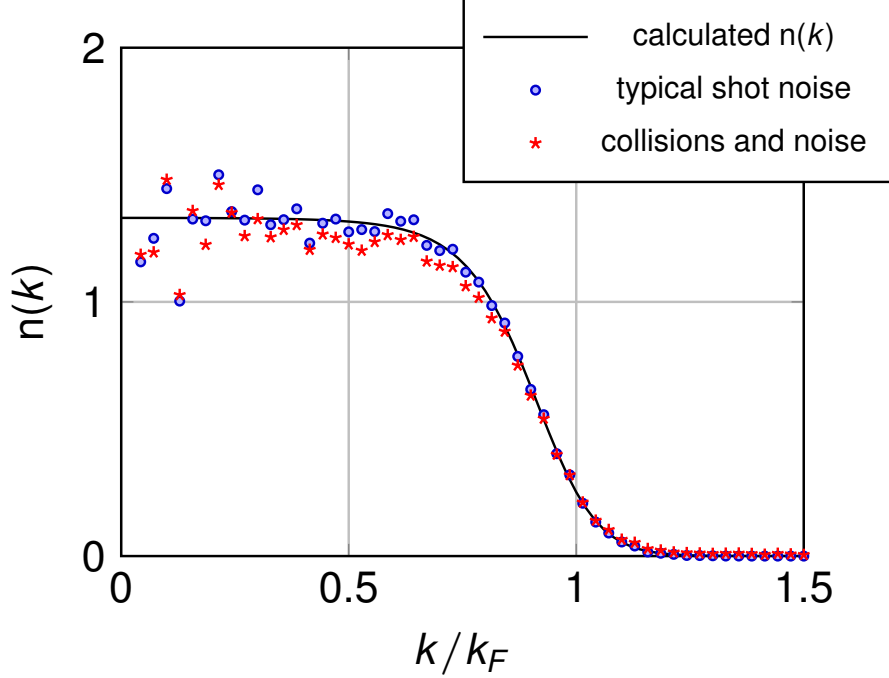
Figure 3.7: **Momentum distribution with and without collisions.** Using the model of optical pumping and the phase space distribution of an ideal Fermi gas, we calculate what the momentum distribution would like if only 23% of the signal is probed (39% removed by the vertical beam). The black line shows this calculation, while the blue points show this calculation plus a typical amount of noise. The red points show how the (blue) momentum distribution changes after a 10 ms expansion, during which the atoms may collide with the optically pumped atoms. We conclude from this that the effect of collisions on our signal is negligible.

from the spatial distribution of atoms after 10 ms time of flight expansion. We find that the collisions during expansion have the effect of slightly scrambling our signal and slightly increasing the weight about $k = k_F$, but we also see that the effect is small. We fit the final momentum distributions to the Fermi distribution for a homogeneous gas, allowing k_F and T/T_F as fit parameters. We find that the fitted T/T_F (from fitting to a homogeneous momentum distribution) increases from 0.141 to 0.155 (which is generally within our uncertainty) with no appreciable change to k_F. From this we conclude that the effect of collisions during expansion is below what we can observe.

3.4.3   Effect of finite branching ratio: the return of hot atoms

While our model of spatially selective imaging relies on the assumption that we are only measuring atoms that have not scattered a photon, this is not necessarily the case. The optical pumping transitions that we use have a small but finite branching ratio, which gives the probability for an atom to spontaneously decay back to initial state after scattering a photon. If this occurs, the atom will remain to be imaged (barring the possibility of scattering another photon), and will retain two extra momentum 'kicks' from first absorbing and then re-emitting a photon. This extra momentum would be on the order of the Fermi momentum, so this process could potentially have a significant effect on the measurement of the Fermi step.

In chapter 2, I presented two optical pumping transitions that we utilize in the donut beam technique. The transition used in this chapter (and the next) is $|F, m_F\rangle = |9/2, -7/2\rangle \rightarrow |F', m_{F'}\rangle = |5/2, -5/2\rangle$. This has a 0.044 branching ratio, so 4.4% of the atoms that absorb a photon will return to the $|9/2, -7/2\rangle$ imaging state. The transition used with photoemission spectroscopy (chapters 5 and 6) is $|F, m_F\rangle = |9/2, -5/2\rangle \rightarrow |F', m_{F'}\rangle = |5/2, -3/2\rangle$, which has a 0.096 branching ratio and thus an enhanced effect. We spent a good deal of time worrying about and looking for this background of hot atoms, particularly for the higher branching ratio transition. It was important for us to understand how much these unwanted hot atoms could distort the momentum information of our gas.

Generally, when using the technique of "optical pumping", one does not need to worry about atoms falling back into the initial state, even for transitions with a particularly high branching ratio. This is because *eventually* all atoms will fall into another state, called the "dark state." If they are not pumped there at first, increasing the power or duration of the optical pumping should continue to drive the transition until no atoms are left in the initial state. Our problem is that our optical pumping beams have a shape, with inner walls that are not infinitely sharp. Even as the power is increased, there will be a small part of the beam with low enough intensity that it will only ever drive one transition at most. On the other hand, some of the atoms (those closer

to the cloud edges and sitting in the middle of the donut "ring") experience a much higher optical pumping intensity, and will almost certainly be pumped again if they happen to fall back to the initial state.

3.4.3.1 Estimating the size of the effect

If atoms are returning to our imaging state after being pumped, the signal we image will be composed of atoms that were not pumped ("good signal") and a small amount of atoms which return from the excited state to their initial state with extra momentum ("bad signal"). We can make a simple calculation to estimate how large the effect of atoms falling back into the imaging state would be. A simple picture of this process is as follows. There is some probability, P, for an atom to be optically pumped, which depends on the intensity of the donut beam. There is also some probability, η, for an optically pumped atom to decay back to the imaging state, which is equal to the branching ratio between the initial and excited states. For the purposes of this calculation, let's assume that the intensity of the optical pumping light is uniform across the cloud and unchanging in time. Thus, P is also uniform and unchanging. We know that this is not true; the optical pumping beam has an LG spatial mode and loses photons as it scatters off the atoms. However, this simple calculation should give us a rough estimate of the amount of the "bad signal" we might expect.

This picture can be described by the following equation:

$$N_{imaged} = N_{initial} - \sum_{i}^{N_{events}} \left(P^i * N_{initial} - \eta^i * P^i * N_{initial} \right), \tag{3.4}$$

where $N_{initial}$ is the number of atoms before optical pumping, N_{events} is the number of times an atom is allowed to scatter a photon, and N_{imaged} is the total number of atoms in the imaging state after optical pumping. The terms in the sum correspond to the effects of optical pumping by at most i photons; for $i = 1$, we calculate that $P * N_{initial}$ atoms scatter one photon, removing them from the signal, and then $\eta * P * N_{initial}$ of those atoms return with extra momentum. In this case, the "good signal" (i.e. atoms with their original momenta) is equal to $(1 - P) * N_{initial}$, while the

(a) chance to return is 4.4 %

Scattering events allowed:
—— one ·········· two – – – three

(b) chance to return is 9.6 %
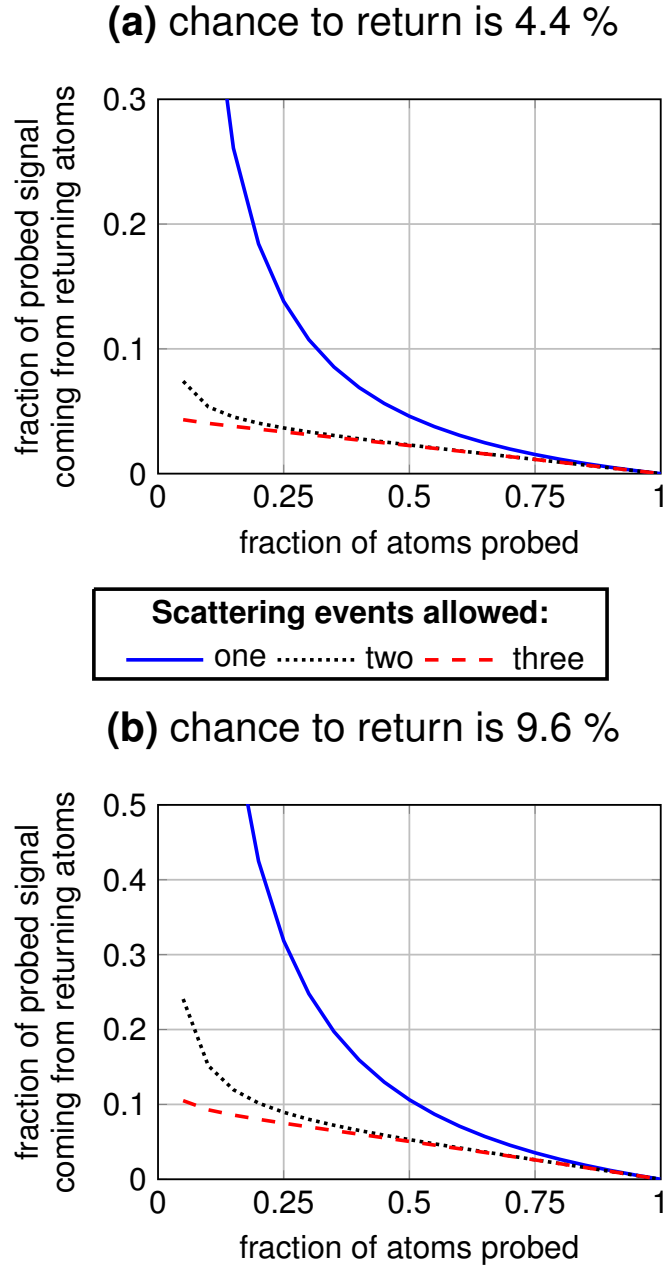
Figure 3.8: **The size of the "bad signal" for two branching ratios.** Using equation 3.4, I can estimate the fraction of the signal that comes from atoms with an extra momentum kick from having scattered a photon. The blue line is the estimated fraction of bad signal if the atoms can scatter at most one photon. As we account for more scattering events, the atoms which have fallen back into the imaging state after being pumped have another chance to be removed, and the fraction of bad signal begins to converge to a lower value. The two graphs correspond to the two optical pumping transitions we use, found in figure 2.4. From these calculations, we estimate the error from "hot atoms" to be below 5% for transition **a** and below 10% for transition **b**.

"bad signal" which comes from returning atoms is given by $\eta * P * N_{initial}$. There is some chance that these "bad atoms" will scatter more photons, which gives them more chances to leave the imaging state. The terms for which $i > 1$ describe this process.

Figure 3.8 shows what fraction of the imaged signal will be composed of atoms with extra momentum kicks, given by equation 3.4. This quantity is found by solving for a particular fraction of atoms imaged after pumping, $N_{imaged}/N_{initial}$, and taking the difference between that and the fraction of atoms pumped by one photon, $(1-P)$ (the "good signal"). The three lines correspond to calculations including the first one, two, or three terms in equation 3.4. Figure 3.8**a** was performed for a branching ratio of $\eta = 0.044$, which corresponds to the optical pumping transition used in this chapter and in chapter 4. Figure 3.8**b** includes a branching ratio of $\eta = 0.096$, which corresponds to the transition used in this chapters 5 and 6.

The fraction of "bad atoms" contributing to the signal increases as more atoms are optically pumped, which is expected. However, allowing for more than one photon scattering event for situations when the optical pumping intensities are high (low fraction of atoms probed) causes the calculation to converge to a smaller "bad signal." This result makes sense—in the case of high optical pumping intensity, the atoms would be more likely to scatter multiple photons, and any returning atoms would have another chance to leave the signal. For most of the data taken in this thesis, the fraction of atoms imaged after the donut beam technique is 25–30%. Thus, we can expect a 3% effect on the signal for transition **a** and a 7% or less effect for transition **b**. Both of these are quite small effects, which, as with the effects of collisions with our dark atoms, we expect will be beneath the noise in our system.

3.5   Conclusions

Our first experiments with the donut beam technique gave us confidence that we could recover sharp features, such as the Fermi step, that would otherwise be washed out of our data. We were initially concerned that this approach might leave too little signal when selecting a small enough region to approximate a homogeneous gas. However, for a gas at $T/T_{F,\text{trap}} = 0.12$ and

our typical measurement precision, we find that probing the central 40% (or less) of the gas is sufficient to approximate a homogeneous gas. We take advantage of the "sweet" spot in the following experiments; in general we probe $25-30\%$ of the gas and see that we are sufficiently homogeneous.

Direct observation of the Fermi surface was pretty satisfying as far as experiments go; it is not every day that your results look like they came from a statistical mechanics textbook! Additionally, the momentum distribution of an ideal Fermi gas has a well-known form, and comparing our results to our expectations allowed us to test our understanding of what the donut beam technique does. Armed with this, we stepped away from the known and into the unknown—in this case, the regime of strong interactions, where the properties of the Fermi gas are still a subject of research. The rest of this thesis presents experiments on gases in the BCS-BEC crossover, where we use spatially selective imaging to probe the local properties of our gases.

Chapter 4

Contact of a homogeneous gas

This chapter presents our measurement of the local, or homogeneous, contact of a unitary Fermi gas as a function of temperature. The contact is a measure of short-range correlations between atoms with a short-range interaction. First defined by Tan in 2005 [2], the contact is a universal quantity that is valid for a very wide range of circumstances—including zero and finite temperature gases, superfluid and normal phases, few and many particle systems, and balanced or imbalanced spin populations. Recent work has shown that the contact can be extended to bosons [44, 45], three-body interactions [46], and nucleons in atoms [47].

Theoretical predictions for the temperature dependence of the contact of a Fermi gas differ substantially, especially near the superfluid transition temperature, T_C/T_F. However, since the Fermi temperature, T_F, is density dependent, even large features near the phase transition can be lost when the measurement is taken from atoms in a harmonic trap. Using our spatially selective imaging, we measure the contact for atoms at the center of our trap where the density is nearly homogeneous. In this data, we observe a sharp feature not distinguishable in previous contact measurements [48]. This feature may be associated with the superfluid transition. The work in this chapter has been published in Ref. [49].

4.1   What is the contact?

In 2005, Shina Tan derived a number of universal relations for an interacting Fermi gas with short-range, or contact, interactions [2, 50, 51]. These powerful relations connect microscopic

quantities, such as the momentum distribution of the fermions, to macroscopic quantities, such as the total energy of the system. Furthermore, the relations are universal in that they do not depend on the details of the interparticle potential, nor do they depend on the state of the system, which could be an exotic Fermi superfluid, a normal Fermi liquid, or even a simple two-body state such as a diatomic molecule. At the heart of the universal relations is a single quantity, which Tan termed the contact.

4.1.1   Tan's definition: the high momentum tail and the Tan relations

The contact was first introduced as a quantity in Ref. [2]. It was defined as the coefficient of the high momentum tail of the momentum distribution, $n(k)$:

$$\mathbf{C} \equiv \lim_{k \to \infty} k^4 n(k). \tag{4.1}$$

The contact is an integration of the contact density, $\boldsymbol{\mathcal{C}}(\boldsymbol{R})$; $\mathbf{C} = \int d^3\boldsymbol{R}\, \boldsymbol{\mathcal{C}}(\boldsymbol{R})$. $\mathbf{C}$ has units of inverse length and is often normalized by k_F.

Equation 4.1 is the first of the so-called "Tan relations". It is has been known for some time that the momentum distribution of particles interacting via a contact interaction has a tail that scales as k^{-4} [52]. However, the real advance came in the universal relations that Tan presented [2, 50, 51], which connected the contact to other extensive properties of the gas, such as energy and pressure. The other relations connect the contact to the spatial correlation atoms in the two spin states, n_1 and n_2, for short distances [51],

$$\langle n_1(\boldsymbol{R} + \frac{r}{2}) n_2(\boldsymbol{R} - \frac{r}{2}) \rangle \xrightarrow[r \to 0]{} \frac{1}{16\pi^2} \left(\frac{1}{r^2} - \frac{2}{ar} \right) \boldsymbol{\mathcal{C}}(\boldsymbol{R}); \tag{4.2}$$

the sum of the kinetic and interaction energies (T and I, respectively) [51],

$$T + I = \sum_{\sigma} \int \frac{d^3k}{(2\pi)^3} \frac{\hbar^2 k^2}{2m} \left(n_\sigma(k) - \frac{\mathbf{C}}{k^4} \right) + \frac{\hbar^2}{4\pi ma} \mathbf{C}; \tag{4.3}$$

the virial theorem [50],

$$T + I - V = -\frac{\hbar^2}{8\pi ma} \mathbf{C}, \tag{4.4}$$

where V is the potential energy of the gas; the pressure, $\mathcal{P}$, of the gas [50],

$$\mathcal{P} = \frac{2}{3}\mathcal{E} + \frac{\hbar^2}{12\pi ma}\mathbf{C}, \tag{4.5}$$

where $\mathcal{E}$ is the energy density; the change in total energy, E, for an adiabatic (constant entropy, S) change in scattering length [2],

$$\left(\frac{\mathrm{dE}}{\mathrm{d}(a^{-1})}\right)_S = -\frac{\hbar^2}{4\pi m}\mathbf{C}; \tag{4.6}$$

and the change in total energy for an instantaneous jump in scattering length from $a_{initial}$ to a_{final} [2],

$$\Delta\mathrm{E} = -\frac{\hbar^2}{4\pi m}\left(\frac{1}{a_{final}} - \frac{1}{a_{initial}}\right)\mathbf{C}. \tag{4.7}$$

Incorporating Tan's definitions into their own work, others have shown that the contact can also be related to the total integral of the rf line shape [53, 54, 55],

$$\int_{-\infty}^{\infty} \mathrm{d}\omega\Gamma(\omega) = \frac{\hbar\Omega^2}{4m}\left(\frac{1}{a_{12}} - \frac{1}{a_{13}}\right)\mathbf{C_{12}}, \tag{4.8}$$

and its high frequency tail [56],

$$\Gamma(\omega) \xrightarrow[\omega\to\infty]{} \frac{\Omega^2(a_{12}^{-1} - a_{13}^{-1})^2}{4\pi\omega(m\omega/\hbar)^{1/2}(a_{13}^{-1} + m\omega/\hbar)}\mathbf{C_{12}}, \tag{4.9}$$

where ω is the frequency of the rf pulse, Ω is the Rabi frequency. In taking such a line shape, atoms are outcoupled from state 2, where their interactions with atoms in state 1 is given by a_{12}, to state 3, where the interaction is given by a_{13}. These relations depend on the contact of the atoms in the initial two states, $\mathbf{C_{12}}$. Other work has related the contact to the number of closed channel molecules measured by photoassociation [57, 58],

$$N_{mol} = \frac{R_*\Delta^2}{4\pi[\Delta - (B - B_0)]^2}\mathbf{C}, \tag{4.10}$$

where B_0 and Δ are the center and the width of the magnetic Fano-Feshbach resonance, and R_* is a length equal to half the effective range at the center of the resonance [55]; and the static structure factor, $S(q)$, measured using Bragg spectroscopy [59],

$$S_{12}(q) \xrightarrow[\omega\to\infty]{} \frac{1}{8}\left(\frac{1}{q} - \frac{4}{\pi aq^2}\right)\mathbf{C}, \tag{4.11}$$

where q is the momentum selected by the Bragg pulses. (For all of the above equations, m is the atomic mass, a is the s-wave scattering length between the two Fano-Feshbach resonance states, and $\hbar/2\pi$ is Planck's constant.)

The contact and its relations are valid for all scattering lengths and phases of the system and encapsulate all of the many-body physics of the gas [57]. Many of these relations have been verified in experiment, both by our group and by others [60, 3, 45, 48, 61, 62].

4.1.2 An "intuitive interpretation"

In Ref. [55], Eric Braaten presented a physical picture of the contact, using equation 4.2 listed above. It is the explanation I find most intuitive, and I have paraphrased it below.

Suppose you have a gas with two types of fermionic atoms, atom A and atom B. A and B interact with each other via a low energy (s-wave) scattering length, a, that is much larger than the effective range of the interactions. (This type of interaction is called a contact interaction, and it can be modeled using potential wells with depths of finite size [63].) Being fermions, A doesn't interact with A nor B with B.

Now, let's calculate the probability to find a B atom near a particular A atom. To be concrete, we are looking in a volume, $V = \frac{4}{3}\pi l^3$, surrounding the A atom. This probability will be determine by the average number density of B atoms, n_B. Indeed, for $a = 0$, this is the only factor. Additionally, as the magnitude of a increases, n_B may adjust, but for l as large or larger than the average distance between particles, n_B still completely determines the probability of finding a B atom near the A atom. However, for l much smaller than the average inter-atomic spacing, the chance to find a B atom close to an A is higher than naïvely expected from n_B. The increased magnitude of the contact interactions make the atoms "sticky" and more likely to be found close together.

Now, let's find the probability to find *any* two atoms, one of type A and one of type B, near each other. Inside large volumes, the number of such pairs is roughly $n_A * n_B * (\frac{4}{3}\pi)^2 * l^6$. However, for $l << n^{1/3}$, (where $n = n_A + n_B$) the number of pairs can be shown to scale as l^4, which is an

increase from the naïve expectation of l^6 scaling:

$$N_{pair}(l) \rightarrow \frac{l^4}{4}\mathbf{C} \tag{4.12}$$

So, the contact is directly proportional to this increased probability of short-range pairs. From Fourier transforms (or simple dimensional analysis), it is straightforward to see how the increased probability to find atoms at short distances leads to increased weight in the high momentum tail of the momentum distribution.

4.2   The contact of a homogeneous gas

The contact can be measured as a sum over the entirety of the system, or it can be presented as a local quantity, $\mathcal{C}(\mathbf{R})$, the contact density. The first measurements of the contact were the former type, where the contact had been integrated over a distribution of densities in the trapped gas (for example, see Ref. [3]). It would be years before the contact for a single density was measured.

Figures 4.1 and 4.2 illustrates the need for a measurement of the local contact. Both figures show three theoretical predictions of the contact of a gas at unitarity as a function of T/T_F. These three theories predict very different behavior, particularly around the phase transition. However, one can use the measured density distribution of atoms at unitarity in a harmonic trap to calculate what each theory predicts would be measured in such a system. In this case, the three theories become indistinguishable, and they are each shown to agree well with the results of the measurement of the contact from Ref. [61]. (Note that, for Refs. [66, 61] and figures 4.1 and 4.2, $\mathcal{I}$ is the total contact, which we call $\mathbf{C}$ and which they define in terms of the contact density, $\mathcal{I} \equiv V * \mathcal{C}(\mathbf{R})$.)

Clearly, a measurement of the contact from a single density would be helpful for distinguishing among theories and guiding future theoretical progress.
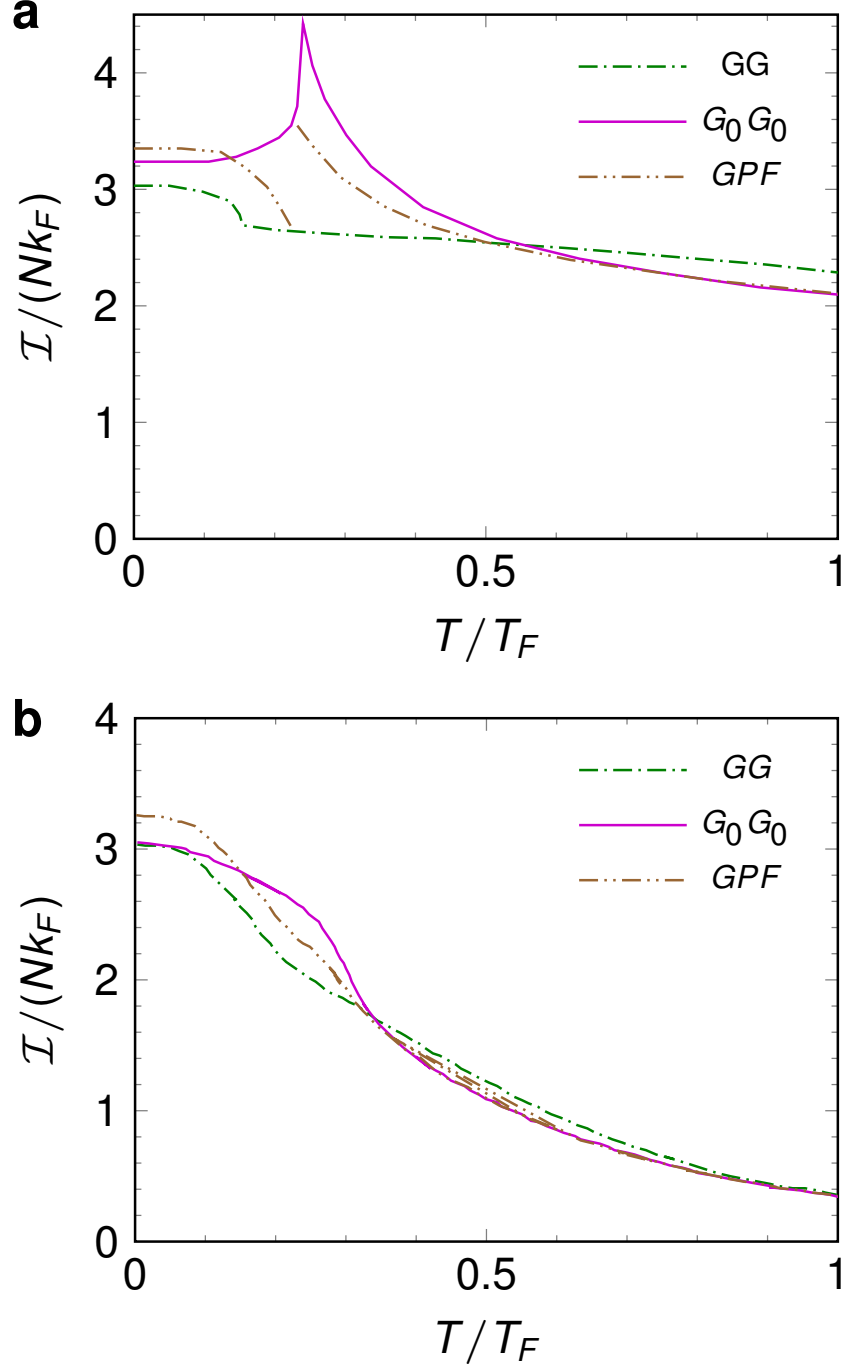
Figure 4.1: **Theories for the contact as a function of temperature.** As a comparison, we plot a self-consistent t-matrix model (GG) [64], a non-self-consistent t-matrix model (G_0G_0) [65], and a Gaussian pair-fluctuation NSR model (GPF) [66]. **a.** The theories presented for a single density. **b.** The theories after being averaged over the densities in a harmonic trap. Despite being qualitatively and quantitatively very different, after trap-averaging the three theories look similar.
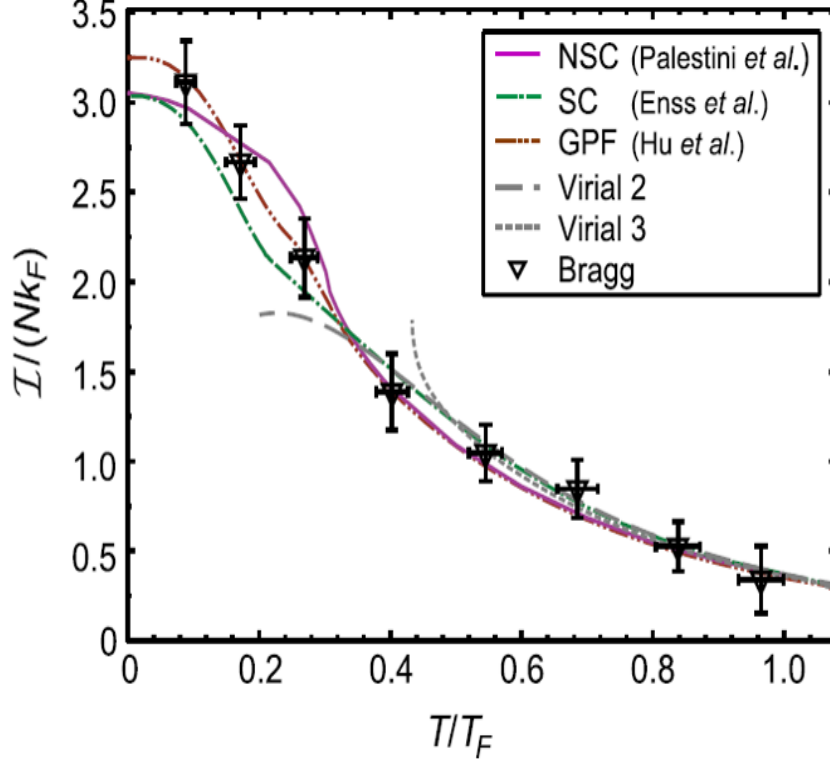
Figure 4.2: **First measurement of the contact as a function of temperature.** The measurement of the trap-averaged contact agrees very well with the theories presented in figure 4.1, as well as the virial expansion. This figure has been reproduced from *Kuhnle, et al*, Ref. [61].

4.2.1 Experiment

With this in mind, we combine our spatially selective imaging with rf spectroscopy to determine the local contact at the center of our trap. In previous work, we measured the (trap-averaged) contact in three different ways: by looking at the tail of the momentum distribution, through atom photoemission spectroscopy, and by looking at the tail of the rf line shape [3]. We chose to look at the tail of the rf line shape for this data, although in chapters 5 and 6 of this thesis, we extract the local contact from both the line shape and atom photoemission spectroscopy.

We begin with an equal mixture of ^{40}K atoms in our two Fano-Feshbach resonance states, $|f, m_f\rangle = |9/2, -9/2\rangle$ and $|9/2, -7/2\rangle$. The temperature of the gas is varied by changing the final depth of the optical dipole trap in the evaporation process. The number of atoms per spin state after the evaporation ranges from $50,000$ to $220,000$. In these measurements, the radial trapping

frequency, ω_r, ranges from $2\pi \times 200$ Hz to $2\pi \times 410$ Hz, while the axial trapping frequency, ω_z, ranges from $2\pi \times 19$ Hz to $2\pi \times 25$ Hz.

Figure 4.3: **Schematic of the experimental sequence.** The magnetic field is ramped from 203.4 G, where the atoms are initially prepared, to the Fano-Feshbach resonance. The hollow light beams are turned on $280\,\mu s$ b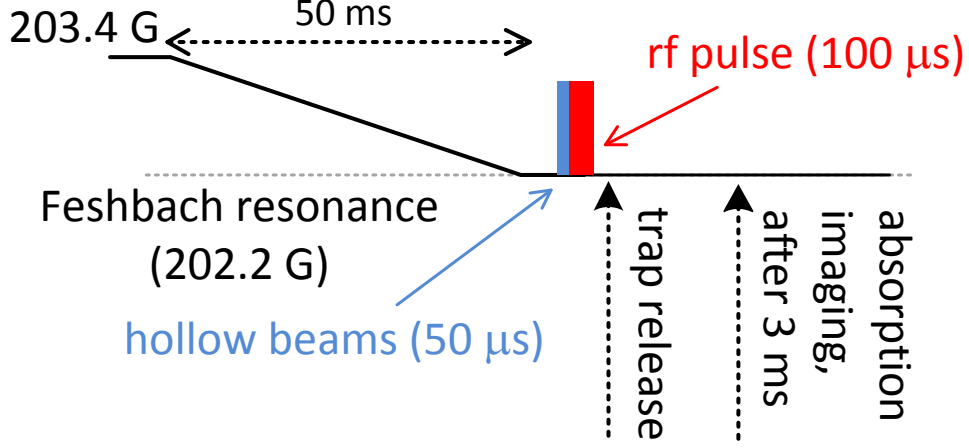efore trap release; the beam that propagates perpendicular to the long axis of the cloud is pulsed on for $10\,\mu s$ followed by $40\,\mu s$ of the second beam. The line shape is measured using an rf pulse with a total duration of $100\,\mu s$ and a Gaussian field envelope with $\sigma = 17\,\mu s$, centered $180\,\mu s$ before trap release. The cloud expands for 3 ms before being probed by absorption imaging.

The experimental sequence is depicted in figure 4.3. The magnetic field is ramped adiabatically to the Fano-Feshbach resonance and kept at this value for 2 ms before the trapping potential is abruptly shut off. Prior to turning off the potential, the hollow beams are sequentially pulsed on for $50\,\mu s$. This is followed by an rf pulse, which transfers a small fraction of the atoms in the occupied $|9/2, -7/2\rangle$ state to the initially unoccupied $|9/2, -5/2\rangle$ state. The $|9/2, -5/2\rangle$ state has a background interaction of only $180a_0$ with the other two states in the left in the trap, which allows us to approximate atoms in this state as non-interacting. The total duration of this pulse is $100\,\mu s$. We then turn off the trapping potential and let the cloud expand for 3 ms. We detect the number of transferred atoms using absorption imaging.

Absorption imaging of a low number of atoms can be difficult. To guarantee our best signal to noise, we remove all atoms not in the $|9/2, -5/2\rangle$ state using optical pumping light and use two $\pi/2$ pulses to move the $|9/2, -5/2\rangle$ atoms to the $|9/2, -9/2\rangle$ just before imaging. This state can be

imaged using the $|9/2, -9/2\rangle$ to electronically excited $|11/2, -11/2\rangle$ closed ("cycling") transition. This imaging procedure is standard in our lab, and it is particularly important for experiments incorporating our donut beam technique, as this technique leaves us with only around 30% of the signal we would otherwise have.

4.2.2   Extracting the contact
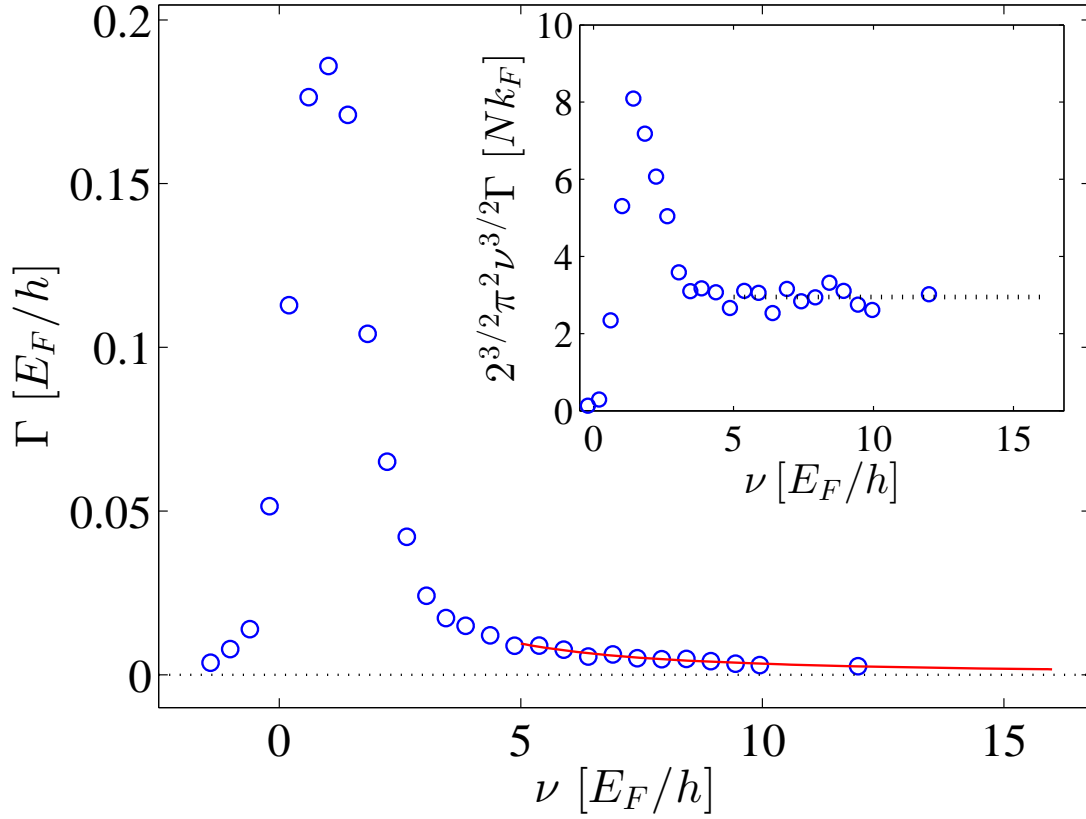
Figure 4.4: An rf line shape for the unitary Fermi gas at $T/T_F = 0.25$ with 30% of the atoms probed. The solid (red) line is a fit to equation 4.13 with the normalization $\int_{-\infty}^{\infty} \Gamma(\nu) \mathrm{d}\nu = 1/2$, due to the 50% − 50% spin mixture. The inset shows the same data multiplied by $2^{3/2}\pi^2\nu^{3/2}$. We make sure the rf pulse induces only a small perturbation, by setting its power to well below the value where we see the onset of saturation of the number of outcoupled atoms. The measurement at different frequencies is done with different rf powers, and when analyzing the data, we linearly scale the measured number of atoms outcoupled at each frequency to correspond to a common rf power.

The contact is extracted from a measurement of the rf line shape $\Gamma(\nu)$ [3], where $\Gamma(\nu)$ is the rate of atoms transferred from $|9/2, -7/2\rangle$ state to the $|9/2, -5/2\rangle$ state by an rf pulse centered at a frequency detuning ν. Equation 4.9 of the Tan relations predicts that the high frequency tail of the rf line shape scales as $\nu^{-3/2}$, with the contact determining the amplitude. This equation can be rewritten:

$$\frac{\Gamma(\nu)}{\int_{-\infty}^{\infty} \Gamma(\nu')\mathrm{d}\nu'} = \frac{\mathbf{C}/(Nk_F)}{\sqrt{2}\pi^2\nu^{3/2}} \quad \text{for } \nu \to \infty \tag{4.13}$$

where N is the total number of atoms, and $\hbar k_F$ is the Fermi momentum, and ν is the rf detuning in units of the Fermi energy, E_F/h, with h being the Planck constant ($2\pi\hbar \equiv h$).

A representative data set, where the hollow light beams were used to select the central 30% of the atom cloud, is shown in figure 4.4. For each line shape, we take data at 30 different detunings between -16 kHz and $+116$ kHz, where $\nu = 0$ is defined as the single-particle transition frequency between the $|9/2, -7/2\rangle$ and $|9/2, -5/2\rangle$ states (measured for a spin polarized gas in the $|9/2, -7/2\rangle$ state). The highest frequency typically corresponds to approximately $13\, E_F/h$. The inset of figure 4.4 shows $\Gamma(\nu)$ multiplied by $2^{3/2}\pi^2\nu^{3/2}$, where we observe a plateau for frequencies higher than $5\, E_F/h$. We extract the contact by fitting the measured $\Gamma(\nu)$ for $\nu > 5\, E_F/h$ to equation 4.13 (solid line in figure 4.4). For the normalization, we integrate the line shape, including the extrapolated tail, up to $\nu = h/mr_{\mathrm{eff}}^2$, where r_{eff} is the effective range of the interaction [67]. We find this cutoff to be $\nu = 320E_F/h$ at the Fano-Feshbach resonance.

4.2.2.1 Setting the rf power for the line shape measurements

When taking the rf line shape, it is important outcouple only a small fraction of the atoms with the rf pulse so that the data can be compared with the theoretical predictions made for the linear response regime. On the other hand, our measurements depend on having good signal to noise in the tail of the rf line shape, which requires increasing the power of the rf pulse to outcouple more atoms for larger detunings. In order to be able to compare the number of atoms taken using different powers, we have measured the number of atoms transferred by the rf pulse as a function of the rf power for different frequencies. For this measurement, the data was taken without the
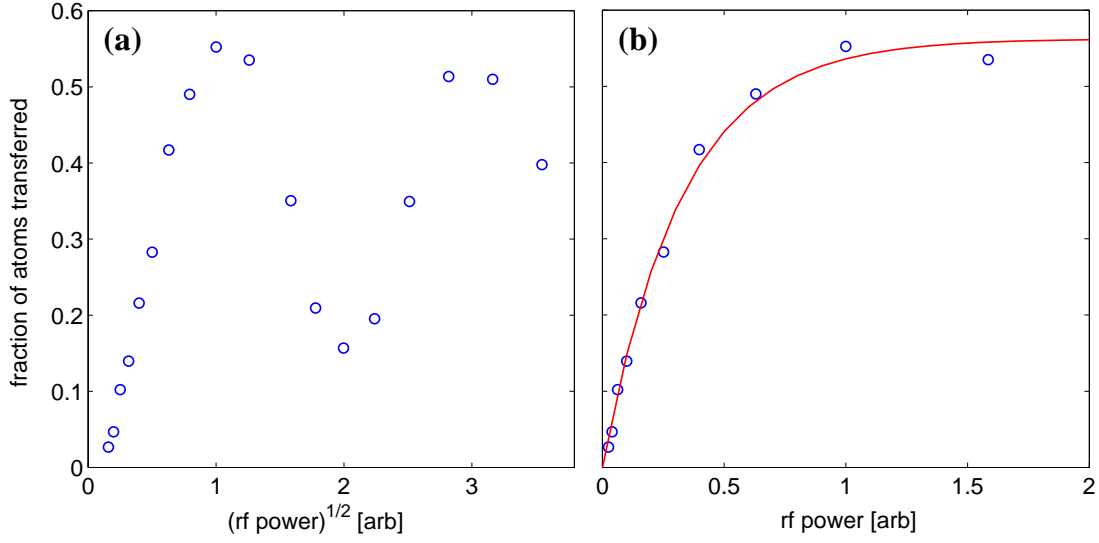
Figure 4.5: **a.** Coherent oscillations with increasing rf power at a detuning of 5 MHz relative to the single-particle transition frequency. To show the coherent oscillations, the x-axis is the square root of the rf power (which is proportional to the Rabi frequency). **b.** Zooming in on the initial rise in figure 4.5a, this time plotted as function of the rf power. The rf power is shown in experimental units and varied by changing the output of a function generator. The solid line is a fit to the exponential model introduced in the text.
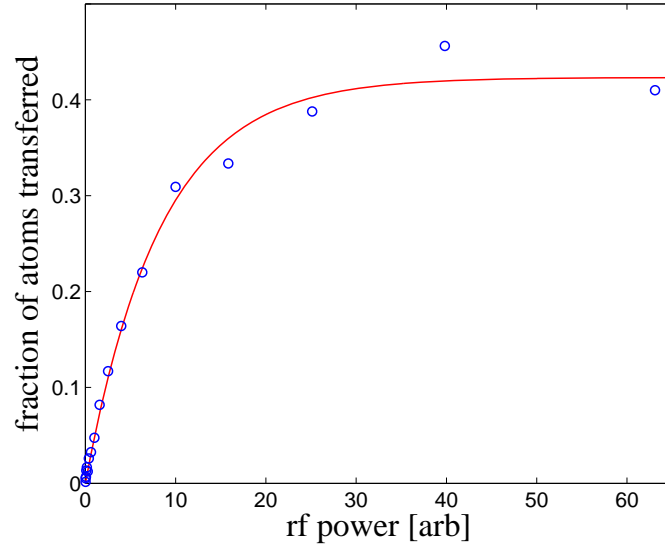
Figure 4.6: Saturation with increasing rf power at a detuning of 45 MHz. Note the absence of coherent oscillations for larger detunings. The solid line is a fit to the exponential model introduced in the text.

donut-mode beams, for a gas at unitarity with ~ 80000 atoms per spin state and $E_F/h = 7700$ Hz, with h being the Planck constant. The temperature of the gas, $T/T_F = 0.13$, was measured before ramping to the resonance field.

For small detunings, we observe oscillatory behavior reminiscent of coherent Rabi oscillations (figure 4.5a). For large detunings, the transfer is incoherent (see figure 4.6), and the number of outcoupled atoms saturates to a value that is between a quarter and a half of the total number of atoms (depending on the rf detuning). We fit the data to $N_{\text{outcoupled}} = A(1 - e^{-P/P_0})$ to find the saturation power P_0, where $N_{\text{outcoupled}}$ is the number of atoms outcoupled by the rf pulse with power, P. The results are given in figure 4.7. For the lowest detuning, where coherent effects exist, we fit the signal up to the first peak (figure 4.5b). We see that P_0 increases with increasing detuning, allowing us to continually increase the rf power as we measure further out on the tail of the line shape.

When measuring the rf line shape we keep the power less than $P_0/5$, where the number of atoms transferred by the rf pulse is small compared to the total number of atoms. Below this power, the linear approximation, $N_{\text{outcoupled}} \approx A\frac{P}{P_0}$, is correct to within 10%. By keeping our rf power in the "linear regime," we stay on the linear rising edge of the curves in figures 4.5 and 4.6. In this regime, we outcouple only about 20% of the total atoms, and the number outcoupled is not yet affected by the depletion of the atoms in the original state. As we increase the rf detuning, we also increase the power to always outcouple about 20% of the atoms. Afterwards, we linearly scale down the number of atoms at each detuning to match the number that would have been outcoupled by the power used for the central part of the line shape.

4.3   Local contact vs. (local) $\mathbf{T/T_F}$

The main result of these experiments, namely the contact of a homogeneous gas as a function of temperature, is presented in figure 4.8. The contact is normalized to the average k_F of the probed sample, and temperature is given in terms of T/T_F, with T_F being the average Fermi temperature of the probed sample. (These quantities are extracted from the average density,

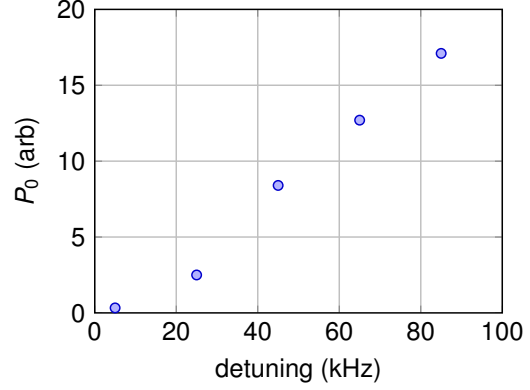| detuning [kHz]	P_0 [arb]
5	0.33
25	2.5
45	8.4
65	12.7
85	17.1

Figure 4.7: **The measured saturation power, P_0, in arbitrary units, for different rf frequency detunings.** This power is extracted from fitting to curves of $N_{outcoupled}$ versus rf power, as seen in figures 4.5 and 4.6. We choose this power in order to stay in the "linear regime" and outcouple about 20% of the atoms.

which I'll explain how we obtain in section 4.3.1.) The data show a monotonic decrease of the contact with increasing temperature from a maximum value of 3.3 Nk_F. For $T/T_F = 0.16$, at the edge of our experimentally attainable temperatures, we observe a sharp decrease of the contact to about 2.6 Nk_F. In figure 4.8, we compare our data with several theoretical models [66] and a quantum Monte-Carlo (QMC) simulation [68]. The many-body theories are in the framework of the t-matrix approximation, differing by their choice of the diagrammatic expansion, the particle-particle propagator, and the self-energy. For $T/T_F > 0.4$, the differences between the theoretical models are small, and the predictions all lie within the uncertainty of the data. As expected, at higher temperatures ($T/T_F > 1$), we also find good agreement with the virial expansions [66] (see inset of figure 4.8). For $T/T_F < 0.4$, our data do not agree fully with any of the many-body theories. It is worth noting, however, that two of the theories (GPF and G_0G_0) predict a higher value for the contact above the superfluid phase transition than below, which may be consistent with observed sharp decrease near $T/T_F = 0.16$. We note that the predicted T_c/T_F has some uncertainty, as indicated by the shaded region in figure 4.8. The non-self-consistent t-matrix model (G_0G_0) predicts an enhancement of about 50% in the value of the contact around T_c [65], which the data do not show. We also do not observe an increasing trend in the contact for $T > T_c$, in

contrast to a recent QMC simulation [68].

Thermometry of a strongly interacting gas is not trivial, and different groups have used various techniques, including thermometry with a minority component [4], measurement of the energy versus entropy relation [69], and an empirical temperature extracted from fitting the cloud to a Thomas-Fermi distribution [48]. We base our thermometry on a measurement of the release energy of the gas and the recently reported equation of state measured by the MIT group [36]. We determine the release energy by taking an image of cloud after 4 ms of expansion at unitarity. Knowing our trapping potential, the equation of state, and the generalized virial theorem at unitarity [69], we are left with only the temperature, T, as a free parameter in the calculation of the release energy. We estimate that the one sigma uncertainty in the temperature is 5%. When reporting T/T_F in figure 4.8, we use $T_F = E_{F,\mathrm{avg}}/k_B$. Appendix A includes the details of calculating the temperature using this technique.

4.3.1 Obtaining the in-situ density distribution

The contact is an extensive property with units of inverse length; it is naturally normalized by $N k_F$, as seen in equation 4.13. The rf detuning is often given in units of E_F. However, a question which arises is how to define k_F and E_F in our experiment. For a harmonically trapped gas, E_F is defined in terms of the trap parameters $E_{F,\mathrm{trap}} = \hbar(\omega_r^2 \omega_z)^{1/3}(6N)^{1/3}$. On the other hand, the Fermi energy of a homogeneous gas is given in terms of its density (in one spin state), n: $E_{F,\mathrm{hom}} = \frac{\hbar^2}{2m}(6\pi^2 n)^{2/3}$. In our experiment, as we increase the power of the hollow light beams, we probe a smaller portion of the gas that is more homogeneous. The relevant Fermi energy, which we use in figures 4.4 and 4.8, is therefore the average of the local (homogeneous) Fermi energy: $E_{F,\mathrm{avg}} = \frac{\hbar^2}{2mN_p}\int P(\mathbf{r})n(\mathbf{r})[6\pi^2 n(\mathbf{r})]^{2/3}\mathrm{d}^3\mathrm{r}$, where $P(\mathbf{r})$ is the detection probability after optical pumping, and $N_p = \int P(\mathbf{r})n(\mathbf{r})\mathrm{d}^3\mathrm{r}$ is the number of atoms probed.

We measure the in-situ density distribution, $n(\mathbf{r})$, in order to calculate the average k_F and E_F of the probed atoms. To get $n(\mathbf{r})$, we use the fact that at unitarity the cloud expands hydrodynamically, and the dynamics are governed by the continuity equation [70, 27]. The solution for
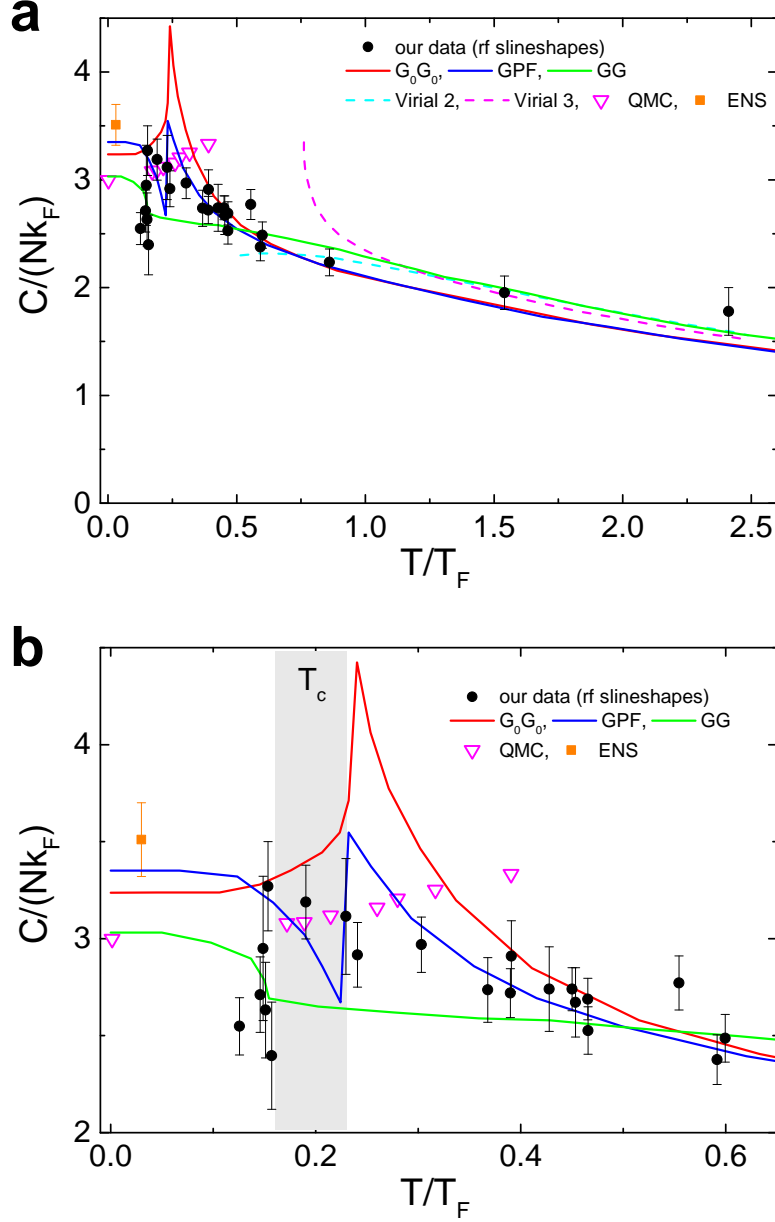
Figure 4.8: **The contact of a nearly homogeneous sample, versus** T/T_F **at unitarity.** We take the rf line shapes for clouds at unitarity and various temperatures and extract the contact from the high momentum part. We use our spatially selective imaging to look at only 30% of the spin flipped atoms, which come from the center of our trap. The contact is normalized by the total number of atoms and k_F, which we find by measuring the in situ density distribution and using our optical pumping model to calculate the average density of the probed atoms. We find T/T_F using the thermometry technique described in Appendix A. We present our data as black points and compare them to the three theories from figure 4.1 [66, 64, 65]. We also include the 2nd and 3rd order virial expansions [66], a quantum Monte-Carlo calculation (QMC) [68], and the contact extracted from a thermodynamic measurement done at ENS [4]. The error bars on our data represent one standard deviation. **a.** Our data show good agreement with the virial expansion at high temperatures, where the virial expansion is expected to be valid. **b.** The shaded area marks the superfluid phase transition, with some uncertainty in its exact position ($T_c/T_F = 0.16 - 0.23$) [64]. The differences in the theories are most obvious near the superfluid phase transition, and in this region, it is clear that the data do not fully support any one theory presented here.

the continuity equation with harmonic confinement with a time-dependent trapping frequency $\omega(t)$ is self-similar with the following scaling transformation: $r_i(t) = b_i(t)r_i(0)$, where r_i is the spatial coordinate ($i = x, y, z$), and $b_i(t)$ obeys the equation:

$$\ddot{b}_i(t) = -\omega_i(t)^2 b_i(t) + \frac{\omega_i(0)^2}{b_i(t)\left[b_x(t)b_y(t)b_z(t)\right]^\gamma} \quad , \tag{4.14}$$

with the initial conditions $b_i(0) = 1$ and $\dot{b}_i(0) = 0$. The constant γ is the characteristic exponent in the equation of state $\mu(n) \propto n^\gamma$, where μ is the chemical potential and $\gamma = 2/3$ at unitarity. For a sudden turn off of the trap, $\omega_i(0)$ is the trapping frequency along the i axis, and $\omega_i(t > 0) = 0$.

In figure 4.9, we plot the measured width of the cloud in the axial and radial directions as a function of the expansion time. The data show a rapid increase in the size in the radial (tight) direction of the cloud and almost no increase in the axial direction–a characteristic of hydrodynamic expansion. The solid lines show the numerical solution of equation 4.14 with $\omega_r = 2\pi \times 226$ Hz and $\omega_z = 2\pi \times 19$ Hz (which were measured independently), which agrees very well with the data. We find that after 4 ms of expansion the finite resolution of the optical imaging system does not affect the extracted parameters, and therefore we choose this expansion time for the density measurements. We fit the measured density profiles at 4 ms with a Thomas-Fermi distribution, which we find to be general enough for this purpose.

We have tested our density determination method by looking at the ratio of the peak density at unitarity to the peak density of a weakly interacting gas, at low temperatures. The density distribution of the weakly interacting gas is measured using a fit to a Thomas-Fermi distribution after ballistic expansion. For $T = 0$, this ratio is $n_U/n_0 = \xi^{-3/4}$, where ξ at unitarity is a universal constant that relates the chemical potential to the Fermi energy: $\mu = \xi\epsilon_F$ [71]. From the measured density ratio at a temperature of $T/T_{F,\text{trap}} = 0.15$, we extract a value of $\xi = 0.40 \pm 0.05$, which is consistent with recent determinations of this universal constant by other groups [36, 4].
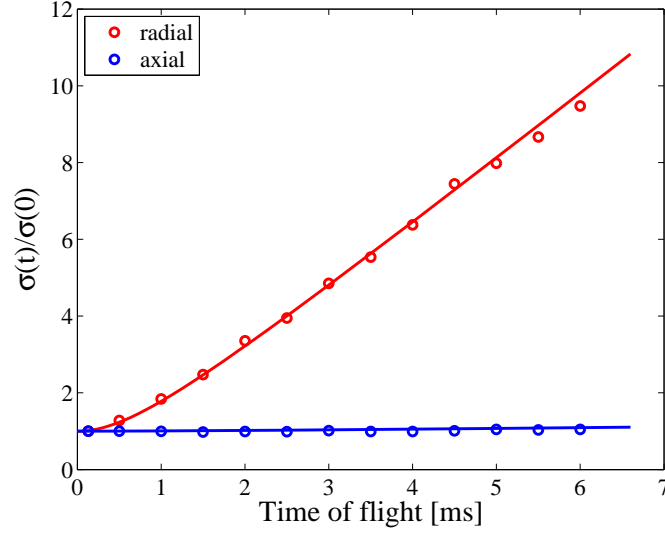
Figure 4.9: Hydrodynamic expansion at unitarity. We start with a weakly interacting gas with ~ 90000 atoms per spin state at $T/T_F = 0.12$ and ramp adiabatically to the Fano-Feshbach resonance field. We fit the cloud with a Thomas-Fermi distribution after a variable expansion time and extract the rms widths, $\sigma(t)$, in the radial and axial directions. For the data, we deconvolve the measured width with a Gaussian point spread function with an rms width of 2.9 μm, to account for the finite resolution of the optical system. The data is normalized by the initial cloud size, which is 33.4 μm and 2.8 μm in the axial and radial directions, respectively. The solid lines are the numerical solution of the hydrodynamic equation.

4.4   Modeling our results

We obtain $P(\mathbf{r})$, the probability to detect an atom after applying spatial selectivity, using the model of the optical pumping presented in section 3.4. We assume that atoms that scatter a single photon are transferred to the dark state, and we account for the attenuation of the hollow light beams as they propagate through the cloud. For a given $n(\mathbf{r})$, the propagation model gives us $P(\mathbf{r})$ after the consecutive application of the two hollow light beams.

In figure 4.10, we show the contact at $T/T_F = 0.46$ as a function of the fraction of atoms probed, which is varied by changing the intensity of the hollow light beams. The main part of figure 4.10 shows the contact per particle in units of $k_{F,\text{trap}}$ in order to show the change in the measured signal. We find that the signal increases as we probe fewer atoms near the center of the trapped gas. We compare our results with several theoretical models, where the model lines are
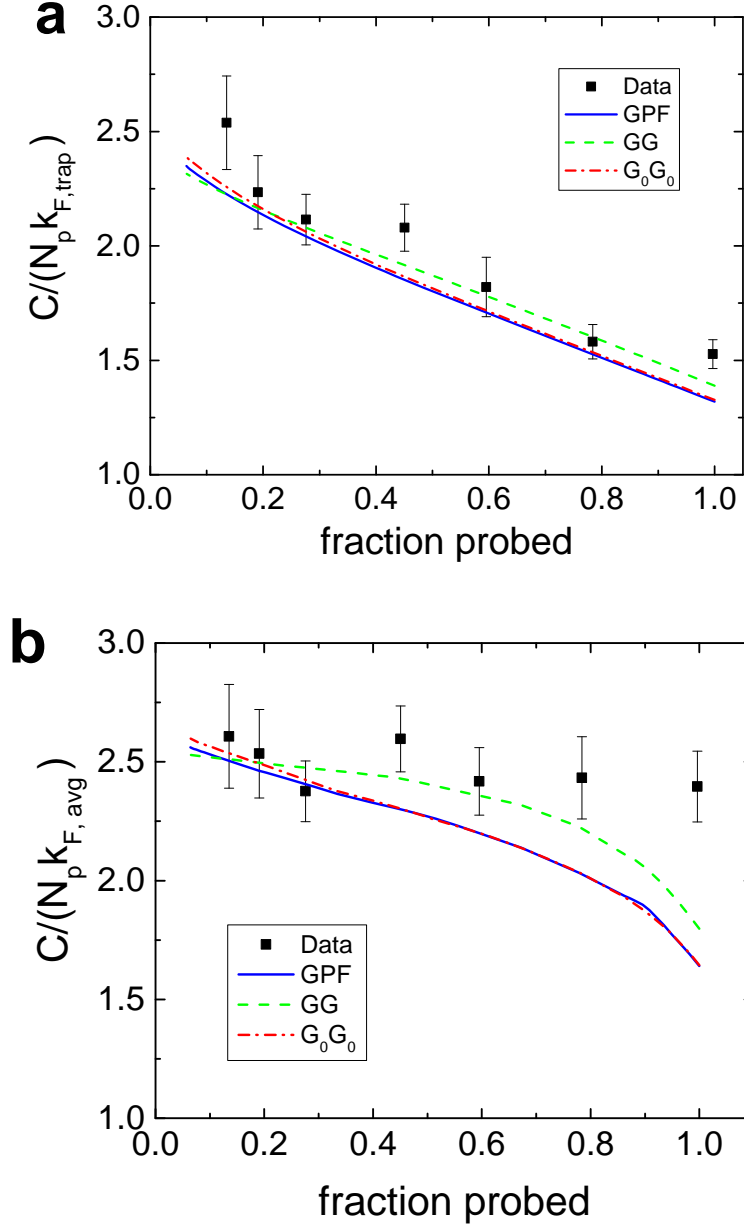
Figure 4.10: **Contact versus the fraction of atoms probed for a gas with** $T/T_F = 0.46$ **at the center of the cloud. a** The measured contact (squares), normalized by the trap k_F, is compared to the predictions of several theoretical models (lines) using the local density approximation. The measured contact increases as we probe fewer atoms at the cloud center, where the local density is largest. **b** Here, the contact is normalized by the average k_F of the probed atoms (squares) and is compared to theoretical predictions of the homogeneous contact at the average T/T_F (lines).

calculated by $C_{\text{trap}}^{\text{model}} = \frac{1}{N_p k_{F,\text{trap}}} \int P(\mathbf{r})n(\mathbf{r})C_{\text{hom}}^{\text{model}}[T/T_F(\mathbf{r})]k_F(\mathbf{r})\mathrm{d}^3\mathbf{r}$, with $C_{\text{hom}}^{\text{model}}(T/T_F)$ being the

model prediction for a homogeneous contact (normalized to Nk_F), $T_F(\mathbf{r}) = E_F(\mathbf{r})/k_B$ is the local

Fermi temperature, and k_B is the Boltzmann constant. We find good agreement of the data with the models.

In figure 4.10 b, we plot the contact divided by the average local k_F, defined in the same way as in figure 4.8. For comparison, we also plot theory predictions for the homogeneous contact at the average T/T_F, $C_{\text{hom}}^{\text{model}}(\langle T/T_F \rangle)$, where the notation $\langle \rangle$ stands for density-weighted averaging. A reasonable criterion for homogeneity is when $C_{\text{hom}}^{\text{model}}(\langle T/T_F \rangle) \approx \langle C_{\text{hom}}^{\text{model}}(T/T_F) \rangle$. When the fraction of the atoms probed is less than 30% we find that this approximation holds to better than 2%. When probing 30% of the atoms, we calculate that the rms spread in the local T_F has been reduced to about 20%. We find that the data for $T/T_F = 0.46$ and fractions lower than 30% agree with theory predictions for a homogeneous gas.

4.4.1 The effect of the remaining density inhomogeneity

In figure 3 in the paper, we compare our data to the predictions of several theoretical models. Here we show that the effect of the remaining density inhomogeneity of the probed sample on the theory predictions is negligible. We use the detection probability, $P(\mathbf{r})$, and the density distribution, $n(\mathbf{r})$, for each of the data points, to calculate the average contact predicted by each theoretical model according to:

$$\langle C \rangle = \frac{1}{N_p \langle k_F \rangle} \int P(\mathbf{r}) n(\mathbf{r}) C_{\text{hom}}^{\text{model}}[T/T_F(\mathbf{r})] k_F(\mathbf{r}) \mathrm{d}^3\mathbf{r} \quad , \tag{4.15}$$

where $C_{\text{hom}}^{\text{model}}$ is the prediction for the contact of a homogeneous gas theory (normalized to $N k_F$), N_p is the number of probed atoms, and $\langle k_F \rangle$ is the average k_F. The comparison of the average contact, $\langle C \rangle$, and the homogeneous contact for three different models is shown in figure 4.11. The graph demonstrates that (with 30% of the atoms probed) the effect of the remaining density inhomogeneity on the contact is negligible, and hence theories for the homogeneous contact can be compared directly to the data.
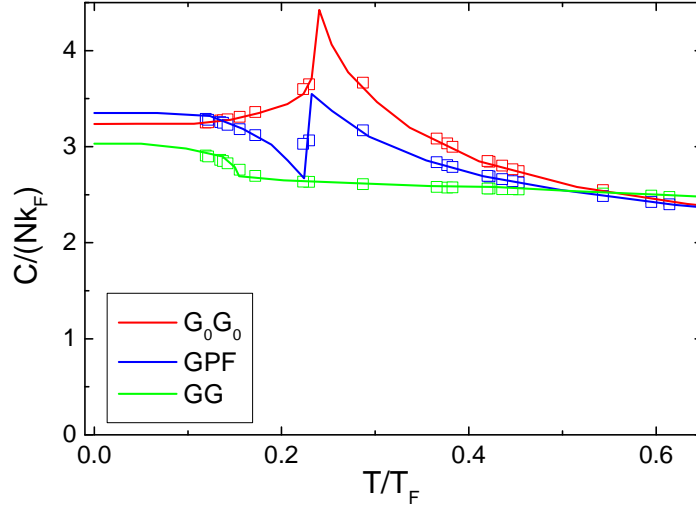
Figure 4.11: Comparison of the homogeneous contact calculated by several theoretical models (solid lines) and the contact averaged over the remaining density inhomogeneity when probing the central 30% of the cloud for the same models (open symbols). The excellent agreement of the points and the lines shows that the effect of the remaining density inhomogeneity on the contact data can be neglected.

4.4.2   The optical pumping model

To calculate the spatially dependent probability that atoms are probed, $P(\mathbf{r})$, we use a model for the optical pumping by the hollow light beams. In Ref. [43] we have introduced such a model, which was also tested experimentally. The calculated $P(\mathbf{r})$ along with $n(\mathbf{r})$ is used in our determination of the average quantities (density, k_F, T_F, E_F and the contact) of the probed atoms. We show here that the results presented in this paper are not sensitive to the details of the optical pumping model.

To show this, we introduce a second, much more simplified model, which we refer to as the "sharp cut" model. In the sharp cut model, we assume that atoms are left for probing only if their position (x, y, z) satisfy $x^2 + y^2 < R_1^2$ and $z^2 + y^2 < R_2^2$, where R_1 and R_2 are set to reproduce the fraction of atoms probed after the application of one or both of the hollow beams. In figure 4.12, we present the homogeneous contact, similar to figure 3 in the paper, but using the two different models. As can be clearly seen in the figure, the results of the two models are essentially the same,
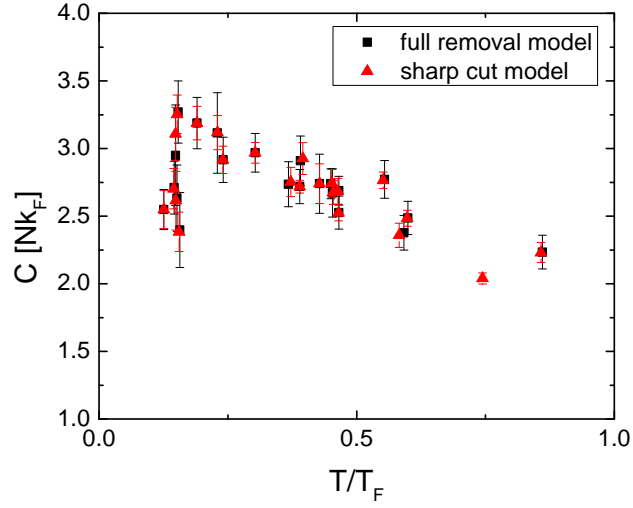
Figure 4.12: The homogeneous contact at unitarity as function of the temperature, using the full removal model (squares) and the sharp cut model (triangles). The good agreement of the two models shows that the exact shape of the detection probability, $P(\mathbf{r})$, does not affect the contact data. This is because the central part of the trapped gas is nearly homogeneous, and the data was taken probing the central 30% of the atoms.
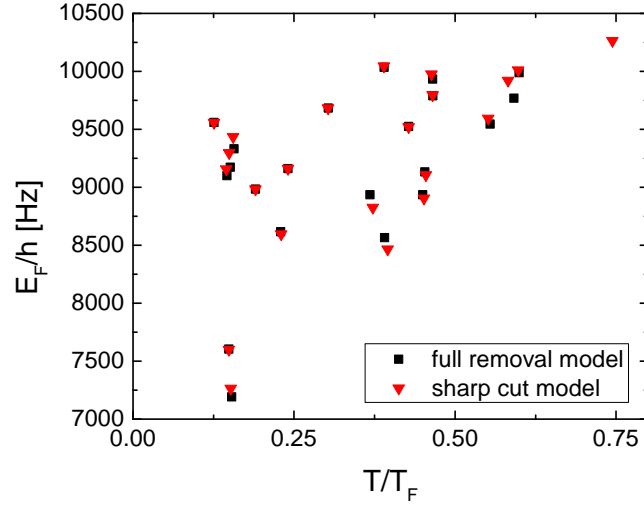

Figure 4.13: The average Fermi energy with $\sim 30\%$ of the atoms probed, using the full removal model (squares) and the sharp cut model (triangles).

which demonstrates that the details of the calculation of $P(\mathbf{r})$ are not important when the fraction

of atoms probed is as small as 30%. In figure 4.13, we show the average Fermi energy for the data,

where again the two models give consistent results.

4.5 Conclusions

The results presented here are the first measurement of the temperature dependence of the contact for a nearly homogeneous Fermi gas. The data show good agreement with theory at "high" temperatures—$T/T_F > 0.4$ or so—but also have a sharp feature near where the superfluid transition occurs. This feature was not seen in previous contact versus temperature measurements presumably because averaging the signal over a spread of densities within the trap smoothed it out. Furthermore, near the phase transition no single prediction fully agrees with the data.

It is our hope that this data will prove useful for theorists attempting to understand the unitary Fermi gas. The contact is a useful parameter for many reasons; not only is it straightforward to measure in experiment, the Tan relations make it fairly straightforward to calculate from theory, too. In particular, equation 4.6 shows that the contact can be directly taken from the dependence of energy on scattering length, which is often calculated in theory.

Since no theory fully predicts the behavior that we see, we cannot say that our data supports one picture of the unitary Fermi gas over another. While an important and useful thermodynamic parameter, it is also not clear how the contact can connects the state of the system, particularly around the superfluid phase transition. In particular, it would be interesting to know more about the so-called "pseudogap regime" in the normal state in the crossover, just above the critical temperature. In the next chapter, I will present our efforts to directly probe the nature of the normal state using momentum-resolved rf spectroscopy. In that work, we develop a more detailed picture of a Fermi gas in the crossover, and we find a surprising connection between our photoemission spectroscopy results and the contact.

Chapter 5

The occupied spectral function of a homogeneous gas in the normal phase

This chapter describes our work measuring the local properties of a strongly interacting Fermi gas in the normal phase of the BCS-BEC crossover. While the ground state of the Fermi gas in the crossover is well established and studied, the nature of the normal state—whether it can be thought of as a Fermi liquid with well-defined quasiparticle excitations or whether is exhibits signatures of uncondensed pairs, as expected for the pseudogap regime—is still a topic of ongoing research.

We measure the spectral function of our atoms using atom photoemission spectroscopy (PES) (realized with momentum resolved rf spectroscopy), which is a technique developed by our group in 2008 [1, 72]. This technique is closely analogous to a condensed matter technique used to probe high-Tc superconductors. With PES, we can measure the probability to find atoms at specific momenta and energies; this is called the spectral function. The energy and momenta dispersion we measure can tell us about the nature of the gas and the state of individual atoms (i.e. paired, unpaired, and so forth). Previously, our lab has measured spectral functions for a gas in the normal phase, which showed evidence of pairing [73, 74]. However, these measurements came from an inhomogeneous sample, and the results were therefore difficult to quantify without relying on theory. This consideration, and the simultaneous measurements of the equation of state in Paris and Tokyo that agreed with a Fermi liquid description of the normal phase [5, 35] convinced us that PES on a homogeneous sample was necessary to understand our system.

In this chapter, I discuss PES measurements that used our spatially selective imaging technique. This turns out to be essential to our ability to understand and quantify our results. The

work in this chapter has been published in Ref. [75].

5.1   The normal state of the BCS-BEC crossover

In section 1.2.1 of this thesis, I introduced the BCS-BEC crossover as the theory describing the ground state of a system of interacting fermions. For weak attractive interactions, the gas at zero temperature is a superfluid of paired fermions that behave like Cooper pairs. For increased interactions, the gas remains a paired superfluid at low temperatures, and for very strong interactions, those pairs resemble bosonic dimers in a molecular BEC. [19, 27, 76, 77, 78]

But what happens to the normal state (i.e. the gas in the non-superfluid regime at finite temperature) is also a critical part of the BCS-BEC crossover. On the BCS side of the crossover (weak attractive interactions), the gas should resemble a nearly non-interacting Fermi sea. If the interaction strength is adiabatically swept across the Fano-Feshbach resonance, on the far BEC side of the crossover the atoms will form uncondensed, bosonic Fano-Feshbach molecules. How the gas evolves from an ensemble of fermions to an ensemble of bosons is extremely interesting and is the subject of ongoing research.

A well-established and powerful paradigm for describing systems of interacting fermions is the theory of Fermi liquids, which was developed by Landau in 1956 [79, 80]. It postulates that even in the presence of strong interactions, the system retains a Fermi surface and has low energy excitations that are long-lived, fermionic, and nearly non-interacting. The effect of interactions is incorporated into renormalized properties of these quasiparticle excitations, such as an effective mass, m^*, that is larger than the bare fermion mass, m, and a spectral weight, or quasiparticle residue, that is between zero and one [80].

While Fermi liquid theory is extremely successful in describing a wide range of materials, it fails in systems exhibiting strong fluctuations or spatial correlations. Understanding the breakdown of a Fermi liquid description is an outstanding challenge in strongly correlated electron physics [81]. If the normal state in the crossover can be described as a Fermi liquid for some range of interaction strengths, there must be an interaction strength at which it fails, either before or as the atoms form

localized dimers.

The question of how the Fermi liquid paradigm breaks down in the normal state of the Fermi gas in the crossover is related to the prediction of a "pseudogap" phase, where incoherent many-body pairing occurs for strong interactions and just above the transition temperature T_C [77]. This pseudogap phase has bosonic (pair) excitations, in contrast to the fermionic excitations of a conventional Fermi liquid. However, unlike true, tightly bound bosonic molecules that would be found in the BEC limit, these bosonic pairs have a binding energy that is on the order of or less than the Fermi energy, and the pairs are as large as or larger than the average interparticle spacing. In the pseudogap region near unitarity, pairing occurs between atoms with similar momenta close to the Fermi momentum, $\hbar k_F$, and the pairing is facilitated by the presence of a Fermi surface and Fermi statistics, a very different picture from the two-body dimer.

While much experimental investigation into the nature of atoms in the normal phase of the crossover had been carried out prior to the work presented in this chapter, no consensus had been reached. In experiments that probed the strongly interacting gas in the middle of the crossover, Fermi-liquid-like behavior was observed in thermodynamic [35, 4] and spin transport properties [82]. Meanwhile, evidence for pairing above T_C was reported in photoemission spectroscopy (PES) measurements [73], which reveal the distribution of single-particle energies and momenta in a many-body system [1, 83]. Interpretation of these data has been controversial, with a Fermi liquid theory and a pseudogap theory each separately argued to agree with the observations [84, 74, 85]. Issues raised include the fact that the PES measurements probed a trapped gas, where averaging over the inhomogeneous density can obscure the intrinsic physics [84, 86], and that thermodynamics measurements are relatively insensitive to a pseudogap compared to spectroscopy. Thus, the question of how a Fermi liquid evolves into a Bose gas of paired fermions in the BCS-BEC crossover, and how the Fermi liquid description breaks down, remains open.

5.2   Photoemission spectroscopy

We approach this question of the nature of the normal state by probing the energies and momenta of the atoms in our system above T_C and at various interaction strengths throughout the crossover. We combine our new technique of imaging a uniform density portion of our gas with the technique of atom photoemission spectroscopy (PES) to measure the occupied part of the spectral function of a homogeneous gas.

Atom photoemission spectroscopy was developed in our lab as an analog to angle-resolved photoemission spectroscopy (ARPES) used to probe electronic systems. ARPES uses the photoelectric effect, in which photons incident on a sample can kick out electrons from a material. If the energy and velocity of both the initial photon and the ejected electron are known, conservation of energy and momentum will reveal the energy and momentum of the electron in the sample. By varying the initial photon angle with respect to the sample, ARPES can be used to measure the probability that an electron will be found in a particular energy and momentum state, which yields the occupied part of the electrons' spectral function. A diagram of the ARPES technique is shown in figure 5.1.

Similarly, our goal is to take our strongly interacting atoms and measure the probability to find an atom at a particular energy and momentum. As with electrons in a solid, the shape of this dispersion will tell us about the microscopic details of the system—paired, unpaired, non-interacting, liquid-like, and so on. In atom PES, the "photo-ejection" occurs when a pulse of rf light outcouples atoms from one of the interacting spin states to a third spin state that is only weakly interacting with the other two. Simultaneously, the confining optical potential is switched off. These steps allow us to project some of our interacting atoms very quickly onto non-interacting states in free space, just as the photo-ejection of electrons does in ARPES. By allowing the non-interacting atoms to expand for some time of flight (TOF), we are able to measure the distribution of velocities/momenta in the ejected atoms. One difference between atom PES and ARPES is that, since there is no underlying lattice and the inter-atomic interactions are engineered to be s-wave,
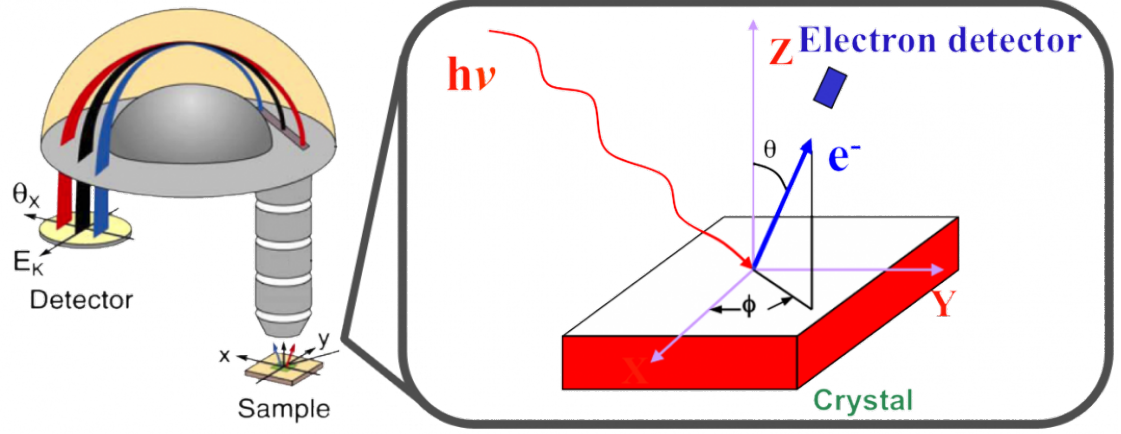
Figure 5.1: **Angle resolved photoemission spectroscopy (ARPES).** In ARPES, a photon incident on a surface kicks out an electron (right), which is then collected by a detector after some time of flight (left). The velocity of the ejected electron and its angle with respect to the incident beam are recorded. Taking these and the energy of the incident photons into account, researchers can solve for the energy and transverse momentum of the electrons in the crystal. This diagram is reproduced from Ref. [11] and the Stanford Shen Laboratory website [87].

the distribution of velocities for the atoms is spherically symmetric. Figure 5.2 shows a diagram of the atom PES technique. [1]

5.2.1   The experiment

We begin this experiment by preparing a gas of ^{40}K atoms in an equal mixture of two spin states, $|9/2, -9/2\rangle$ and $|9/2, -7/2\rangle$. The temperature of the atoms after evaporation is $T_0 = (0.16 \pm 0.02)T_F$ with $80,000$ to $120,000$ atoms per spin state. The atoms are held in an optical dipole trap, and the trapping frequencies at the end of evaporation are 243 Hz and 21.3 Hz in the radial and axial directions, respectively.

We use the Fano-Feshbach resonance between these two spin states to control interactions [19, 73]. The final stage of evaporative cooling is performed at a magnetic field of 203.3 G where $a \approx 1100a_0$ (a_0 is the Bohr radius), after which the field is swept linearly in 50 ms to the final value where we carry out the PES measurement (see figure 5.3).

---

[1] An alternate spectroscopy technique to measure occupied spectral functions was proposed prior to the development of the "atom PES" presented here [88]. This technique uses two-photon Raman transitions instead of single photons of MHz frequencies to transfer atoms to an unoccupied Zeeman state.
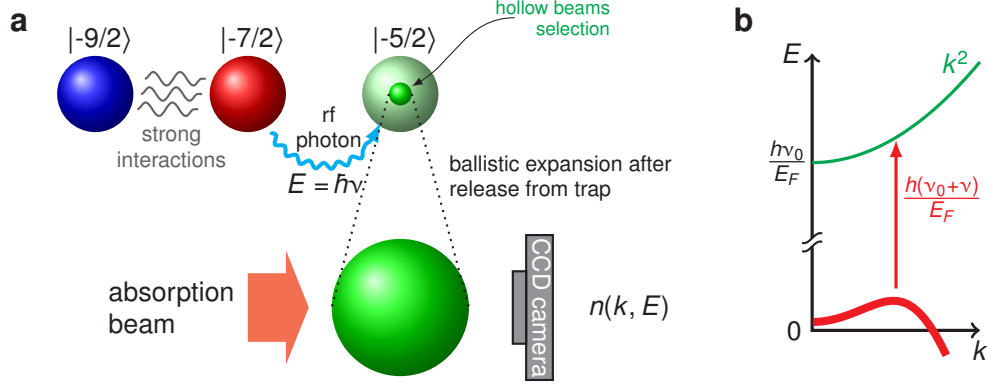
Figure 5.2: **Atom photoemission spectroscopy (PES). a.** In our PES experiments, we start with an equal mixture of atoms in the $|9/2, -9/2\rangle$ and $|9/2, -7/2\rangle$ states, with a Fano-Feshbach resonance controlling their interactions. An rf photon moves some atoms from the $|9/2, -7/2\rangle$ state to the $|9/2, -5/2\rangle$ state, which does not interact with the first two states. Nearly simultaneously with the rf pulse, the hollow light beams are pulsed and the trapping potential is turned off. The atoms expand and fall during time of flight, and we take an image of only those atoms selected by the hollow beams. **b.** The signal that we measure from PES is constructed through energy and momentum conservation. By measuring the momentum of the outcoupled atoms (green line), we know the momentum of the atoms in the trap, and we can use the rf photon energy to also get the energy of the atoms in the trap (red line). The shape of the measured dispersion (red line) tells us something about the state of the interacting system (the back-bending seen here can be indicative of BCS-like pairing).

Figure 5.3: **PES sequence timing.**

It is important to note that this field sweep is adiabatic, which means the gas ideally stays at constant entropy but not necessarily constant temperature. T_0, the temperature of the atoms at

203.3 G before the final field sweep, was chosen such that the final temperature is just above T_C after sweeping to the Fano-Feshbach resonance at 202.20 G [73]. From our previous measurements of the release energy 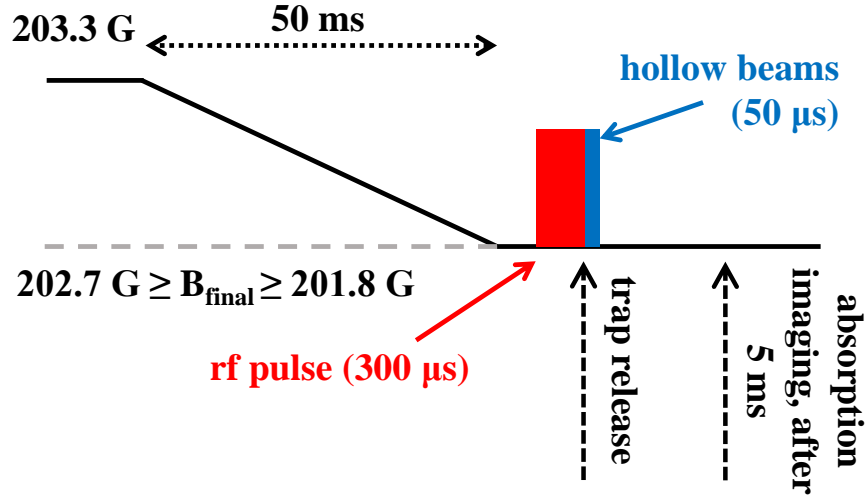at unitarity [49], we estimate that the temperature after a sweep to unitarity increases from $T_0 = (0.16 \pm 0.02)T_F$ to $(0.18 \pm 0.02)T_F$. Using the pair projection technique from Ref. [25], we verified that for all interaction strengths the condensate fraction is less than 1%. [2]

The atom PES measurement uses an rf pulse with a Gaussian field envelope that has an rms width of 51 μs (17 μs), and a total duration of 300 μs (100 μs), for $\nu < 34$ kHz ($\nu \geq 34$ kHz) (see figure 5.3). We use shorter pulses at higher ν to minimize effects due to the motion of the spin-flipped atoms during the rf pulse. The rf detuning ν is given with respect to the resonant transition frequency ν_0, which is measured for a spin-polarized gas. For each PES data set, we take data for the same 25 values of ν, each of which is repeated three times. The rf power is increased for larger ν while keeping the fraction of spin-flipped atoms less than 40%. As we did when measuring the contact (chapter 4), we measure the dependence of the number of spin-flipped atoms and scale the measurements done at different rf powers to correspond to a common level (see Appendix B for more details).

Immediately after the rf pulse, and exactly at trap release, we pulse on the hollow-core light beams, which propagate perpendicularly to each other and intersect at the center of the cloud [43, 49]. The frequency of these beams is chosen to optically pump atoms from the $|9/2, -5/2\rangle$ state into the upper hyperfine manifold ($F = 7/2$), where they are invisible to our imaging (see figure 5.4). Both the rf pulse and the spatially selective optical pumping, which is pulsed for 40 μs, are completed in a timescale that is short compared to motion of atoms in the trap. We typically probe the $|9/2, -5/2\rangle$ atoms that came from the central 30% of the cloud; we find this fraction to be a good compromise between spatial selectivity and signal-to-noise ratio [43, 49]. As described in chapter 4 and Ref. [49], just before imaging the cloud, we remove the remaining atoms from the $|9/2, -9/2\rangle$ and $|9/2, -7/2\rangle$ states and then transfer the outcoupled atoms in the $|9/2, -5/2\rangle$ state

[2] Measuring the temperature of an interacting Fermi gas away from unitarity is thus far beyond the limits of what we know how to do. At unitarity, we can rely on other groups' measurements of the equation of state[4, 5, 36]. However, this measurement is only valid if the gas is at a single $(k_F a)^{-1}$, which only happens if $a \to \infty$.

to the $|9/2, -9/2\rangle$ state with two short rf π-pulses. This procedure enables us to image the atoms on the cycling transition, which improves the signal-to-noise ratio.
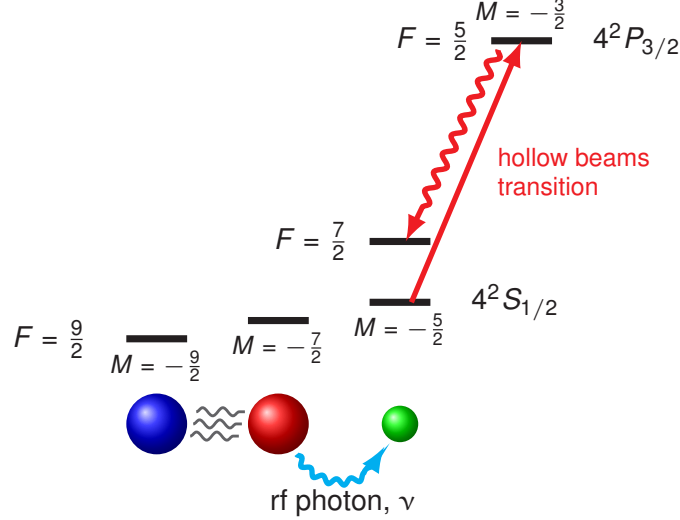
Figure 5.4: **Schematic level diagram of ^{40}K energy states relevant to the experiment.** The gas is prepared in an equal mixture of two hyperfine states. These two states, that can be made strongly interacting near a Fano-Feshbach resonance, are $|9/2, -9/2\rangle$ and $|9/2, -7/2\rangle$, where the first number is the total atomic spin F and the second number is its projection M. For photoemission spectroscopy, an rf pulse drives the transition from the $|9/2, -7/2\rangle$ state to the $|9/2, -5/2\rangle$ state, which is weakly interacting with the two other spin states. Also shown are the transition driven by the hollow-core light beams (straight red arrow) and the spontaneous emission transition with the largest Clebsch-Gordan coefficient (curvy red arrow).

5.2.2 The PES signal

Each PES data set consists of 75 images of the atoms each taken after 5 ms time of flight. One such image is displayed in figure 5.5**b**, which corresponds to the detuning shown in red on the rf line shape (figure 5.5**a**). Images taken for the same detuning are averaged together, and the radial momentum distribution is extracted by performing an azimuthal average and an inverse Abel transform on the image. The inverse Abel transform maps the 2D projection onto a 3D image of the full cloud, and the azimuthal average sums over the azimuthal direction to get the radial momentum distribution, $n(\mathbf{r})$.

A full PES dispersion plot is constructed from 25 momentum distributions, each at different
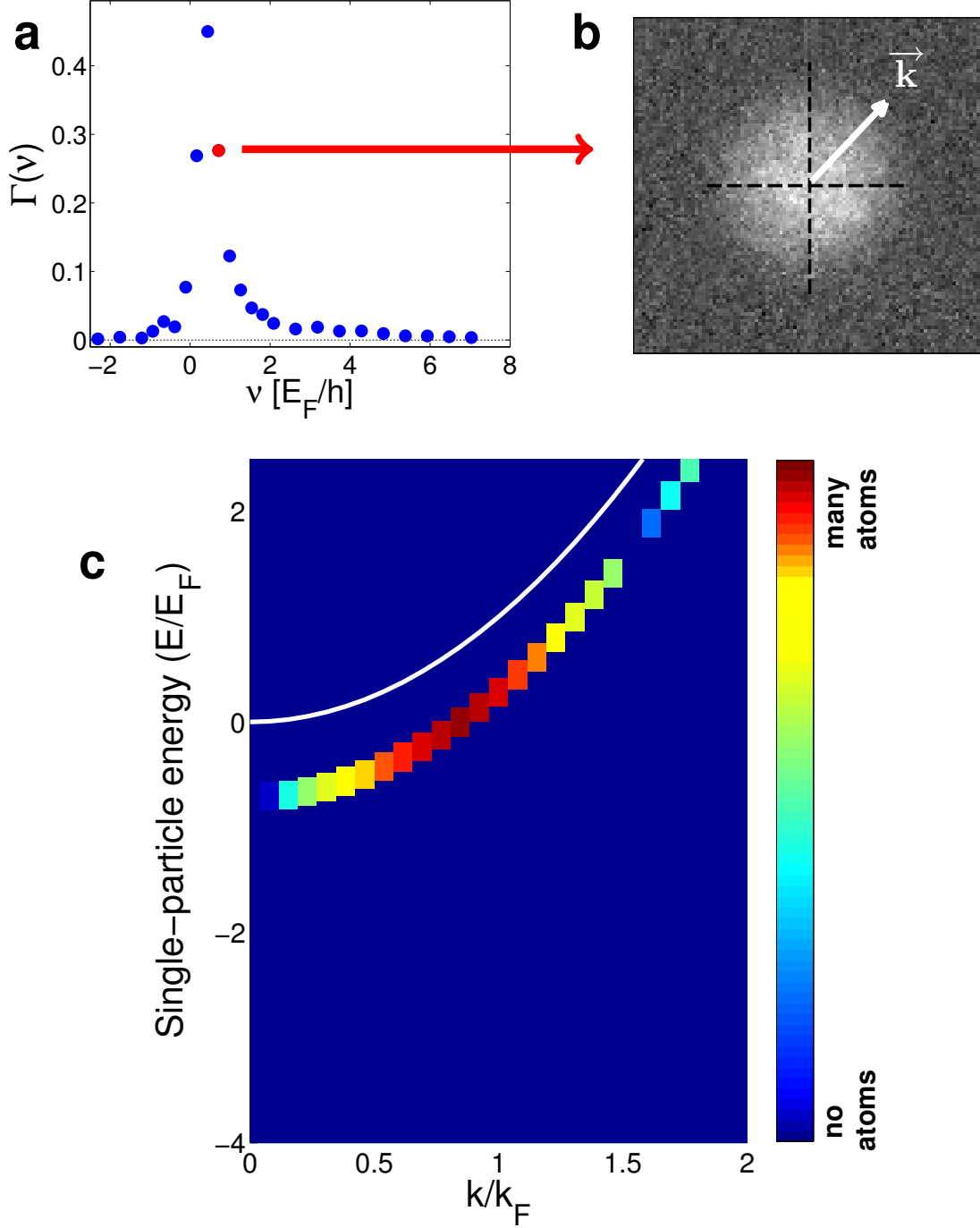
Figure 5.5: **Creating the PES plots. a.** A line shape showing the relative fraction of atoms outcoupled at each rf detuning. The line shape is normalized such that $\int_{-\infty}^{\infty} \Gamma(\nu)d\nu = 1/2$, due to the $50\% - 50\%$ spin mixture. **b.** An image of an atom cloud, taking for the detuning marked in red on the line shape ($\nu \approx 6.5$ kHz). In our analysis, this image will be averaged with 2 others at the same detuning, and the momentum distribution will be extracted from the atoms' TOF positions. **c.** The contribution of a single image to a full PES dispersion plot. The image in **b** is shown after extracting the momentum distribution. The color corresponds to the fraction of the atoms having a specific momentum. Each frequency on the line shape (**a**) will add a parabolic strip of dispersion data to the plot. Each strip is shifted from the bare transition (the white line, also called the free-particle line) by $-\hbar\nu$.

detunings. Using energy conservation, the detuning of the rf and an atom's final momentum can be used to find the energy of the atom before "photo-ejection." Each detuning corresponds to a parabolic slice of the plot:

$$E_{\text{after spin flip}} = E_{\text{before spin flip}}$$
$$\frac{\hbar^2 k^2}{2m} = h\nu + E;$$

(5.1)

where E is the energy of a single atom in the strongly interacting sample. The distribution of momenta along that slice is shown by the color. (Note that positive detunings yield $E = -\hbar\nu$ for zero momentum.) Figure 5.5**c** shows the single slice of the PES dispersion plot that comes from the image shown in 5.5**b** ($\nu \approx 6.5$ kHz). The final signal from PES is displayed in a 2D plot created when data from all frequencies are combined.

The PES signal, $I(k, E)$, is proportional to the probability to find an atom in the interacting gas at a particular energy, E, and momentum, k. This signal is proportional to $k^2 A(k, E) f(E)$, where $A(k, E)$ is the atomic (single-particle) spectral function [1, 89], and $f(E)$ is the Fermi function. As in chapter 4, we use the contact extracted from the rf line shapes when we normalize the PES data so that $\int_{-\infty}^{\infty} \left(\int_0^{\infty} I(k, E) \mathrm{d}k \right) \mathrm{d}E = 1$. Since the PES data span a finite range of E and k (typically, $-4 < E < 3$ and $k < 4$), knowing the behavior of $\Gamma(\nu)$ for large ν allows us to account for signal beyond the range of the data in our normalization of the PES data.

Since we eject, or spin flip, atoms from the interacting gas, we only measure the *occupied* part of the spectral function. If we wanted to measure unoccupied states, one would need a different technique that somehow populated those higher energy states; this might involve the injection of non-interacting atoms into the strongly interacting gas (inverse PES) or the forced excitation of atoms into the unoccupied bands. [3]

Figure 5.6 shows $I(k, E)$ measured for 11 different values of $(k_F a)^{-1}$ in the BCS-BEC crossover at a temperature above T_C. The color encodes the likelihood that an atom will be in the corresponding energy/momentum state. The y-axis shows the energy in units of the Fermi

---

[3] The development of a technique to measure the unoccupied higher energy states would be a great project for the near future!

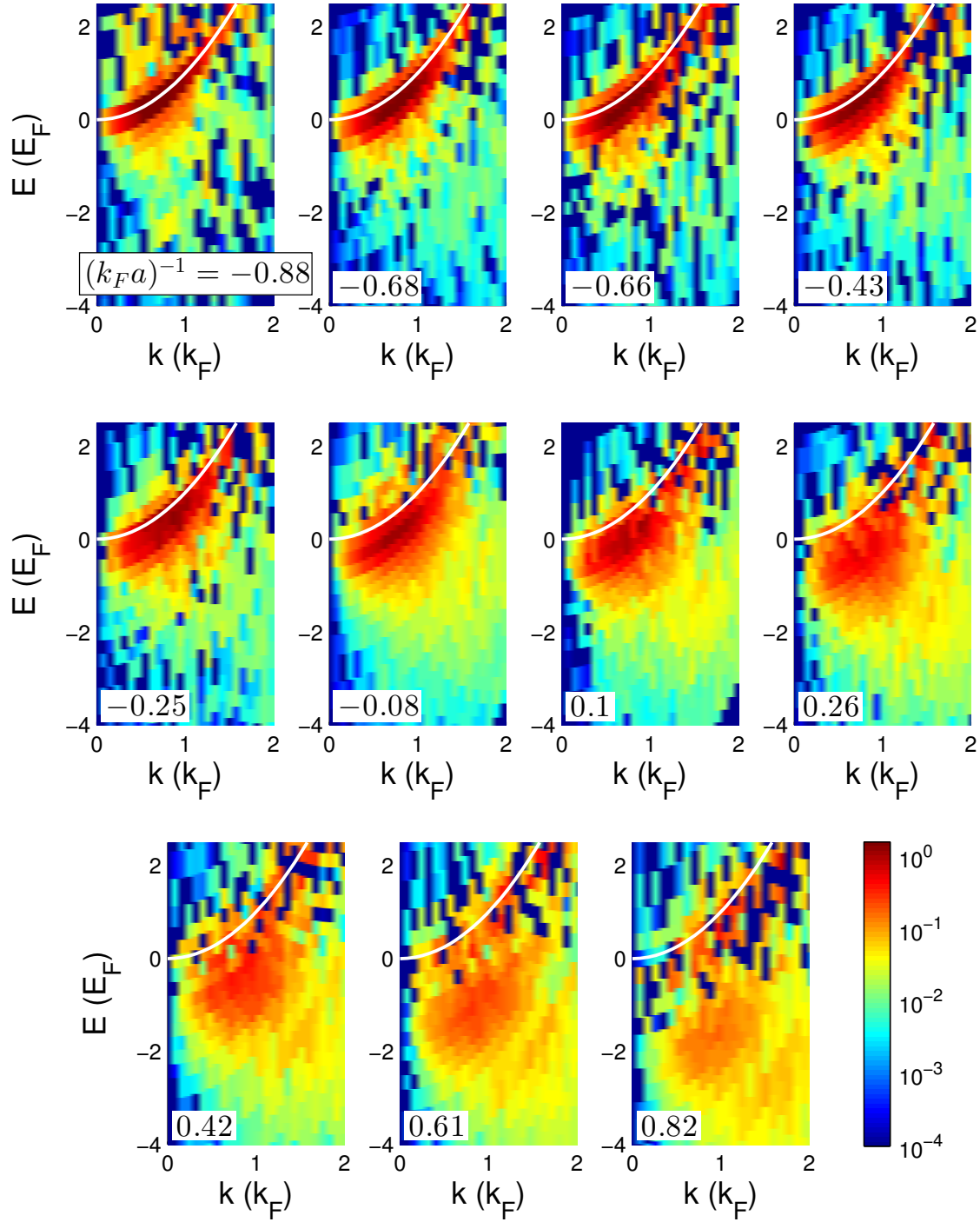Figure 5.6: **Atom photoemission spectroscopy (PES).** In these plots of PES data, the color encodes the probability distribution of atoms at a given E and k in the strongly interacting gas. We estimate that the error bar of $(k_F a)^{-1}$ is 0.03. $E = 0$ is the energy of a free atom at rest and the white line shows the free-particle dispersion $E = k^2$. Here, E is in units of E_F, k is in units of k_F.

energy, E_F, and the x-axis shows the momentum in units of the Fermi wavevector, k_F. The white parabolas show the dispersion of non-interacting atoms (the "free-particle line"). Zero energy was found by measuring the transition energy of a spin polarized gas of $|9/2, -7/2\rangle$ atoms.

E_F and k_F, which scale the axes of the figure 5.6, are calculated from the average density of the probed gas. As when we measured the contact in chapter 4, the average density is determined from the central part of the *in-situ* density distribution of the gas (see section 4.3.1). For that experiment, we took a picture of our gas after a small TOF expansion, keeping the gas at the Fano-Feshbach resonance. Expansion of a gas at unitarity is hydrodynamic and well characterized by previous measurements [70, 27]; this allows us to back out the density distribution in trap from the expanded cloud image. Throughout the BCS-BEC crossover, the expansion is also hydrodynamic, although the rate of expansion differs from that at unitarity. We deduce the in-situ density distribution by solving the Euler equation with a scaling solution that assumes the chemical potential is proportional to n^γ, where n is the density, and γ depends on the interaction strength (see section 4.3.1 and Ref. [27] for the equations describing this scaling). For the purpose of this work, we use γ as approximated by the Leggett ansatz [27]. After finding the in-situ density distribution, we use our model of donut beam removal (presented in section 3.4) to find the density distribution of the selected atoms and take the average density-weighted density.

The PES data in figure 5.6 show several trends as a function of $(k_F a)^{-1}$. For the point at $(k_F a)^{-1} = -0.88$, which is the furthest on the BCS side, $I(k, E)$ shows a maximum centered on the free particle line with a relatively narrow spread in energy for any given k. As interactions increase, the maximum signal in $I(k, E)$ shifts down to more negative energies, and the spread in energy gets larger. By the time $(k_F a)^{-1} = 0.82$, which is the data set furthest on the BEC side, the spread in energy is quite large, and the data appear very different from the free particle dispersion.

Previous trap-averaged atom PES data showed back-bending and large energy widths [73, 74]. These features are also apparent in the nearly homogeneous data (shown in Appendix C). However, these data are more amenable to quantitative analysis because k_F (and E_F) are approximately single-valued across the sample. The remainder of this chapter explains how we implement such

a quantitative analysis, the results from this analysis, and the greater understanding it brings us about the nature of the normal state.

5.3   The two component fits

Similar to the analysis done in electron systems, we use a two-mode function to describe the PES signal [11]:

$$I(k, E) = Z I_{\text{coherent}}(k, E) + (1 - Z) I_{\text{incoherent}}(k, E) \quad , \tag{5.2}$$

where the first part describes quasiparticles with a positive dispersion, the second part accommodates an "incoherent background" that exhibits negative dispersion, and Z is the quasiparticle spectral weight. When these two parts (defined below) are combined, the resulting dispersion can exhibit back-bending.

5.3.1   The quasiparticle signal

The quasiparticles in Fermi liquid theory are long-lived and therefore give rise to narrow energy peaks, which, in principle, could be directly observed. However, such peaks would be broadened by our experimental resolution of about $0.25 E_F$. In practice, this resolution is difficult to improve. It is set by the number of atoms (with E_F scaling only weakly with increasing N) and the rf pulse duration, which must be short compared to the harmonic trap period in order to probe momentum states. We convolve equation 5.2 with a Gaussian function that accounts for our energy resolution before fitting to the data.

To describe quasiparticles, we use

$$I_{\text{coherent}}(k, E) = 4\pi k^2 \cdot \delta(E - \frac{k^2}{m^*} - E_0) \frac{\left[-(\pi m^* T)^{3/2} \text{Li}_{3/2}\left(-\exp\left(\frac{-E_0 + \mu}{T} \right) \right) \right]^{-1}}{\exp\left(\frac{E - \mu}{T} \right) + 1} \quad , \tag{5.3}$$

which consists of a quadratic dispersion of sharp quasiparticles multiplied by a normalized Fermi distribution (δ is the Dirac delta function, and Li is the polylogarithm function). We include as fit parameters, a Hartree shift E_0, effective mass m^*, chemical potential μ, and temperature T. Here, energies are given in units of E_F and m^* in units of m. This description of Fermi liquid

quasiparticles is typically only used very near k_F and for T approaching zero, whereas we fit to data for a larger range in k and with temperatures near 0.2 T_F (just above T_C). The latter is necessitated by the unusually large interaction energy compared to E_F, and we note that 0.2 T_F is still sufficiently cold that one can observe a sharp Fermi surface in momentum [43]. Any increase in quasiparticle widths away from k_F will have little effect on the data as long as the quasiparticles have an energy width less than our energy resolution, which should be the case for long-lived quasiparticles. Finally, as discussed in figure 5.7, using a quadratic dispersion over a large range of k is supported by the data.
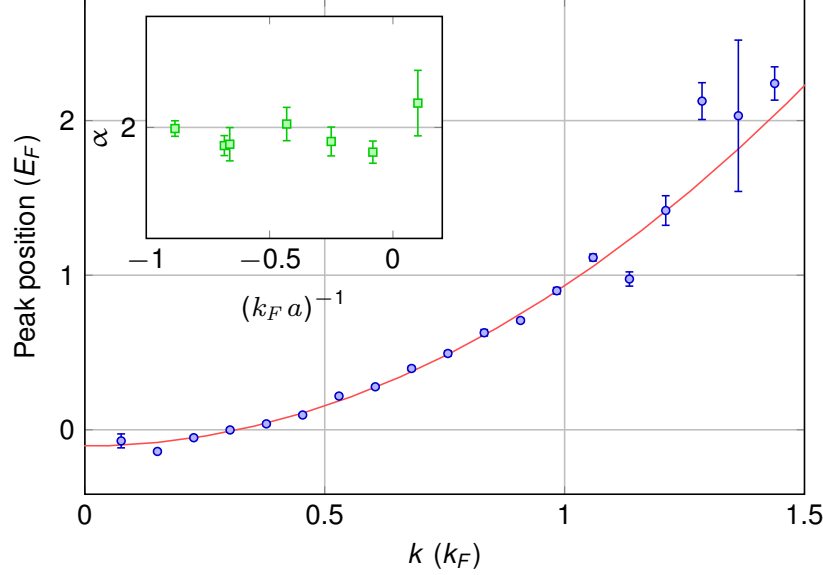
Figure 5.7: **Observation of quadratic dispersion.** An example for the peak dispersion, which is determined by finding the peak location for each k, is shown for $(k_F a)^{-1} = -0.43$ (circles). We locate the peaks by fitting each EDC separately to a Gaussian plus an offset, where the Gaussian width is fixed to the experimental resolution. The red line shows a fit to $Ak^\alpha + B$ in the range $0.2 < k < 1.5$. **Inset,** The exponent from fits to the peak dispersion (squares). The error bars indicate ± 1 standard deviation. We find that α is consistent with 2.

In equation 5.3, we assume a quadratic dispersion for the quasiparticle peak, which agrees well with the data but is only predicted to be valid for $k \approx k_F$. To empirically test the validity of this assumption, we locate the peak positions in the EDCs at each k and fit the dispersion $E(k)$. To focus on a quasiparticle-like peak, and to reduce the effect of the asymmetric tails, we use a

Gaussian fit where the width is constrained to be equal to our resolution ($h \times 2400$ Hz) and where we also include a constant offset as a fit parameter. An example of the resulting peak dispersion for $(k_F a)^{-1} = -0.43$ is shown in figure 5.7. We can then fit the peak dispersion to $Ak^\alpha + B$ to extract an exponent. The results are shown in the inset of figure 5.7 as a function of $(k_F a)^{-1}$, where we restrict this analysis to the region where $Z > 0$. (For higher $(k_F a)^{-1}$, the EDCs are increasingly asymmetric and the peak positions from the Gaussian fits are noisy.) We find that α is consistent with 2, which matches the quadratic dispersion of Fermi liquid theory.

5.3.2 The "incoherent background"

The second part in equation 5.2 needs to accommodate the remainder of the signal, which is often referred to as an "incoherent background" in a Fermi liquid description. However, to the best of our knowledge the functional form of this background has not been determined. In Fermi liquid theory, the fractional signal in the quasiparticle feature decreases as stronger interactions cause greater distortion of the Fermi surface, so it is logical that the growth of the background is directly connected to the "breakdown" of a Fermi liquid picture.

For fermions with contact interactions, one expects signal at high momentum due to short-range pair correlations [2, 55, 90]. In addition, the normal state in the BEC limit of the crossover is a gas of bosonic dimers. Motivated by these two ideas, we use for $I_{\text{incoherent}}$ a function that describes a thermal gas of pairs. The pairs have a wave function that decays as $\exp\left(-r/R\right)$, where r is the relative distance and R is the pair size [91], and a Gaussian distribution of center-of-mass kinetic energies characterized by an effective temperature T_p. This gives

$$I_{\text{incoherent}}(k, E) = \Theta\left(-E_p - E + k^2\right) \frac{8k\sqrt{\frac{E_p}{T_p}} \exp\left(\frac{E_p + E - 3k^2}{T_p}\right) \sinh\left(\frac{2\sqrt{2}k\sqrt{-E_p - E + k^2}}{T_p}\right)}{\pi^{3/2}\left(E - k^2\right)^2} \quad, \quad (5.4)$$

where Θ is the Heaviside step function, E_p is a pairing energy defined by $k_F R = \sqrt{2/E_p}$, and both E_p and T_p are dimensionless fitting parameters. The full derivation of this formula is given in Appendix D. While this description of the incoherent piece may not fully capture the microscopic behavior except in the BEC limit, we find nonetheless that equations 5.2, 5.3, and 5.4 fit the data

very well throughout the crossover, after convolution with a Gaussian function that accounts for our energy resolution. For each value of $(k_F a)^{-1}$, we perform a surface fit to the roughly 300 points that comprise the PES data $I(k, E)$ for $k \leq 1.5$ and $E \geq -3$. The reduced chi-squared statistic, χ^2, after accounting for the seven fit parameters, is between 0.75 and 1.3 (see figure 5.8b.). An example fit is shown in figure 5.8a, where I show several traces at fixed k for PES data taken near unitarity.
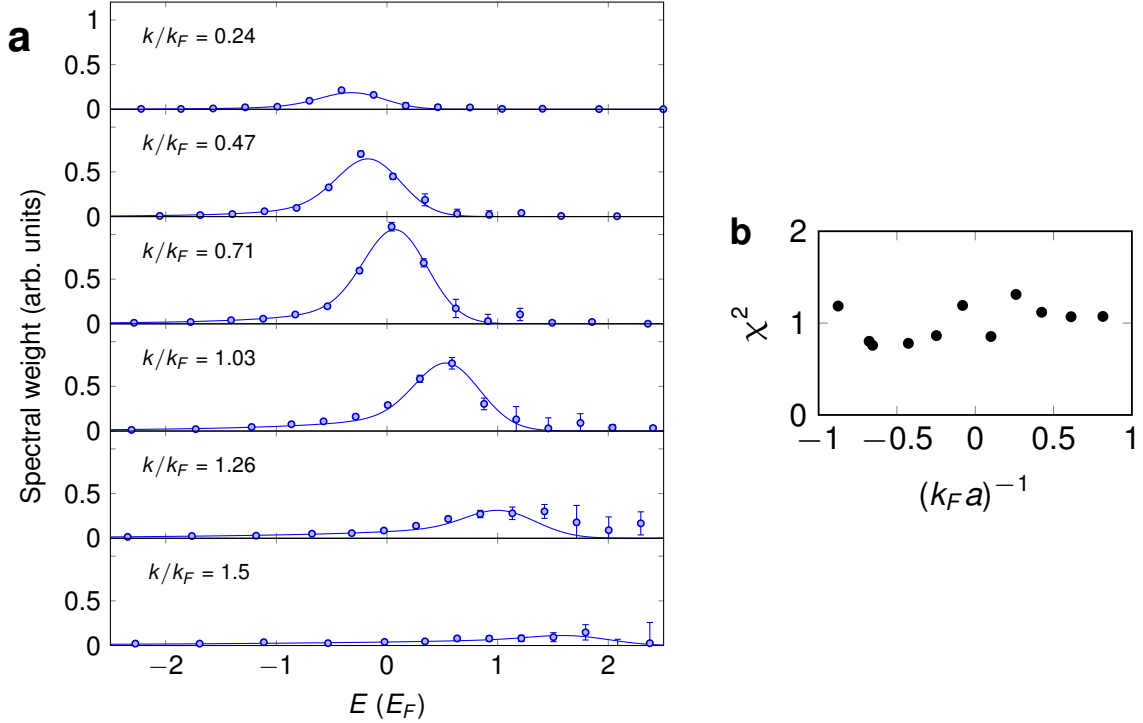
Figure 5.8: **Two-component fits to the atom PES data. a** Data (circles) and fits (lines) are shown for several example traces at fixed k through the PES data at $(k_F a)^{-1} = -0.08$. These traces are often called energy distribution curves, or EDCs. Here, the fitting parameters are $Z = 0.37 \pm 0.03$, $m^* = 1.22 \pm 0.03$, $T = 0.24 \pm 0.02$, $E_0 = -0.33 \pm 0.02$, $\mu = 0.19 \pm 0.04$, $E_p = 0.23 \pm 0.04$, $T_p = 1.09 \pm 0.08$, where the error margins are for one standard deviation and also include a 5% uncertainty in E_F. **b** The χ^2 values from fitting our PES data to our two-component function range from 0.75 to 1.3. For the EDCs shown on the right, the reduced χ^2 is 1.2.

5.4   Results of the fits

In figure 5.10, we show Z as a function of $(k_F a)^{-1}$. For our lowest $(k_F a)^{-1}$, $Z \approx 0.8$; however, Z decreases rapidly going from the BCS side of the crossover (negative a) to the BEC side

Figure 5.9: **Comparing the PES data with the results of the two-component fits.** The top row shows seven of the PES dispersion plots from figure 5.6. The bottom row shows dispersion plots constructed from equations 5.2, 5.3, and 5.4 and the best fit parameters corresponding to the data above. The fitted value of Z is shown between e

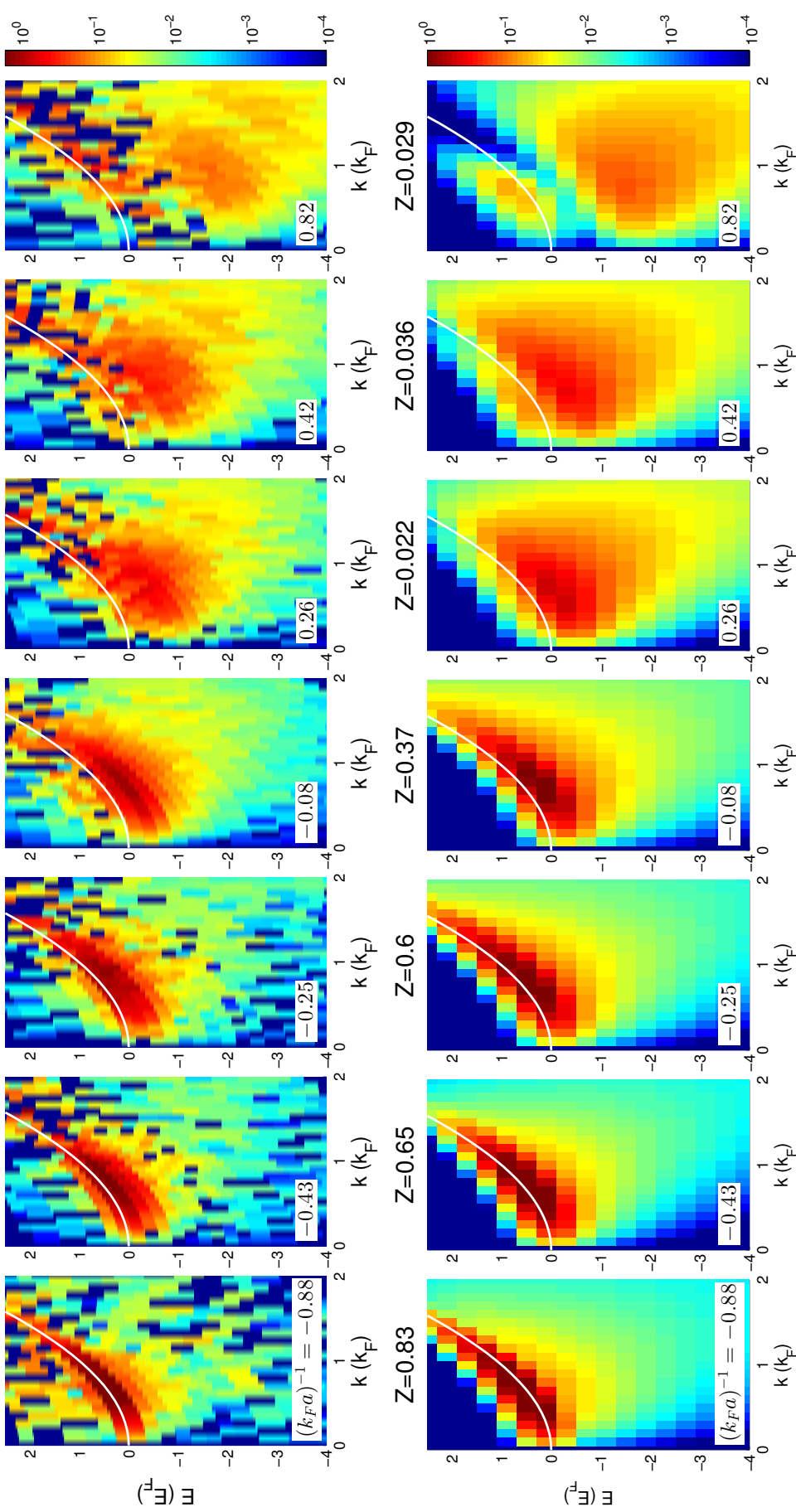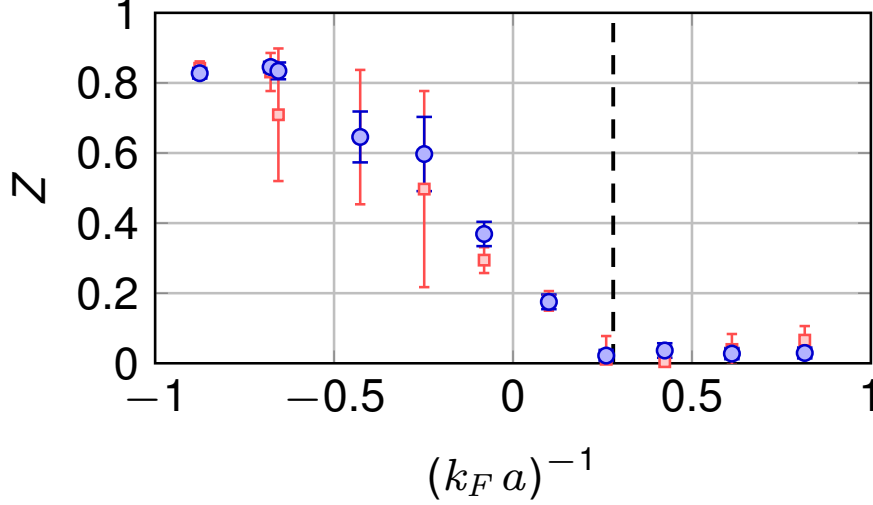Figure 5.10: Z, **the quasiparticle spectral weight** The quasiparticle spectral weight decreases as $(k_F a)^{-1}$ increases. Using a linear fit to the range $-0.5 \leq (k_F a)^{-1} \leq 0.3$, we find that Z vanishes at $(k_F a)^{-1} = 0.28 \pm 0.02$ (dashed line); this marks the breakdown of a Fermi liquid description. The blue circles come from fits of a large range of data, from 0 to 1.5 k_F. The red squares show the result of restricting the fit to 0.7 to 1.3 k_F, and they show a similar trend and slightly larger error bars.

(positive a), reaching $Z \approx 0.3$ at unitarity. Beyond $(k_F a)^{-1} = 0.28 \pm 0.02$, Z vanishes, signaling the breakdown of a Fermi liquid description. Restricting the fitting to a smaller region around k_F gives results for Z that are consistent with the fits to $k \leq 1.5$ (red points in figure 5.10). We note that the interaction strength where Z vanishes, as well as the sharpness with which Z goes to zero, are likely to be temperature dependent [92].

The best fit values for the effective mass, m^* are shown in figure 5.11, where m^* increases with increasing interaction strength as expected for a Fermi liquid. A linear fit gives $m^* = 1.21 \pm 0.03$ at unitarity, which is somewhat higher than $m^* = 1.13 \pm 0.03$ measured in Ref. [35], but close to the $T = 0$ prediction of $m^* = 1.19$ from Ref. [86].

The fitted values of the remaining parameters are shown in figure 5.12. The temperatures characterizing the two parts of equation 5.2 T and T_p are shown in figure 5.12**a**. For the quasiparticle component, T is close to, but somewhat above the estimated temperature of the gas, $T = (0.18 \pm 0.02)T_F$. We attribute the discrepancy to the remaining density inhomogeneity of the probed
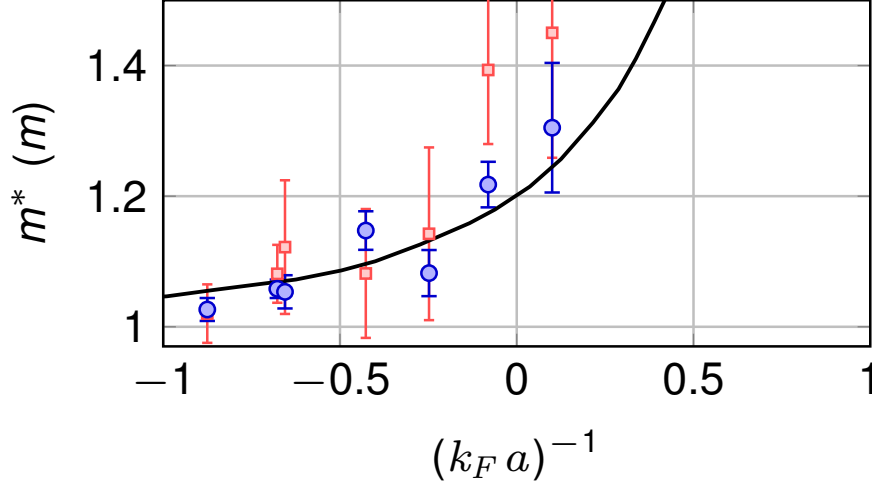
Figure 5.11: m^*, **the quasiparticle effective mass.** The quasiparticle effective mass m^* is shown for the region where $Z > 0$. Interactions increase m^*, and the data (circles) agree surprisingly well with the theoretical prediction for the limiting case of the Fermi polaron (solid line) [93, 4]. Restricting the fit to EDCs close to the Fermi surface produces similar results with increased error bars (red squares).

portion of the trapped gas, which can broaden sharp features. In particular, when applying our PES measurement technique to a weakly interacting gas, we find that the resulting momentum distribution has a step at the Fermi surface whose width typically corresponds to $T \approx 0.25 T_F$. For the incoherent component, T_p, which in the model characterizes the spread of center-of-mass energies of pairs, is around $0.75 T_F$. This is much higher than the temperature of the gas and suggests that the data cannot be simply interpreted as coming from weakly bound bosonic molecules in thermal equilibrium with a Fermi gas of atoms.

Figure 5.12**b** shows the second fit parameter in $I_{\text{incoherent}}$, which is a binding energy $E_p = \frac{\hbar^2}{mR^2}$ that sets the size of the pairs R. For the data farthest on the BEC side of the crossover, E_p approaches the two-body molecule binding energy, $\frac{\hbar^2}{ma^2}$ (solid line in figure 5.12**b**). In the crossover, E_p is larger than the binding energy for two-body molecules, as one would expect for many-body pairs.

The two remaining fit parameters, E_0 and μ, come from the quasiparticle part of the fitting function and are shown in figure 5.12**c** and **d**, respectively. The Hartree energy shift E_0 is negative

and has a magnitude that increases as $(k_F a)^{-1}$ increases, reaching a value of $-0.46 \pm 0.03 E_F$ at unitarity, in good agreement with several theoretical calculations [94, 86, 95, 96]. Figure 5.12**c** shows E_0 for the full range of $(k_F a)^{-1}$ for our data. Here, one can clearly see the jump in the fit values and the large uncertainties that appear in the region where the fits return a small Z. This happens because the quasiparticle component that is fit for $(k_F a)^{-1} < 0.2$ has vanished. For this reason, when discussing the fit parameters for the quasiparticle part (m^*, T, E_0, and μ), we focus on the region $(k_F a)^{-1} < 0.2$.

The chemical potential, μ, from the quasiparticle part of the fit is shown in figure 5.12**d**. In general, one expects μ to decrease as $(k_F a)^{-1}$ increases. The data (blue circles) for $(k_F a)^{-1} > -0.5$ follow this expected trend, but the points for our two lowest $(k_F a)^{-1}$ values are surprisingly low. In addition, all the values of μ here are somewhat lower than the predicted chemical potential in the BCS-BEC crossover [77]. We have found that there is some interdependence of the two fit parameters μ and T for the quasiparticles. This is illustrated in figure 5.12**d**, where the red squares show the result for μ when we fix $T = 0.25$ in the fits. (The effect of fixing T on the other fit parameters is to reduce some scatter but is otherwise minimal.) This interdependence, and the fact that T is increased by technical issues (namely, the remaining density inhomogeneity that limits our resolution in k), may play a role in explaining the lower than expected values for μ.

5.4.1 Comparison to the Fermi polaron case

It is interesting to compare our results with those of Fermi polaron, which is the quasiparticle in the limit of a highly imbalanced Fermi gas. Schirotzek *et al.* measured $Z = 0.39 \pm 0.09$ for the Fermi polaron at unitarity [97], which is similar to our result for the balanced Fermi gas. For the polaron case, Z also goes to zero in a similar fashion to our results, but farther on the BEC side of the crossover [97]. This similarity is surprising because we expect a phase transition from polarons to molecules in the extreme imbalance limit [98, 99], with Z acting as an order parameter [100], while, in contrast, the balanced Fermi gas should exhibit a continuous crossover. For m^*, we also find that our result is close to the measured effective mass of the Fermi polaron at unitarity [35],
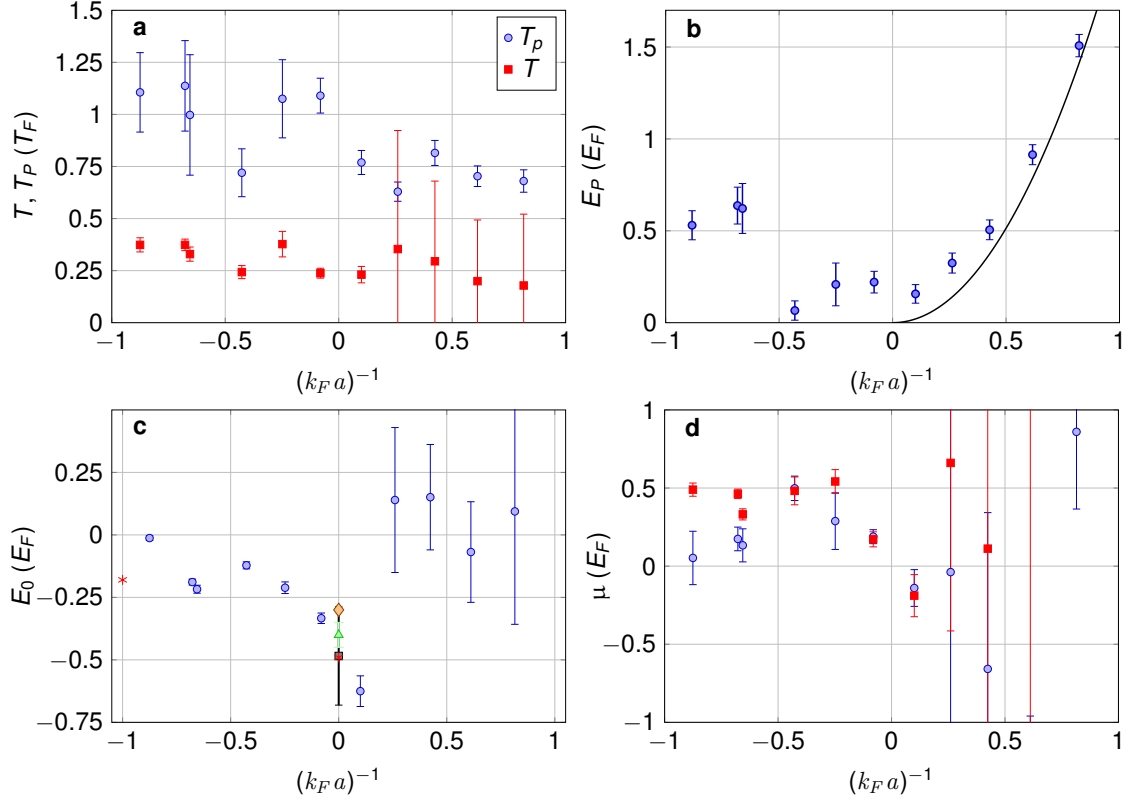
Figure 5.12: **Parameters of the fits to the PES data. a**, We extract two temperatures from our fits to $I(k, E)$. The quasiparticle parts of the fits to the PES data give T values (red squares) that are comparable to, but higher than, our estimated temperature of the gas at unitarity ($T = 0.18 \pm 0.02$). In contrast, the incoherent parts of the fit give T_p values (blue circles) around 0.75. T_p can be thought of as an effective temperature that characterizes the energy width of the incoherent part of the spectral function. **b**, The pairing energy, E_p, comes from the incoherent part of the fit. At the largest $(k_F a)^{-1}$, the data (circles) approach the two-body molecular binding energy (line). **c**, The Hartree energy shift, $\mathbf{E_0}$, comes from the quasiparticle part (blue circles). The error bars correspond to ± 1 standard deviation from the fits and 5% uncertainty in E_F. Also shown are the results of a quantum Monte-Carlo calculation [94] (black square) and three theories by Haussmann *et al.* [86] (red asterisks), Kinnunen [95] (green triangle), and Bruun and Baym [96] (orange diamond). **d**, The chemical potential μ is also found in the quasiparticle part of the fit. We show the results of the fit with (red squares) and without (blue circles) the constraint $T = 0.25$. The fact that constraining T affects the best fit value for μ reveals an interdependence of μ and T that we do not observe for the other fit parameters.

$m^* = 1.20 \pm 0.02$, and similar to the predicted polaron mass [93, 4] throughout our measurement range (solid line in figure 5.11).
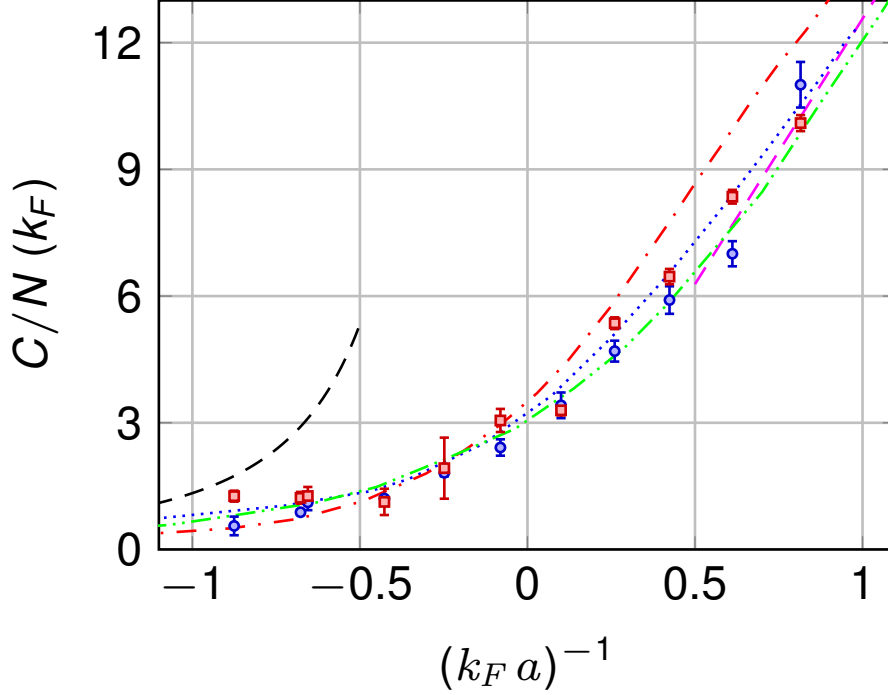
Figure 5.13: **The contact parameter.** From the PES data, we extract the contact per particle (in units of k_F) for a homogeneous Fermi gas above T_C as a function of the interaction strength $(k_F a)^{-1}$. The contact measured from the tail of the rf line shape, using data for $h\nu \geq 5E_F$, is shown in blue circles, while the contact extrapolated from the fits of the PES data is shown in red squares. Remarkably, even though we limited the fits of the PES data to $k \leq 1.5$ and $E \geq -3$, a region with a relatively small contribution of short-range correlations [2, 55, 3, 49], we find that the contact from the PES fits is consistent with the contact measured from the tail of the momentum-integrated rf line shape. For comparison with the data, we also plot the BCS (dashed black line) and BEC (dashed magenta line) limits, given by $4(k_F a)^2/3$ and $4\pi(k_F a)^{-1}$, respectively [55], the non-self-consistent t-matrix at $T = 0$ (dotted blue line) and its Popov version at T_C (dash-dotted red line) [65], and the self-consistent t-matrix model at $T = 0$ (double-dotted green line) [86]. Interestingly, we find that the contact measured above T_C agrees well with the $T = 0$ theories.

5.5 The homogeneous contact vs. $(k_F a)^{-1}$

In chapter 4, we measured the contact of a homogeneous gas at unitarity as a function of temperature. In this chapter, we also measure the rf line shape, and we can extract the contact as a function of $(k_F a)^{-1}$ from these measurements. As $(k_F a)^{-1}$ increases, short-range correlations are expected to increase, and so is the contact. Figure 5.13 shows the measured contact per particle, C/N, in units of k_F, as a function of $(k_F a)^{-1}$. The blue points come from the weight in the rf line shape tail.

We can also extract the contact in another, perhaps surprising, way. In a Fermi liquid description of strongly interacting atoms, the contact is expected to be valid and finite, and it must be accounted for by the incoherent part of the spectral function [90]. (The contact cannot be accounted for by the quasiparticle part, which only includes narrow peaks that are symmetric in energy.) Our particular choice for $I_{\text{incoherent}}$ has the expected form of a $1/k^4$ high-k tail in the momentum distribution [2] and a $1/\nu^{3/2}$ large-ν tail in the rf line shape [55], where ν is the rf detuning (see equations 4.1 and 4.9 from chapter 4). Thus, we can extract the contact directly from the fits the to PES data (figure 5.13, red points). To do this, we use the model and the best fit parameters for each data set, to calculate the momentum distribution: $n(k) = \int_{-\infty}^{\infty} I_p(k, E)\mathrm{d}E$ out to $k = 5$. We then find the contact from the average value of $k^4 n(k)$ in the region $3 \leq k \leq 5$. Remarkably, we find that the contact can be accurately extracted in this way even though we restrict the fits to $k \leq 1.5$. For comparison, $1/k^4$ behavior in the momentum distribution was observed for $k > 1.5 k_F$ [3], and the fits to the rf line shape tails are restricted to $h\nu \geq 5E_F$.

As a check of the fitting function, we have compared these results with a simple expression derived from the contact for weakly bound molecules. For a dimer with a wave function $\phi(r) = \sqrt{\frac{2}{R}}e^{-r/R}$, the contact [101] is $C_{\text{dimer}} = 8\pi/R$. Since the dimer consists of two atoms, the contact per particle is $C/N = 4\pi/R$. Expressing this in terms of the dimensionless E_p and multiplying by the amplitude $(1 - Z)$, we have

$$\frac{C}{Nk_F} = 4\pi(1 - Z)\sqrt{\frac{E_p}{2}} \quad . \tag{5.5}$$

We find that the result of equation (5.5) agrees very well with the contact extracted directly from the momentum tail of the fitted dispersion.

5.6   Understanding the "incoherent background"

The two-part function that we use to fit and analyzed our PES data is simply the sum of the expected forms of the spectral function in the BCS and BEC limits. One can argue that the "quasiparticle" part has a generic form that should describe Fermi liquid-like quasiparticles

regardless of how strong the interactions, provided that the lifetimes of those quasiparticles give energy widths which are far below the energy resolution of our spectroscopy. However, the other part of the fitting function describes tightly bound ^{40}K$_2$ molecules with a specific binding energy, E_p, and a thermal distribution described by Boltzmann statistics. This is a good description for a gas of molecules far from resonance on the BEC side of the crossover. In the center of the crossover, where any pairs are of the similar size to the interparticle spacing and Fermi statistics presumably still play a role in pairing, it is unclear whether the choice of this function to describe the non-quasiparticle signal is justified.

In this section, I attempt to lay out an intuitive understanding of the non-quasiparticle signal and our choice of functional form for $I_{\text{incoherent}}$. I also present some arguments justifying our choice as not only a good fit to our data, but a reasonable physical description.

5.6.1 $I_{\text{incoherent}}$ as large pairs in the crossover

One interpretation of $I_{\text{incoherent}}$ is that it describes many-body pairing in the crossover. The functional form correctly describes molecules in the BEC limit, and one can think of those molecules remaining but getting more weakly bound as interactions are decreased. Weakly bound pairs with a very large size are expected for many-body pairing in the superfluid phase in the center of the BCS-BEC crossover, and this is also a way to describe pairing in the normal phase in a pseudogap picture.

To understand $I_{\text{incoherent}}$ as describing many-body pairs, we can look at the fit parameter E_p as giving a characteristic pair size. As seen in figures 5.12 and 5.14a, fitted E_p values from the data sets taken farthest on the BEC side are consistent with the prediction of dimers with binding energy determined by the scattering length, $E_p = \frac{\hbar}{ma^2}$. As the interaction strength decreases, the fitted pairing energy drops to less than half E_F, indicating a pair size that is more than twice the interparticle spacing. The pair size, R, given by $E_p = \frac{\hbar}{mR^2}$, is shown in figure 5.14b.

The divergence of the fit values for R from the two-body prediction could be thought of as the gradual change from two-body dimers to main-body pairs. Certainly, pairs that are a few
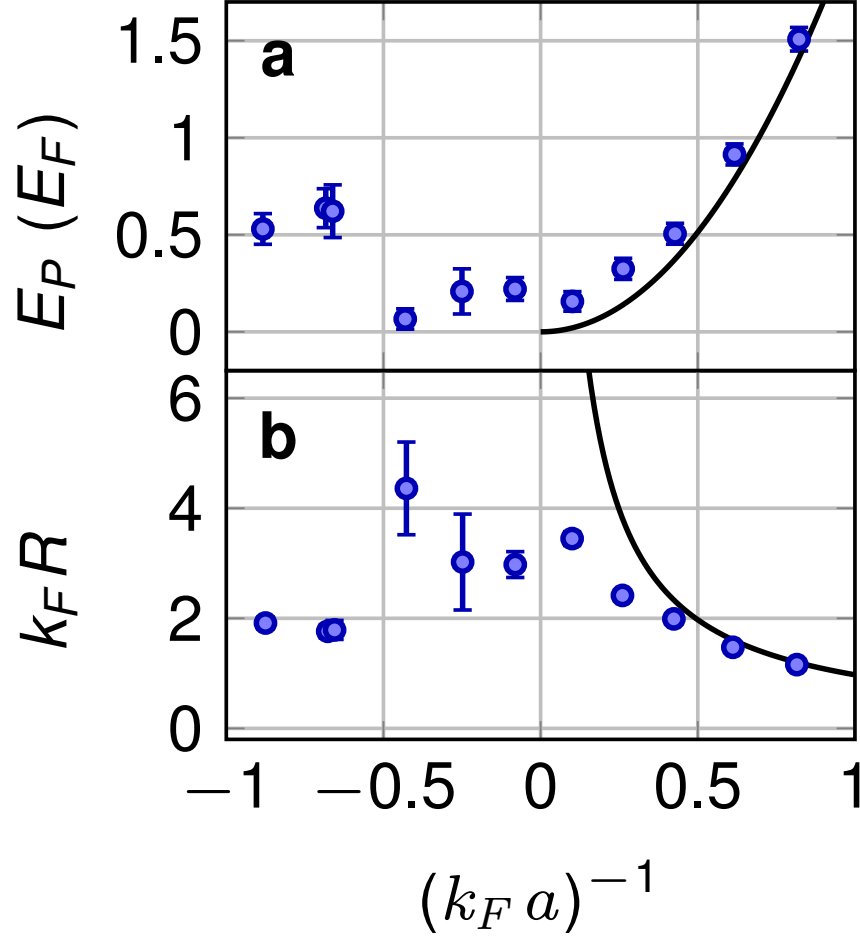
Figure 5.14: **Fit results for binding energy and pair size from** $I_{\text{incoherent}}$**. a**, Fitting to our two-part function yields results for E_p that are consistent with the two-body prediction in the BEC limit and deviate from this prediction around unitarity. This is the same plot as presented in figure 5.12b. **b**, E_p is directly related to a characteristic pair size through $E_p = \frac{\hbar}{ma^2}$. In the case of only two atoms, the pair size is predicted to be equal to the scattering length, a. At unitarity, this prediction diverges and is therefore unphysical. The fit returns pair sizes in the crossover which are larger than the interparticle spacing, k_F^{-1}.

times larger than the average interparticle spacing, k_F^{-1}, can no longer be thought of as "traditional" molecules. Molecules that are much smaller than k_F^{-1} are predicted to exist outside of the crossover, for $(k_F a)^{-1} > 1$. Seeing these small molecules would require data taken farther on the BEC side.

Evidence of a pseudogap and the associated many-body pairing encompasses more than seeing large pairs. In addition, these pairs must form around the Fermi surface, causing a back-bending in the dispersion near k_F [73]. In Appendix C, it is shown that both our data and the two-part fitting

function produce the qualitative back-bending effect. However, it is unclear how to quantify this back-bending from our fit parameters. Additionally, the hallmark of a pseudo-gap is a suppression in the density of states, which is almost, but not quite, an energy gap between occupied and unoccupied bands. Unfortunately, atom PES only measures the occupied spectral function, and so we cannot see the pseudogap directly.

5.6.2 $I_{\text{incoherent}}$ as part of a Fermi liquid

Descriptions of a Fermi liquid typically focus on the presence of coherent, long-lived quasi-particles. However, a Fermi liquid as first presented by Landau has another part—an incoherent background signal with large energy widths that contrasts with the peaked dispersion of the quasi-particles [80].

For interaction strengths less than $(k_F a)^{-1} = 0.28$, the PES data show some component that is (relatively) narrow in energy and positively dispersing, which is well described by I_{coherent}, our function based on quasiparticles. If the gas has some quasiparticles (the presence of which are consistent with, if not completely proven by, our results), it can be thought of as a Fermi liquid, with the non-quasiparticle signal being the broad, incoherent background described by Landau. The form of this background signal is not specified, but we know that its growth is linked to the shrinking of the quasiparticle residue and the eventual breakdown of the Fermi liquid. In the BCS-BEC crossover, this motivates a background piece, $I_{\text{incoherent}}$, that describes uncondensed pairs.

5.6.3 $I_{\text{incoherent}}$ and the Contact

Theoretical work done by Schneider and Randeria calculated the spectral function for a Fermi liquid of atoms and showed that the "background" signal has a high momentum, negative energy component [90]. This component has a $1/k^4$ dependence on momentum and is related to Tan's contact. We see that our form of $I_{\text{incoherent}}$ has spectral weight in this high momentum, low energy region and, moreover, has the same form predicted by Randeria.

Our choice for $I_{\text{incoherent}}$, moreover, as briefly discussed in section 5.5, not only has the

correct *form* of the tails of the momentum distribution and rf line shape for a gas with a contact (see equations 4.1 and 4.9), but our own best fit parameters when fitting a restricted region of PES data near k_F nevertheless give the correct *value* for the contact (when compared to the high frequency tails in rf spectroscopy).

5.7 Conclusions

The results presented in this chapter show that PES data are consistent with a spectral function that includes two parts, namely a coherent part that corresponds to long-lived fermionic quasiparticles and an incoherent part that describes large, many-body pairs. These results explain how different observations lead to different conclusions regarding the nature of the normal state of the unitary Fermi gas. Although the data here taken just above T_C show that a Fermi liquid description breaks down for $(k_F a)^{-1} \geq 0.28 \pm 0.02$, Z remains finite at unitary. Fermionic quasiparticles may play a key role in thermodynamics, while PES data reveal back-bending and significant spectral weight in an "incoherent" part that is consistent with pairing. With the nearly homogeneous PES data, we find that Z vanishes surprisingly abruptly and note some similarity to Fermi polaron measurements. Comparing the PES data with various BCS-BEC crossover theories may help elucidate these observations and advance quantitative understanding of the crossover.

Chapter 6

Photoemission spectroscopy as a function of temperature

In chapter 5, I presented our results regarding the evolution of the spectral function in the normal phase of the BCS-BEC crossover. In addition to these studies, we wanted to see how the spectral function of a homogeneous gas changes with temperature. This chapter presents our preliminary findings.

We took PES data for several temperatures at two interaction strengths, one on either side of the Feshbach resonance. This data was taken using the sequence and procedures laid out in chapter 5. The data on the BCS side was taken for $(k_F a)^{-1} = -0.24(2)$, and the data on the BEC side was at $(k_F a)^{-1} = 0.23(3)$. (The error reflects the small variations in $(k_F a)^{-1}$ in the data sets.)

6.1   Temperature in the normal phase of atoms in the BCS-BEC crossover

Looking back to the phase diagram of atoms in the BCS-BEC crossover (figure 1.2), one can see that the presence of preformed pairs is expected for some interactions and temperatures above T_C, but not for all. There is another temperature, T_{pair} (often called T^* [24, 27]), which signifies a crossover from a region of the phase diagram with pairs to a region without pairs. Consistent with the gradual increase of pair-like signal as a function of $(k_F a)^{-1}$ in the PES data in chapter 5, T_{pair} does not mark a phase transition but instead corresponds to a gradual transition over some range of interaction strengths and temperatures. We expect that the fraction of pair-like signal in PES data should depend on the temperature of the gas, as well as on the interaction strength.

A Fermi liquid is also expected to change its character as a function of temperature. The

Fermi liquid is a description of gas of interacting fermions at a temperature much lower than the Fermi temperature. At these temperatures, the deBroglie wavelength of the particles is comparable to the interparticle spacing; this is the regime of a "quantum" liquid [80]. At higher temperatures, the gas moves out of the quantum regime, and the properties that depend on the quantum nature of the system go away. At this point, we would expect the effective mass of the Fermi liquid to approach the bare mass and the dispersion to be close to that of an ideal (non-interacting) Fermi gas. At finite temperature in the quantum regime, Fermi liquid behavior may persist, but the quasiparticle lifetime may decrease. In the PES data, a shorter quasiparticle lifetime should appear as an increased energy width in the dispersion.

Investigating the dependence of PES signal on temperature is as interesting and challenging an endeavor as investigating the dependence on interaction strength at $T \approx T_C$. One particular challenge is the possible increase of the energy widths of the quasiparticle feature with temperature. In the $T \approx T_C$ data, we isolated the quasiparticle signal from the background by looking for resolution-limited features (chapter 5). If the width of the "sharp" quasiparticle feature were to increase to the size of our resolution or above, this approach would no longer work. In order to see this very interesting behavior, we would need to develop better resolution in our experiment or a different analysis technique. In the first part of this chapter, I analyze PES data vs. temperature by extracting the contact from the rf line shape, as was done in chapter 4. This analysis is more straightforward, as it is not affected by the energy widths in the data, and it produces the first measurement of the homogenous contact as a function of temperature at interaction strengths other than unitarity. In the second part of this chapter, I analyze the PES signal using our two-part fitting function, and I show how this yields some nice results, as well as some evidence that another way to analyze this data is needed.

6.2   The contact

As in chapters 4 and 5, the contact of a homogeneous gas can be extracted by fitting the high frequency tails of the rf line shapes (see equation 4.13). Figure 6.1 shows the results for our data
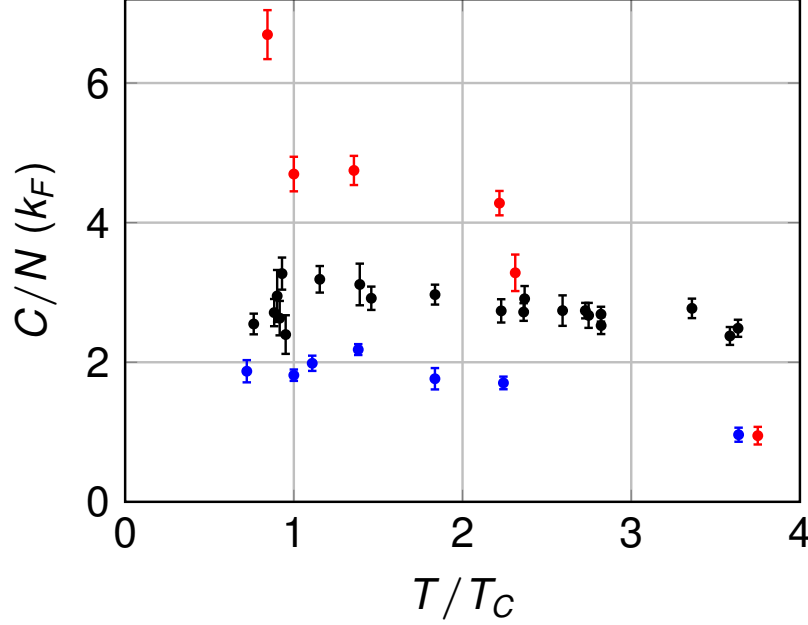
Figure 6.1: **The contact of a homogeneous gas at three interaction strengths.** The red points were taken at $(k_F a)^{-1} = 0.23(3)$, the black points at $(k_F a)^{-1} = 0$ (from figure 4.8), and the blue at $(k_F a)^{-1} = -0.24(2)$.
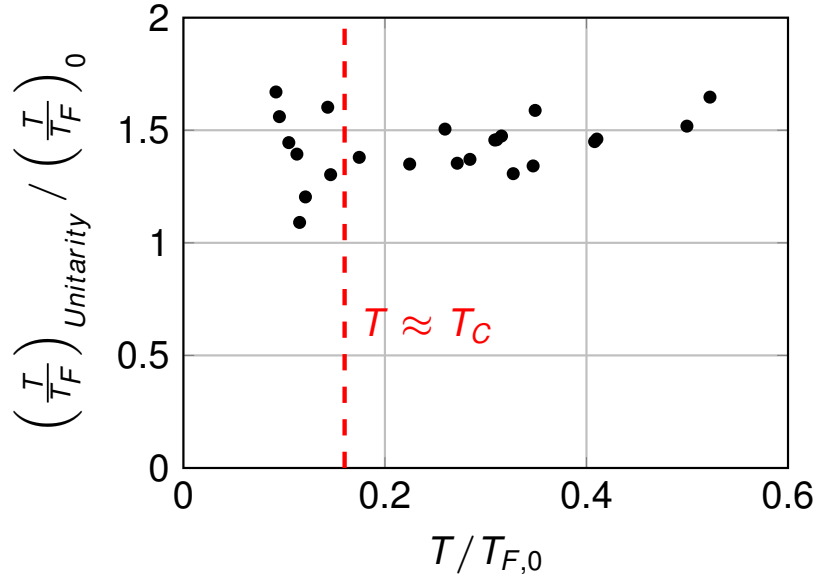
Figure 6.2: **Comparing initial temperature of the weakly interacting gas with the temperature at unitarity.** We measure $T/T_{F,0}$ of the gas at $a \approx 1100 a_0$, after finishing evaporation and before a 50 ms ramp to unitarity. $T/T_{F,Unitarity}$ of the gas after this ramp is measured using the release energy of the gas, as presented in Appendix A. The ratio of $T/T_{F,Unitarity}$ to $T/T_{F,0}$ is roughly constant (1.4 ± 0.2) for $T > T_C$. We expected this to also be true for data taken at $(k_F a)^{-1} = 0.23(3)$ and $-0.24(2)$.

exploring temperature dependence at the different values of $(k_F a)^{-1}$ in the strongly interacting regime.

As expected, the contact increases as the interaction strength, $(k_F a)^{-1}$ increases. The x-axis in figure 6.1 is the temperature normalized by T_C, which is the critical temperature for condensation at the field in question. For the data points at unitarity, we were able to determine the temperature of the atoms at the final interaction strength through methods outlined in Appendix A. However, we do not have a reliable way to determine the temperature of the atoms at values of $(k_F a)^{-1}$ other than unitarity. For these data, we experimentally determine T_C in terms of $T_{F,0}$ using the pair projection technique [25]. ($T/T_{F,0}$ is the initial temperature of the gas at $a \approx 1100 a_0$ before the final magnetic field sweep towards the Feshbach resonance, so $T_C/T_{F,0}$ is the initial temperature that, after sweeping to the final interaction strength, yields a gas at the critical temperature.) To estimate T/T_C for the non-unitarity data, we take the ratio of $T/T_{F,0}$ to $T_C/T_{F,0}$, and we make the assumption that the ratio of T/T_F of the gas at the final field to its initial $T/T_{F,0}$ is constant for many temperatures. We find this assumption to be approximately true for the majority of the unitarity data above $T = T_C$ and below $T = 0.6 T_F$ (see figure 6.2). (At unitarity, $T_F \approx 6 T_C$.)

The data show a strong dependence of the contact on temperature for the BEC side, while the data taken at unitarity and on the BCS side have a much weaker dependence. Neither the BEC nor the BCS side data definitively show the non-monotonic behavior seen in the unitarity data at low temperature, but one would need to take more data near and below T_C to investigate this.

6.3   The occupied spectral function as a function of temperature

The PES data on either side of the resonance is shown in figures 6.3 and 6.4. There are a few distinguishing features of this data. First of all, the PES data on the BCS side is narrow with most of the signal contained in a positively dispersing peak. The data on the BEC side is comparatively broader in energy. For both sets, the signal along the positively dispersing feature reaches to higher E/E_F as temperature increases; this is expected as the higher energy broadens the Fermi surface. Also, both sets show the signal shifting closer to the free particle line for higher

temperatures. In fact, the highest temperature sets on either side $([T/T_C, (k_F a)^{-1}] = [3.8, -0.24]$ and $[3.6, 0.23])$ look very similar. This might be understood as the temperature setting the energy scale instead of the interactions.

6.4 Fitting to our two-component function

I fit our new PES data to the two-part function presented in chapter 5, equation 5.2. While this analysis worked well for the data just above T_C, whether it extends to higher temperatures or to data with significant superfluid fractions was uncertain. In particular, while we clearly saw for data near $T = T_C$ that sharp features (i.e. the quasiparticle part) have widths limited by the resolution, it is not clear that this should be the case at higher temperatures as well. According to Landau, the energy width of the quasiparticle peak should scale with the square of the temperature [79, 80], so the higher temperature data might have a larger width. To look for this effect, I fit the data at $(k_F a)^{-1} = -0.24(2)$ to a version of equation 5.2 in which the delta function in I_{coherent} is replaced by a Gaussian function with a width, σ, determined by the fit:

$$I_{\text{coherent}}(k, E) = 4\pi k^2 \cdot \frac{1}{\sqrt{2\pi}\sigma} \exp \frac{-[E - (E_0 + \frac{k^2}{m^*})]^2}{2\sigma^2} \frac{\left[-(\pi m^* T)^{3/2} \, \text{Li}_{3/2} \left(-\exp \left(\frac{-E_0 + \mu}{T} \right) \right) \right]^{-1}}{\exp \left(\frac{E - \mu}{T} \right) + 1},$$

$$(6.1)$$

Figure 6.5 shows the results of fitting the data on the BCS side while allowing the width to float. As before, we apply a Gaussian convolution to account for our experimental energy resolution. For the lowest temperatures, σ is consistent with zero, which means that the width of the quasiparticle peak is limited by our resolution. For the highest temperatures, we see that the best fit includes a finite σ, but the values are comparable to our resolution of 2.4 kHz.

How well the fitting function describes our data is shown by the reduced chi-squared statistic, χ^2, in figure 6.6. For the data presented in chapter 5, χ^2 is between 0.75 and 1.3, indicating a good fit. Fits to the data at $(k_F a)^{-1} = -0.24(2)$ are similarly good, and χ^2 is between 0.7 and 1.4 with no discernible trend versus temperature. Allowing the width to be an additional fitting parameter does not change χ^2 significantly. Fits to the data at $(k_F a)^{-1} = 0.23(3)$ are not as good, and χ^2
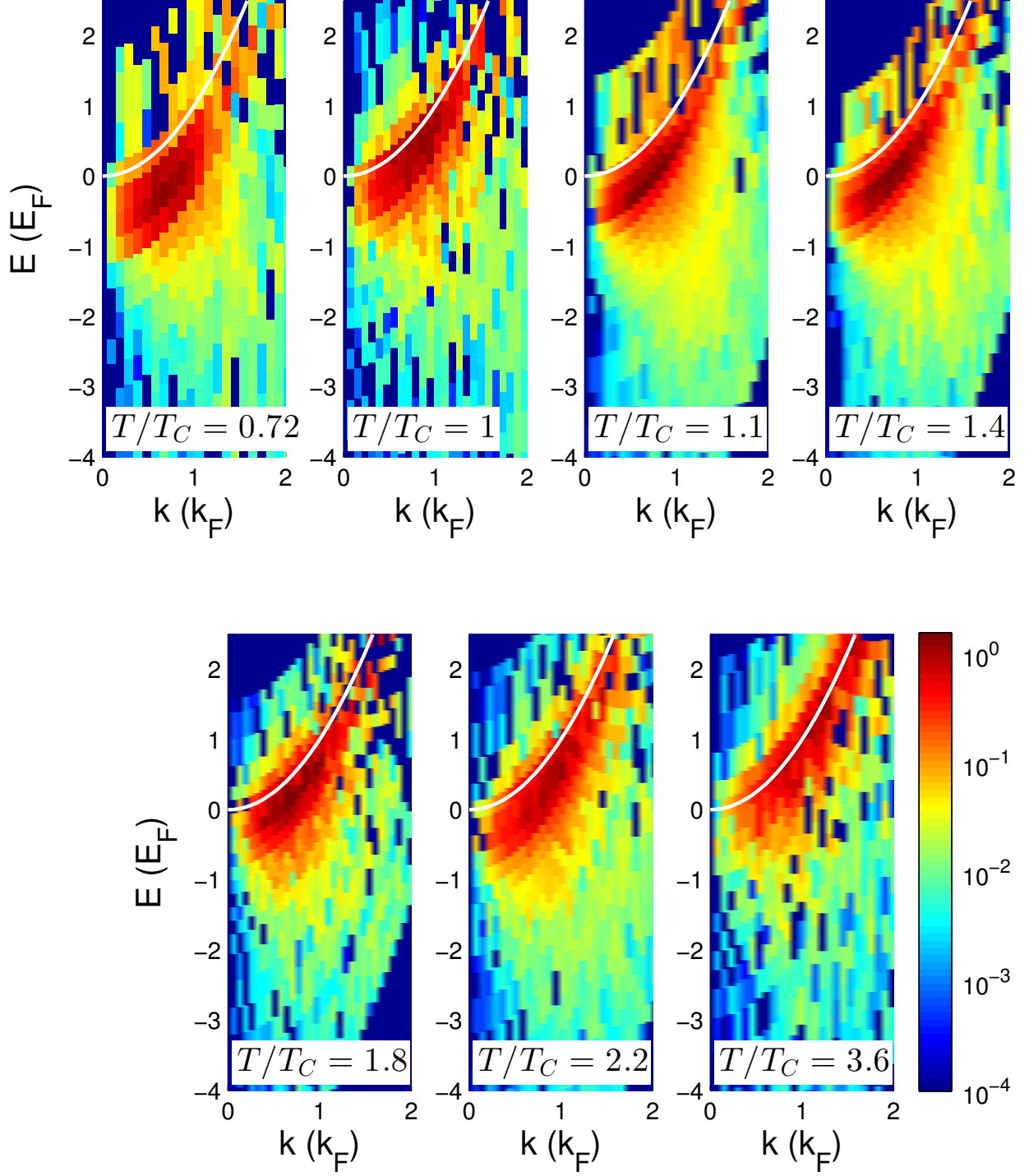
Figure 6.3: **PES data at** $(k_F a)^{-1} = -0.24(2)$**.**

ranges from 1 to 4. It is unclear why this is the case for these data.

These results suggest that an additional width parameter in the fits is not needed to fit our
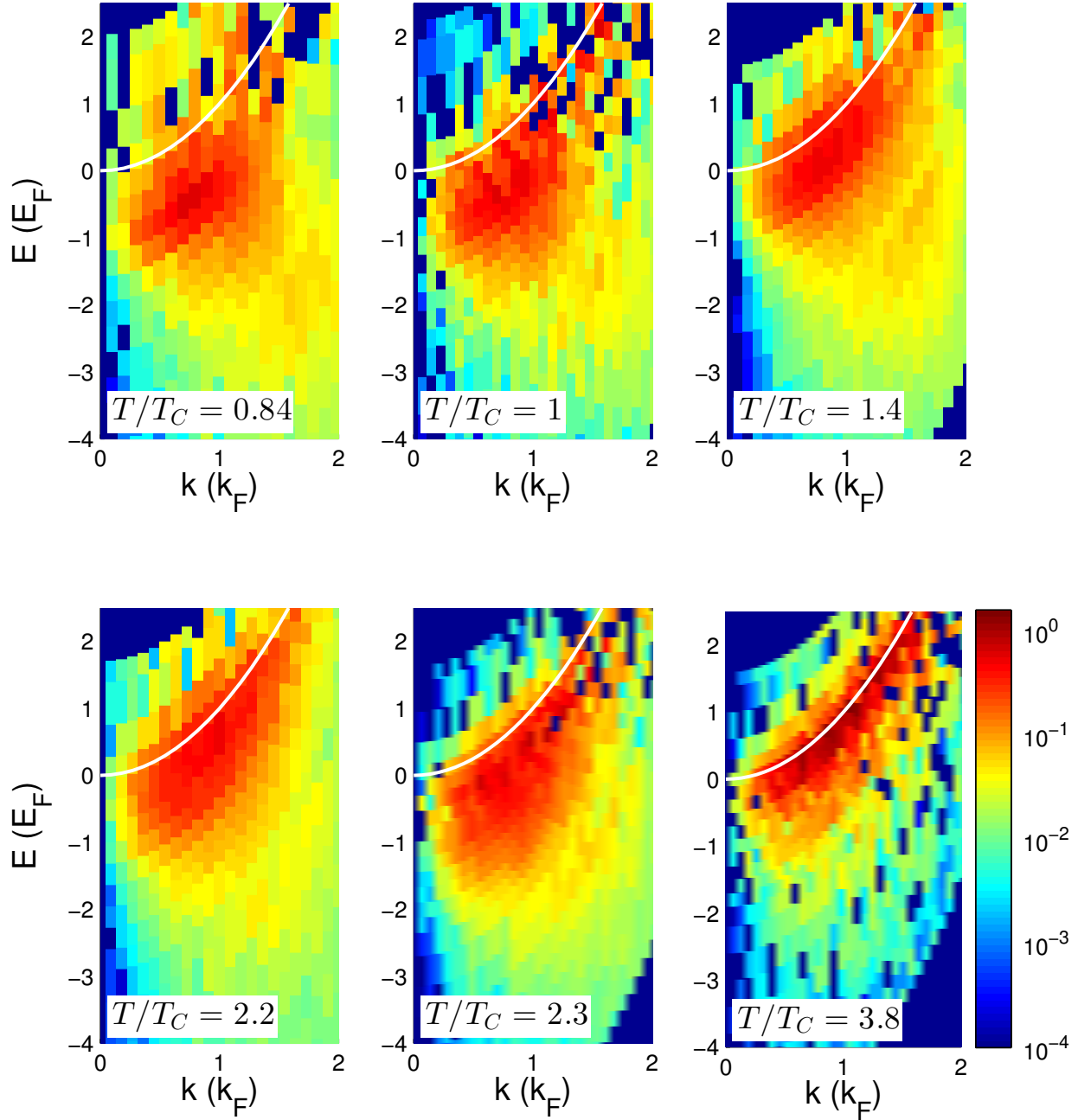
Figure 6.4: **PES data at** $(k_F a)^{-1} = 0.23(3)$.

data. In addition, if the width of I_{coherent} can vary, some of the incoherent background signal could be fit as quasiparticles. We clearly see this effect for the data taken at $(k_F a)^{-1} = 0.23(3)$, where the incoherent background makes up the majority of the signal. For the remainder of this section, I fit the data at $(k_F a)^{-1} = -0.24(2)$ two ways, both including an energy width fit parameter in
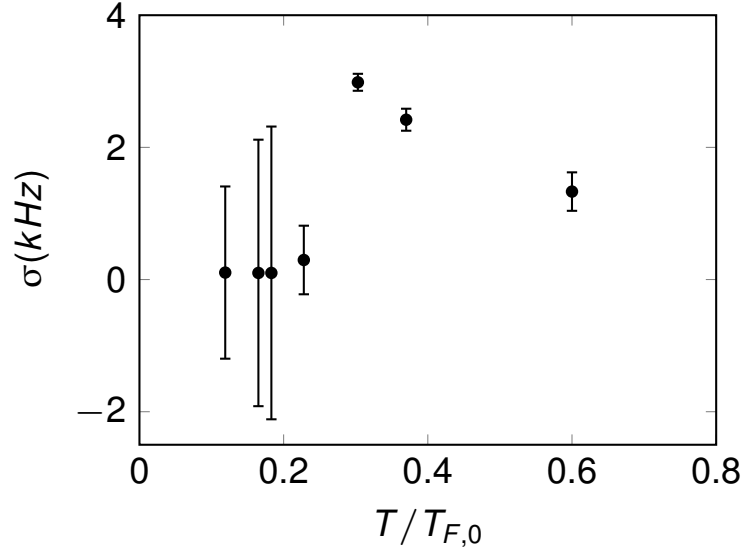
Figure 6.5: **The energy widths in** I_{coherent}. The data sets shown here were taken at $(k_F a)^{-1} = -0.24(2)$.
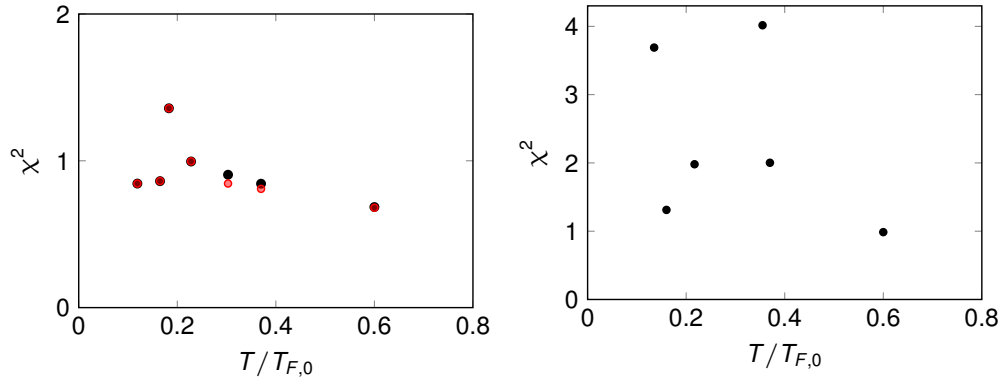
Figure 6.6: **The reduced chi-squared.** On the left, we see the χ^2 values for data on the near BCS side. The red points are fits where the width of the quasiparticles was a fit parameter (same as figure 6.5), and the black points were taken from fits where the width was constrained to be much smaller than the resolution. The plot on the right shows the χ^2 values for fits of data taken on the near BEC side.

I_{coherent} and not. For the most part, this only affects the highest three temperatures and then only slightly. For the data at $(k_F a)^{-1} = 0.23(3)$, I do not include an additional width parameter in the fits.

Figure 6.7 shows Z, the best fit value for the quasiparticle fraction for $(k_F a)^{-1} = -0.24(2)$ and $(k_F a)^{-1} = 0.23(3)$. One might expect that the quasiparticle fraction would increase with

Figure 6.7: **The quasiparticle fraction.** The results on the left were taken at $(k_F a)^{-1} = -0.24(2)$, and those on the right were taken at $(k_F a)^{-1} = 0.23(3)$. As before, red points indicate that σ was a fit parameter, and black points indicate that the width of I_{coherent} was fixed to a value much smaller than the resolution.

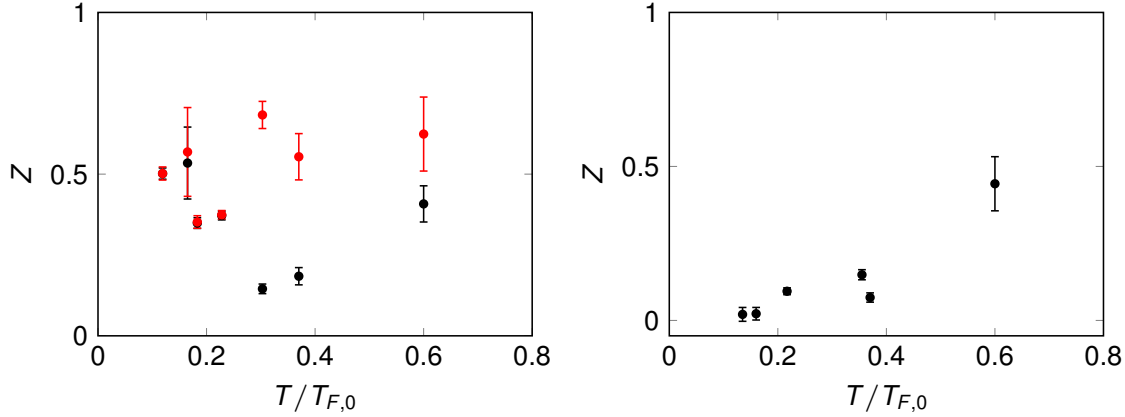temperature and possibly gradually go to 1 as T crosses T^*. The value of T^* has never been measured experimentally for atoms in the BCS-BEC crossover, but there have been a few predictions from various theories. Perali et al predict T^* of a homogeneous gas at unitarity to be roughly 0.55 T_F [102]. Sá De Melo et al predict that the pseudogap region closes at $T = 0.45 T_F$ at unitarity [103]. By these predictions, only the data set at the highest temperature on either side of the resonance would be above T^*. In this case, we might not expect to see Z = 1 because we are never hot enough. On the other hand, it is interesting to note that the highest temperature PES data at either interaction strength look remarkably similar. This may suggest that both sets are above T^*.

While the data show an increase of Z from 0 to 0.44 at $(k_F a)^{-1} = 0.23(3)$, the trend is less clear at $(k_F a)^{-1} = -0.24(2)$. This could be for several reasons. One reason might relate to the quasiparticle width; if the width is allowed to be fit to the values in figure 6.5 (red points in figure 6.7a), Z has a more monotonic trend. It is problematic, however, that this difference in the best fit value of Z does not lead to much change in χ^2.

The quasiparticle parameters that we get from fitting, such as the effective mass and the temperature, show the expected trends. (Since the effective mass is determined by the slope of the quasiparticle dispersion, and the temperature is determined by how quickly the quasiparticle signal

Figure 6.8: **The effective mass at** $(k_F a)^{-1} = -0.24(2)$**.** Red points indicate that σ was a fit parameter, and black points indicate that the width of I_{coherent} was fixed to $\sigma << 2.4$ kHz.

disappears with increasing energy, it may be that a Z value which underestimates the quasiparticle fraction still returns the correct value for these other parameters.) Figure 6.8 shows the effective mass extracted from I_{coherent} as a function of temperature. m^* starts higher than the bare mass (by 20%) and drops as temperature increases until it becomes consistent with the bare mass near $T/T_{F,0} = 0.3$. This decrease with increasing temperature is expected; quasiparticles in a Fermi liquid are only well-defined for low temperatures, and at high enough temperature, we expect the excitations to look like bare ^{40}K atoms with a mass equal to the bare mass. The transition from a system with dressed quasiparticles to one of bare particles could be thought of as another breakdown of the Fermi liquid description—this time due to temperature, rather than interaction strength.

The temperature of the quasiparticles is also a parameter in the fitting function. Figure 6.9 shows this temperature. We find that the best fit value for the temperature follows the trend of increasing temperature nicely, with the fit T/T_F slightly above $T/T_{F,0}$.
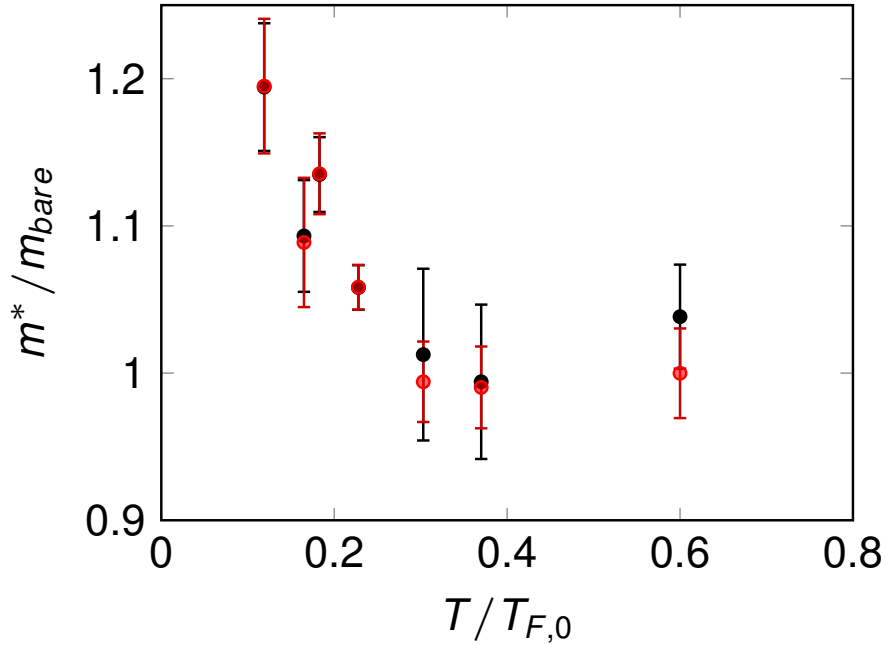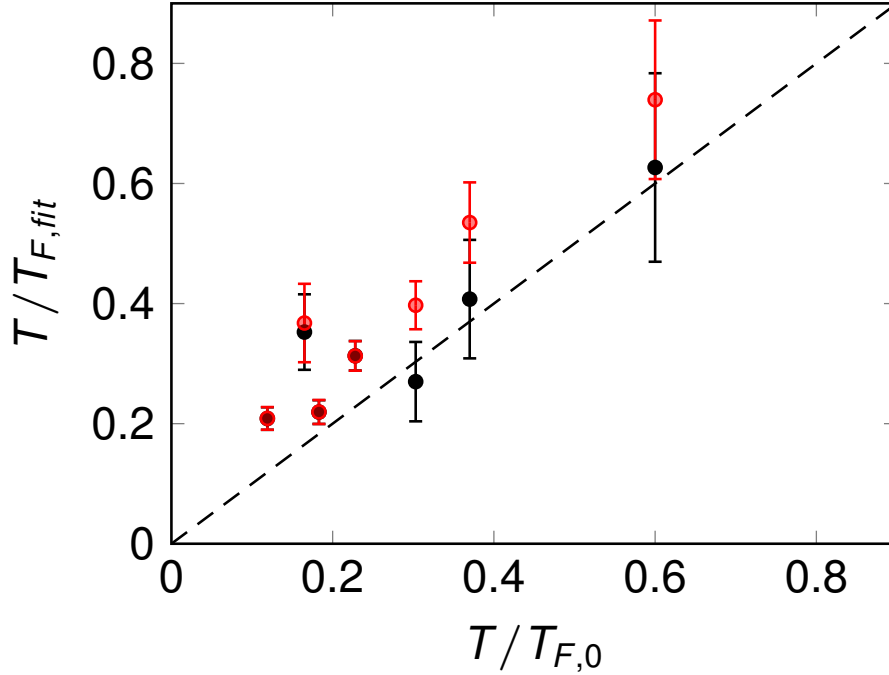
Figure 6.9: **The fitted T/T_F from I_{coherent}.** These data were taken at $(k_F a)^{-1} = -0.24(2)$. Red points indicate that σ was a fit parameter, and black points indicate that the width of I_{coherent} was fixed to a negligibly small value. The dashed line indicates $T/T_{F,fit} = T/T_{F,0}$. The fit to the data returns a slightly higher temperature than the initial temperature at $a = 1100a_0$, which is consistent with results at unitarity (figure 5.12a).

6.5   Conclusions

The PES data that we took for different temperatures on either side of the crossover has the potential to answer some interesting questions regarding the role of temperature in the Fermi liquid description and in the formation of pairs. In this chapter, I have presented some limited preliminary data that was analyzed using our two-part phenomenological model. I also used the data to extract the first measurement of the homogeneous contact as a function of temperature at interaction strengths other than unitarity.

There are several ways we might proceed. If we were to analyze data where we would expect only coherent signal or only pair-like signal, we could look at the evolution of these signals as a function of temperature separately. This would be easily done by taking data farther from unitarity on either side of the crossover. We might also be able to separate out the quasiparticle signal by

looking directly at the coherence, as others have done in the past [104]. I believe that further investigation into this regime would yield very interesting results.

Chapter 7

Conclusions

7.1   Summary

In this thesis, I have discussed experimental work on ultracold Fermi gases carried out at JILA in the past four years. The main body of work in this thesis involves the use of a spatially selective imaging technique that allows us to take measurements from a region of the trapped gas that has a nearly homogeneous density. I described how the use of beams with a Laguerre-Gaussian (LG) profile tuned to an optical pumping frequency achieve this end, and I described the optical setup and several procedures we employ for aligning and characterizing the LG beams.

Most of this thesis is taken from experiments that lead to the publication of Refs. [43], [49], and [75]. In the first, we used the spatially selective imaging technique to reveal the "textbook" sharp step in the ideal Fermi momentum distribution. In the second, we measured the contact of a homogeneous Fermi gas with strong interactions as a function of temperature. We saw a sharp drop in the value of the contact near the superfluid transition; this feature would not be visible in measurements of the contact of a gas with inhomogeneous density. In the last reference, we combined atom photoemission spectroscopy with the spatially selective imaging to measure the occupied spectral function of a Fermi gas for different interaction strength in the BCS-BEC crossover. To understand our results, we used a phenomenological model that splits the signal into two parts: a part resembling quasiparticles and a part based on thermal pairs. We found that this model described our data well, and this led to interesting intuition about the nature of non-superfluid gas in the BCS-BEC crossover. Finally, I presented some photoemission spectroscopy data taken

for different temperatures in the crossover. This data is preliminary, and the higher temperature behavior may not be fully captured by the phenomenological model previously employed. However, these first results are interesting and, this subject is worth pursuing with further research.

7.2   Future Possibilities

The future study of Fermi gases in the BCS-BEC crossover has many possible directions. Many of these possibilities follow naturally from the work presented here. For instance, the temperature dependence of the contact of a homogeneous gas in the crossover has been studied in depth only at unitarity. The preliminary results from chapter 6 indicate an increase in the steepest of the slope of the contact as a function of temperature as one crosses from the BCS side to the BEC side that deserves more investigation. The preliminary data in chapter 6 also indicates that extending the photoemission spectroscopy data to more temperatures (both higher and lower) in the BCS-BEC crossover would be very interesting.

Besides temperature and interaction strength, an important variable in the study of strongly interacting Fermi gases is the relative population of the two atomic spin states. All of the work presented here is carried out with ^{40}K in an equal mixture of two spins states, but there are systems in nature composed of strongly interacting fermions with imbalanced populations; the mixture of neutrons and protons in heavy atomic nuclei is an important example. The connection between the polaron picture (maximum population imbalance) and the results for a balanced gas discussed in section 5.4.1 is interesting and worth further research. In addition, it would be interesting to measure the contact of an imbalanced gas. The contact of an imbalanced gas is predicted to be equal for the minority and majority states. This prediction has interesting implications for the structures of heavy nuclei and of neutron stars.

In chapter 5, I briefly mentioned the problem of thermometry of a gas away from unitarity. The equation of state of a Fermi gas at different interaction strengths in the crossover has been measured but only for zero temperature [4]. Measuring the temperature for any interaction strength is an important piece still missing from our understanding of the BCS-BEC crossover.

In chapter 5, I also briefly mentioned that, while atom photoemission spectroscopy measures the occupied part of the atoms' spectral function, the unoccupied branches remain unknown. Researchers have had luck with injection spectroscopy (the inverse of photoemission spectroscopy, where you couple atoms into the system instead of outcoupling them) for measuring short-lived states in Rb-Cs mixtures [104]. This technique could possibly be adapted to measure the unoccupied spectral function. Being able to measure the unoccupied branch would immediately allow us to extract the superfluid gap, as well as allow us to directly look for a pseudo-gap above the superfluid transition temperature.

The immediate future of Fermi gas research at JILA involves the construction of a new experimental setup. In December of 2014, the 17-year-old apparatus in which the entirety of work from this thesis had been carried out was retired and disassembled for parts. The new apparatus has been designed, assembled, and baked, and optimization is currently being carried out for the creation an ultracold gas of ^{40}K atoms. The new apparatus should have faster experimental cycle times and better optical access in the final chamber. I look forward to seeing which new avenues of research will be pursued and where they will lead.

Bibliography

[1] J. T. Stewart, J. P. Gaebler, and D. S. Jin, "Using photoemission spectroscopy to probe a strongly interacting Fermi gas," <u>Nature</u>, vol. 454, pp. 744–747, Aug. 2008.

[2] S. Tan, "Large momentum part of a strongly correlated Fermi gas," <u>Annals of Physics</u>, vol. 323, pp. 2971–2986, 2008.

[3] J. T. Stewart, J. P. Gaebler, T. E. Drake, and D. S. Jin, "Verification of universal relations in a strongly interacting Fermi gas," <u>Physical Review Letters</u>, vol. 104, p. 235301, June 2010.

[4] N. Navon, S. Nascimbène, F. Chevy, and C. Salomon, "The equation of state of a low-temperature Fermi gas with tunable interactions," <u>Science</u>, vol. 328, no. 5979, pp. 729–732, 2010.

[5] M. Horikoshi, S. Nakajima, M. Ueda, and T. Mukaiyama, "Measurement of universal thermodynamic functions for a unitary Fermi gas," <u>Science</u>, vol. 327, no. 5964, pp. 442–445, 2010.

[6] S. Krinner, D. Stadler, D. Husmann, J.-P. Brantut, and T. Esslinger, "Observation of Quantized Conductance in Neutral Matter," <u>Nature</u>, vol. 517, no. 7532, pp. 64–67, 2015.

[7] N. Q. Burdick, K. Baumann, Y. Tang, M. Lu, and B. L. Lev, "Fermionic suppression of dipolar relaxation," <u>PRL</u>, vol. 114, no. 023201, 2015.

[8] M. K. Tey, S. Stellmer, R. Grimm, and F. Schreck, "Double-degenerate Bose-Fermi mixture of strontium," <u>Physical Review A - Atomic, Molecular, and Optical Physics</u>, vol. 82, no. 1, pp. 82–85, 2010.

[9] Z. G. Sheng, M. Nakamura, W. Koshibae, T. Makino, Y. Tokura, and M. Kawasaki, "Magneto-tunable photocurrent in manganite-based heterojunctions," <u>Nature Communications</u>, vol. 5, no. 4584, 2014.

[10] B. V. Jacak and B. Muller, "The Exploration of Hot Nuclear Matter," <u>Science</u>, vol. 337, no. 6092, pp. 310–314, 2012.

[11] A. Damascelli, Z. Hussain, and Z. X. Shen, "Angle-resolved photoemission studies of the cuprate superconductors," <u>Reviews of Modern Physics</u>, vol. 75, pp. 473–541, Apr. 2003.

[12] M. Hashimoto, I. M. Vishik, R.-H. He, T. P. Devereaux, and Z.-X. Shen, "Energy gaps in high-transition-temperature cuprate superconductors," <u>Nature Physics</u>, vol. 10, no. 7, pp. 483–495, 2014.

[13] B. DeMarco, "Onset of Fermi Degeneracy in a Trapped Atomic Gas," Science, vol. 285, pp. 1703–1706, 1999.

[14] M. H. Anderson, J. R. Ensher, M. R. Matthews, C. E. Wieman, and E. A. Cornell, "Observation of bose-einstein condensation in a dilute atomic vapor," Science, vol. 269, no. 5221, pp. 198–201, 1995.

[15] K. B. Davis, M. O. Mewes, M. R. Andrews, N. J. Van Druten, D. S. Durfee, D. M. Kurn, and W. Ketterle, "Bose-Einstein condensation in a gas of sodium atoms," Physical Review Letters, vol. 75, no. 22, pp. 3969–3973, 1995.

[16] C. Bradley, C. Sackett, J. Tollett, and R. Hulet, "Evidence of Bose-Einstein Condensation in an Atomic Gas with Attractive Interactions," Physical Review Letters, vol. 75, no. 9, 1995.

[17] S. Inouye, M. R. Andrews, J. Stenger, H.-J. Miesner, D. M. Stamper-Kurn, and W. Ketterle, "Observation of Feshbach resonances in a Bose-Einstein condensate," Nature, vol. 392, no. 6672, pp. 151–154, 1998.

[18] B. Demarco, Quantum Behavior of an Atomic Fermi Gas. PhD thesis, University of Colorado, 2001.

[19] C. Regal and D. S. Jin, "Experimental realization of BCS-BEC crossover physics with a Fermi gas of atoms," Adv. Atom. Mol. Opt. Phys., vol. 54, p. 1, 2005.

[20] V. N. Popov, "Theory of a Bose gas produced by bound states of Fermi particles," Soviet Physics Jetp-Ussr, vol. 50, no. 6, pp. 1034–1039, 1966.

[21] L. Keldysh and A. Kozlov, "Collective properties of excitons in semiconductors," Soviet Journal of Experimental and Theoretical Physics, vol. 27, no. 3, p. 521, 1968.

[22] D. Eagles, "Possible Pairing without Superconductivity at Low Carrier Concentrations in Bulk and Thin-Film Superconducting Semiconductors," Physical Review, vol. 186, no. 2, pp. 456–463, 1969.

[23] J. Bardeen, L. N. Cooper, and J. R. Schrieffer, "Theory of superconductivity," Physical Review, vol. 108, no. 5, pp. 1175–1204, 1957.

[24] C. A. R. Sá De Melo, "When fermions become bosons: Pairing in ultracold gases," Physics Today, vol. 61, pp. 45–51, Oct. 2008.

[25] C. A. Regal, M. Greiner, and D. S. Jin, "Observation of resonance condensation of fermionic atom pairs," Physical review letters, vol. 92, p. 040403, Jan. 2004.

[26] M. W. Zwierlein, C. A. Stan, C. H. Schunck, S. M. F. Raupach, A. J. Kerman, and W. Ketterle, "Condensation of Fermionic Atom Pairs Near a Feshbach Resonance," Phys. Rev. Lett., vol. 02139, no. 12, pp. 1–5, 2004.

[27] W. Ketterle and M. W. Zwierlein, "Making, probing, and understanding Fermi gases," in Ultracold Fermi Gases, Proceedings of the International School of Physics "Enrico Fermi" Course CLXIV (M. Inguscio, W. Ketterle, and C. Salomon, eds.), (Amsterdam), IOS Press, 2006.

[28] Z. Lu, K. Corwin, M. Renn, M. Anderson, E. Cornell, and C. Wieman, "Low-Velocity Intense Source of Atoms from a Magneto-optical Trap," Physical Review Letters, vol. 77, no. 16, pp. 3331–3334, 1996.

[29] J. Stewart, Probing a strongly interacting Fermi gas. PhD thesis, University of Colorado, 2004.

[30] A. L. Gaunt, T. F. Schmidutz, I. Gotlibovych, R. P. Smith, and Z. Hadzibabic, "Bose-Einstein Condensation of Atoms in a Uniform Potential," Physical Review Letters, vol. 110, p. 200406, May 2013.

[31] I. Gotlibovych, T. F. Schmidutz, A. L. Gaunt, N. Navon, R. P. Smith, and Z. Hadzibabic, "Observing properties of an interacting homogeneous Bose-Einstein condensate: Heisenberg-limited momentum spread, interaction energy, and free-expansion dynamics," Physical Review A - Atomic, Molecular, and Optical Physics, vol. 89, no. 6, pp. 1–5, 2014.

[32] T. F. Schmidutz, I. Gotlibovych, A. L. Gaunt, R. P. Smith, N. Navon, and Z. Hadzibabic, "Quantum Joule-Thomson effect in a saturated homogeneous bose gas," Physical Review Letters, vol. 112, no. 4, pp. 1–5, 2014.

[33] N. Navon, A. L. Gaunt, R. P. Smith, and Z. Hadzibabic, "Critical dynamics of spontaneous symmetry breaking in a homogeneous Bose gas," Science, vol. 347, no. 6218, pp. 167–170, 2015.

[34] B. Mukherjee, M. Ku, Z. Yan, P. Patel, E. Guardado-Sanchez, T. Yefsah, J. Struck, and M. W. Zwierlein, "A Fermi gas in a homogeneous box potential," in 46th Annual Meeting of the APS Division of Atomic, Molecular and Optical Physics, (Columbus, Ohio), 2015.

[35] S. Nascimbène, N. Navon, K. J. Jiang, F. Chevy, and C. Salomon, "Exploring the thermodynamics of a universal Fermi gas," Nature, vol. 463, no. 7284, pp. 1057–1060, 2010.

[36] M. J. H. Ku, A. T. Sommer, L. W. Cheuk, and M. W. Zwierlein, "Revealing the Superfluid Lambda Transition in the Universal Thermodynamics of a Unitary Fermi Gas," Science, vol. 335, no. 6068, pp. 563–567, 2012.

[37] D. S. Jin, B. DeMarco, and S. Papp, "Exploring a quantum degenerate gas of fermionic atoms," in AIP Conference Proceedings 551, vol. 414, p. 5, AIP Publishing, 1998.

[38] N. R. Heckenberg, R. McDuff, C. P. Smith, and A. G. White, "Generation of optical phase singularities by computer-generated holograms," Optics letters, vol. 17, no. 3, p. 221, 1992.

[39] S. N. Khonina, V. V. Kotlyar, R. V. Skidanov, V. A. Soifer, P. Laakkonen, and J. Turunen, "Gauss-Laguerre modes with different indices in prescribed diffraction orders of a diffractive phase element," Optics Communications, vol. 175, no. 4, pp. 301–308, 2000.

[40] S. Kennedy, M. Szabo, H. Teslow, J. Porterfield, and E. Abraham, "Creation of Laguerre-Gaussian laser modes using diffractive optics," Physical Review A, vol. 66, no. 4, pp. 1–5, 2002.

[41] K. C. Wright, L. S. Leslie, and N. P. Bigelow, "Optical control of the internal and external angular momentum of a Bose-Einstein condensate," Physical Review A - Atomic, Molecular, and Optical Physics, vol. 77, no. 4, pp. 1–4, 2008.

[42] M. R. Andrews, "Observation of Interference Between Two Bose Condensates," Science, vol. 275, no. 5300, pp. 637–641, 1997.

[43] T. E. Drake, Y. Sagi, R. Paudel, J. T. Stewart, J. P. Gaebler, and D. S. Jin, "Direct observation of the Fermi surface in an ultracold atomic gas," Physical Review A - Atomic, Molecular, and Optical Physics, vol. 86, Mar. 2012.

[44] D. H. Smith, E. Braaten, D. Kang, and L. Platter, "Two-body and three-body contacts for identical bosons near unitarity," Physical Review Letters, vol. 112, pp. 3–7, 2014.

[45] R. J. Wild, P. Makotyn, J. M. Pino, E. a. Cornell, and D. S. Jin, "Measurements of Tan's contact in an atomic bose-einstein condensate," Physical Review Letters, vol. 108, 2012.

[46] E. Braaten, D. Kang, and L. Platter, "Universal relations for identical bosons from three-body physics," Physical Review Letters, vol. 106, pp. 2–5, 2011.

[47] O. Hen, L. B. Weinstein, E. Piasetzky, G. A. Miller, M. M. Sargsian, and Y. Sagi, "Correlated Fermion Pairs in Nuclei and Ultracold Atomic Gases," arXiv:1407.8175v2, 2014.

[48] E. D. Kuhnle, S. Hoinka, P. Dyke, H. Hu, P. Hannaford, and C. J. Vale, "Temperature dependence of the universal contact parameter in a unitary Fermi gas," Physical Review Letters, vol. 106, p. 170402, Apr. 2011.

[49] Y. Sagi, T. E. Drake, R. Paudel, and D. S. Jin, "Measurement of the homogeneous contact of a unitary Fermi gas," Physical Review Letters, vol. 109, p. 220402, Nov. 2012.

[50] S. Tan, "Generalized virial theorem and pressure relation for a strongly correlated Fermi gas," Annals of Physics, vol. 323, pp. 2987–2990, 2008.

[51] S. Tan, "Annals of Physics Energetics of a strongly correlated Fermi gas," Annals of Physics, vol. 323, pp. 2952–2970, 2008.

[52] V. A. Belyakov, "The momentum distribution of particles in a dilute Fermi gas," Soviet Physics Jetp-Ussr, vol. 13, no. 4, pp. 2–3, 1961.

[53] M. Punk and W. Zwerger, "Theory of rf-spectroscopy of strongly interacting fermions," Physical Review Letters, vol. 99, p. 170404, Oct. 2007.

[54] G. Baym, C. J. Pethick, Z. Yu, and M. W. Zwierlein, "Coherence and clock shifts in ultracold Fermi gases with resonant interactions," Physical Review Letters, vol. 99, no. November, pp. 1–4, 2007.

[55] E. Braaten, "Universal relations for fermions with large scattering length," in Lecture Notes in Physics (W. Zwerger, ed.), vol. 836 of Lecture Notes in Physics, pp. 193–231, Springer Berlin / Heidelberg, 2012.

[56] E. Braaten, D. Kang, and L. Platter, "Short-time operator product expansion for rf spectroscopy of a strongly interacting Fermi gas," Physical Review Letters, vol. 104, pp. 4–7, 2010.

[57] S. Zhang and A. J. Leggett, "Universal properties of the ultracold Fermi gas," Physical Review A - Atomic, Molecular, and Optical Physics, vol. 79, p. 23601, 2009.

[58] F. Werner, L. Tarruell, and Y. Castin, "Number of closed-channel molecules in the BEC-BCS crossover," European Physical Journal B, vol. 68, no. 3, pp. 401–415, 2009.

[59] H. Hu, X.-J. Liu, and P. D. Drummond, "Static structure factor of a strongly correlated Fermi gas at large momenta," Europhys. Lett., vol. 20005, no. 91, p. 8, 2010.

[60] G. B. Partridge, K. E. Strecker, R. I. Kamar, M. W. Jack, and R. G. Hulet, "Molecular probe of pairing in the BEC-BCS crossover," Physical Review Letters, vol. 95, p. 20404, July 2005.

[61] E. D. Kuhnle, H. Hu, X. J. Liu, P. Dyke, M. Mark, P. D. Drummond, P. Hannaford, and C. J. Vale, "Universal behavior of pair correlations in a strongly interacting Fermi gas," Physical Review Letters, vol. 105, p. 70402, Aug. 2010.

[62] A. B. Bardon, S. Beattie, C. Luciuk, W. Cairncross, D. Fine, N. S. Cheng, G. J. A. Edge, E. Taylor, S. Zhang, S. Trotzky, and J. H. Thywissen, "Transverse demagnetization dynamics of a unitary Fermi gas," Science, vol. 344, no. May, pp. 722–4, 2014.

[63] J. Sakurai, Modern Quantum Mechanics. Addison-Wesley Publishing Company, Inc, 1985.

[64] R. Haussmann, W. Rantner, S. Cerrito, and W. Zwerger, "Thermodynamics of the BCS-BEC crossover," Physical Review A - Atomic, Molecular, and Optical Physics, vol. 75, p. 23610, Feb. 2007.

[65] F. Palestini, A. Perali, P. Pieri, and G. C. Strinati, "Temperature and coupling dependence of the universal contact intensity for an ultracold Fermi gas," Physical Review A - Atomic, Molecular, and Optical Physics, vol. 82, p. 21605, Aug. 2010.

[66] H. Hu, X. J. Liu, and P. D. Drummond, "Universal contact of strongly interacting fermions at finite temperatures," New Journal of Physics, vol. 13, no. 3, p. 35007, 2011.

[67] C. Chin, R. Grimm, P. Julienne, and E. Tiesinga, "Feshbach resonances in ultracold gases," Reviews of Modern Physics, vol. 82, pp. 1225–1286, Apr. 2010.

[68] J. E. Drut, T. A. Lähde, and T. Ten, "Momentum distribution and contact of the unitary Fermi gas," Physical Review Letters, vol. 106, p. 205302, May 2011.

[69] L. Luo and J. Thomas, "Thermodynamic Measurements in a Strongly Interacting Fermi Gas," J. Low Temp. Phys., vol. 154, no. 1, pp. 1–29, 2009.

[70] K. M. O'Hara, S. L. Hemmer, M. E. Gehm, S. R. Granade, and J. E. Thomas, "Observation of a strongly interacting degenerate Fermi gas of atoms," Science, vol. 298, pp. 2179–2182, 2002.

[71] J. T. Stewart, J. P. Gaebler, C. A. Regal, and D. S. Jin, "Potential energy of a 40K Fermi gas in the BCS-BEC crossover," Physical review letters, vol. 97, no. 22, p. 220406, 2006.

[72] J. P. Gaebler, Photoemission spectroscopy of a strongly interacting Fermi gas. PhD thesis, University of Colorado, 2010.

[73] J. P. Gaebler, J. T. Stewart, T. E. Drake, D. S. Jin, A. Perali, P. Pieri, and G. C. Strinati, "Observation of pseudogap behavior in a strongly interacting Fermi gas," Nat. Phys., vol. 6, pp. 569–573, Aug. 2010.

[74] A. Perali, F. Palestini, P. Pieri, G. C. Strinati, J. T. Stewart, J. P. Gaebler, T. E. Drake, and D. S. Jin, "Evolution of the normal state of a strongly interacting Fermi Gas from a Pseudogap phase to a molecular Bose gas," Physical Review Letters, vol. 106, p. 60402, Feb. 2011.

[75] Y. Sagi, T. E. Drake, R. Paudel, R. Chapurin, and D. S. Jin, "Breakdown of the Fermi Liquid Description for Strongly Interacting Fermions," Physical Review Letters, vol. 114, no. 075301, pp. 1–5, 2015.

[76] Q. Chen, J. Stajic, S. Tan, and K. Levin, "BCS-BEC crossover: From high temperature superconductors to ultracold superfluids," Physics Reports, vol. 412, no. 1, pp. 1–88, 2005.

[77] M. Randeria, W. Zwerger, and M. Zwierlein, The BCS-BEC Crossover and the Unitary Fermi Gas, vol. 836 of Lecture Notes in Physics. Springer, 2011.

[78] M. Randeria and E. Taylor, "Crossover from Bardeen-Cooper-Schrieffer to Bose-Einstein Condensation and the Unitary Fermi Gas," Annual Review of Condensed Matter Physics, vol. 5, no. 1, pp. 209–232, 2014.

[79] A. Abrikosov and I. Khalatnikov, "The theory of a Fermi liquid," Soviet Physics Jetp-Ussr, vol. 3, no. 6, pp. 329–367, 1957.

[80] E. M. Lifshitz and L. P. Pitaevskii, Statistical Physics, Part 2, vol. 9 of Landau and Lifshitz Course of Theoretical Physics. Butterworth-Heinemann, 1980.

[81] R. W. Hill, C. Proust, L. Taillefer, P. Fournier, and R. L. Greene, "Breakdown of Fermi-liquid theory in a copper-oxide superconductor," Nature, vol. 414, no. 6865, pp. 711–715, 2001.

[82] A. Sommer, M. Ku, G. Roati, and M. W. Zwierlein, "Universal spin transport in a strongly interacting Fermi gas," Nature, vol. 472, no. 7342, pp. 201–204, 2011.

[83] Q. Chen, Y. He, C.-C. Chien, and K. Levin, "Theory of Radio Frequency Spectroscopy Experiments in Ultracold Fermi Gases and Their Relation to Photoemission Experiments in the Cuprates," Rep. Prog. Phys., vol. 72, p. 23, 2008.

[84] S. Nascimbène, N. Navon, S. Pilati, F. Chevy, S. Giorgini, A. Georges, and C. Salomon, "Fermi-liquid behavior of the normal phase of a strongly interacting gas of cold atoms," Physical Review Letters, vol. 106, p. 215303, May 2011.

[85] D. Wulin, H. Guo, C. C. Chien, and K. Levin, "Spin transport in cold Fermi gases: A pseudogap interpretation of spin diffusion experiments at unitarity," Physical Review A - Atomic, Molecular, and Optical Physics, vol. 83, p. 61601, 2011.

[86] R. Haussmann, M. Punk, and W. Zwerger, "Spectral functions and rf response of ultracold fermionic atoms," Physical Review A - Atomic, Molecular, and Optical Physics, vol. 80, p. 63612, Dec. 2009.

[87] Z.-X. Shen, "Stanford Shen Laboratory Website, https://arpes.stanford.edu/."

[88] T. L. Dao, A. Georges, J. Dalibard, C. Salomon, and I. Carusotto, "Measuring the one-particle excitations of ultracold fermionic atoms by stimulated Raman spectroscopy," Physical Review Letters, vol. 98, no. 24, pp. 1–4, 2007.

[89] M. Veillette, E. G. Moon, A. Lamacraft, L. Radzihovsky, S. Sachdev, and D. E. Sheehy, "Radio-frequency spectroscopy of a strongly imbalanced Feshbach-resonant Fermi gas," Physical Review A - Atomic, Molecular, and Optical Physics, vol. 78, p. 33614, Sept. 2008.

[90] W. Schneider and M. Randeria, "Universal short-distance structure of the single-particle spectral function of dilute Fermi gases," Physical Review A - Atomic, Molecular, and Optical Physics, vol. 81, p. 21601, Feb. 2010.

[91] C. Chin and P. S. Julienne, "Radio-frequency transitions on weakly bound ultracold molecules," Physical Review A - Atomic, Molecular, and Optical Physics, vol. 71, p. 12713, Jan. 2005.

[92] E. V. H. Doggen and J. J. Kinnunen, "Momentum-resolved spectroscopy of a Fermi liquid," arXiv:1411.7207, Nov. 2014.

[93] R. Combescot, S. Giraud, and X. Leyronas, "Analytical theory of the dressed bound state in highly polarized Fermi gases," Europhys. Lett., vol. 88, no. 6, p. 5, 2009.

[94] P. Magierski, G. Wlazowski, A. Bulgac, and J. E. Drut, "Finite-Temperature Pairing Gap of a Unitary Fermi Gas by Quantum Monte Carlo Calculations," Physical Review Letters, vol. 103, p. 210403, Nov. 2009.

[95] J. J. Kinnunen, "Hartree shift in unitary Fermi gases," Physical Review A - Atomic, Molecular, and Optical Physics, vol. 85, p. 12701, Jan. 2012.

[96] G. M. Bruun and G. Baym, "Bragg spectroscopy of cold atomic Fermi gases," Physical Review A - Atomic, Molecular, and Optical Physics, vol. 74, p. 33623, 2006.

[97] A. Schirotzek, C. H. Wu, A. Sommer, and M. W. Zwierlein, "Observation of Fermi polarons in a tunable fermi liquid of ultracold atoms," Physical Review Letters, vol. 102, p. 230402, June 2009.

[98] N. Prokof'ev and B. Svistunov, "Fermi-polaron problem: Diagrammatic Monte Carlo method for divergent sign-alternating series," Physical Review B - Condensed Matter and Materials Physics, vol. 77, p. 20408, Jan. 2008.

[99] N. V. Prokof'ev and B. V. Svistunov, "Bold diagrammatic Monte Carlo: A generic sign-problem tolerant technique for polaron models and possibly interacting many-body problems," Physical Review B - Condensed Matter and Materials Physics, vol. 77, p. 125101, Mar. 2008.

[100] M. Punk, P. T. Dumitrescu, and W. Zwerger, "Polaron-to-molecule transition in a strongly imbalanced Fermi gas," Physical Review A - Atomic, Molecular, and Optical Physics, vol. 80, p. 53605, Nov. 2009.

[101] E. Braaten, D. Kang, and L. Platter, "Universal relations for a strongly interacting Fermi gas near a Feshbach resonance," Physical Review A - Atomic, Molecular, and Optical Physics, vol. 78, p. 53606, Nov. 2008.

[102] A. Perali, P. Pieri, L. Pisani, and G. C. Strinati, "BCS-BEC crossover at finite temperature for superfluid trapped Fermi atoms," Physical Review Letters, vol. 92, no. 22, pp. 220404–1, 2004.

[103] C. A. R. Sá De Melo, M. Randeria, and J. R. Engelbrecht, "Crossover from BCS to Bose superconductivity: Transition temperature and time-dependent Ginzburg-Landau theory," Physical Review Letters, vol. 71, pp. 3202–3205, Nov. 1993.

[104] C. Kohstall, M. Zaccanti, M. Jag, A. Trenkwalder, P. Massignan, G. M. Bruun, F. Schreck, and R. Grimm, "Metastability and coherence of repulsive polarons in a strongly interacting Fermi mixture," Nature, vol. 485, no. 7400, pp. 615–618, 2012.

Appendix A

Thermometry

Our thermometry assumes a knowledge of the trapping potential $V(\mathbf{r})$ and the equation of state $n(\mu, T)$, where T is the temperature and μ is the chemical potential. For a non-interacting gas the equation of state is known, and for the unitary gas, we use the equation of state recently measured at MIT [36]. The trapping potential is calibrated from the known optical trap beam waists and the measured oscillation frequencies in all three directions. We adopt a local density approximation approach; the local chemical potential is given by $\mu(\mathbf{r}) = \mu_0 - V(\mathbf{r})$. For a given T and number of atoms, N, μ_0 is set by the normalization requirement $N = \int n[\mu(\mathbf{r}), T] \, \mathrm{d}^3\mathbf{r}$. The equation of state then determines the complete density profile $n(\mathbf{r})$, from which we can calculate other quantities such as the entropy, total energy, release energy, and shape of the cloud. Since we measure N, we get a one-to-one correspondence between T and these quantities, and therefore any of them can serve as a thermometer. With the unitary gas, we have chosen to use the release energy as a thermometer.

We determine the release energy by measuring the cloud after it expands at unitary for 4 ms. The release energy per particle is calculated from the measured density profile of the expanded gas using

$$E_{\mathrm{rel}} = \sum_{i=x,y,z} E_{i,\mathrm{rel}} = \frac{1}{N} \sum_{i=x,y,z} \int \frac{m}{2} \left(\frac{r_i}{t}\right)^2 [n_t(\mathbf{r}) - n_0(\mathbf{r})] \mathrm{d}^3\mathbf{r} \quad , \tag{A.1}$$

where r_i is the corresponding spatial coordinate $(i = x, y, z)$, t is the expansion time, and $n_t(\mathbf{r})$ is the density distribution at time t. In the experiment, we use $t = 4$ ms. We have verified that the release energy measured at $t = 4$ ms is the same as that measured after 12 ms of expansion. For a

given potential $V(\mathbf{r})$, the release energy is given by [69]:

$$E_{\text{rel}} = \frac{1}{2}\langle \mathbf{r} \cdot \nabla V(\mathbf{r})\rangle \quad , \tag{A.2}$$

where the symbol $\langle\rangle$ stands for the density-weighted average: $\langle g(\mathbf{r})\rangle = \frac{1}{N}\int g(\mathbf{r})n(\mathbf{r})\mathrm{d}^3\mathbf{r}$. By equating the calculated $E_{\text{rel}}(T)$ to the measured E_{rel}, we determine T.

As a comparison, we have used two other techniques to extract the temperature of the unitary gas. The first technique we compare to is based on the widely used practice of fitting the strongly interacting gas to a Thomas-Fermi distribution and extracting an empirical temperature, $\tilde{T}$, from the fitted fugacity [48]. At $T = 0$, the empirical temperature is connected to the real temperature by $T = \tilde{T}\sqrt{\xi}$, where ξ is the universal constant defined above [27]. Albeit without a complete theoretical justification, one can then extend this to finite temperatures and extract T [48]. In the following analysis, shown as the blue triangles in figure A.1, we used $\xi = 0.376$ [36].

The second thermometry method we compare to is based on the entropy of the weakly interacting gas before the ramp to unitarity. We calculate the entropy of the weakly interacting gas from the measured temperature and the trapping potential. In the experiment, we start from the weakly interacting gas and slowly ramp to the Fano-Feshbach resonance field. By performing this ramp there and back and comparing the entropy before and after the ramp for a gas initially at $T/T_F = 0.12$ and $T/T_F = 0.22$, we have determined that the entropy increases by about 6% when going to the Fano-Feshbach resonance field. Assuming this increase, we use the entropy of the unitary gas together with the equation of state as the thermometer. In figure A.1, the T/T_F we obtain from these two additional techniques are plotted against the release energy thermometry. We find a good agreement between all the three techniques up to $T/T_F = 0.4$. Above that temperature, the empirical temperature technique becomes unreliable since the effect of quantum degeneracy of the shape of the cloud diminishes. The entropy technique starts to show a small systematic deviation upwards above $T/T_F = 0.4$. The close agreement of the three techniques, which are based on independent observables, up to $T/T_F = 0.4$ gives us confidence in our thermometry. To estimate the errors in T we look at the difference between the entropy and release energy
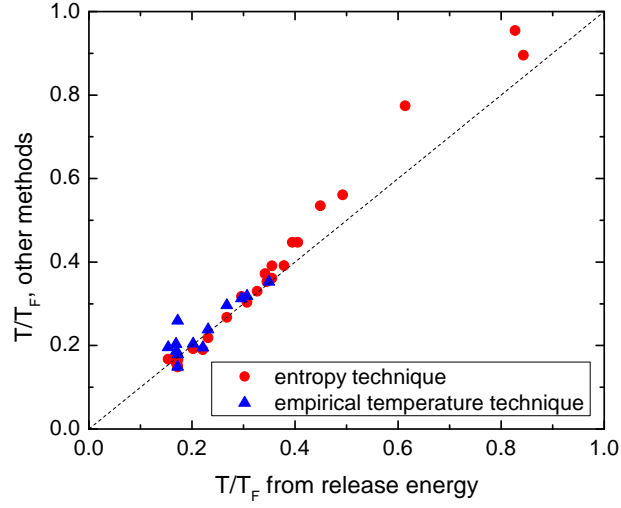
thermometry techniques.

Figure A.1: Comparison of different thermometry methods. The x-axis is the temperature, T/T_F, where T_F is the trap Fermi temperature, as extracted from the release energy. The y-axis is the temperature we get from the two other thermometry methods (see text for more details). The dashed line is $y = x$.

Appendix B

Scaling the number of atoms in PES data

When taking an rf line shape to extract the contact, we increase the power of our rf pulse for large detunings in order to increase our signal to noise when there is very low signal (see section 4.2.2.1). This technique is even more necessary for photoemission spectroscopy, where, in addition to measuring number, we resolve the momentum distribution of the atoms outcoupled for each detuning (chapter 5).

As described in chapter 4, section 4.2.2.1, we measure the number of atoms outcoupled as a function of power for several detunings, ν, and use the results of this measurement to determine how to scale the data at each ν for PES to correspond to the signal for a single rf power. We fit the number outcoupled vs. power to an exponential and used the linear approximation to scale down the number of atoms from shots with higher rf powers:

$$N_{\text{out}} = A(1 - e^{-P/P_0}) \approx A\frac{P}{P_0} \tag{B.1}$$

However, for the contact data, we keep the power sufficiently low such that this approximation is correct to within 10%. For the PES data, in order to get more signal in the high-momentum, negative energy portion of the plots, we use a higher rf pulse power and scale the number using the full exponential. Below is a table of the calibrated P_0 that we used for the PES data:

detuning [kHz]	P_0 [arb]
-25	6.3
-5	0.70
-0	0.15
5	0.092
20	1.4
40	8.0
60	19.8
80	32.3

Table B.1: The measured saturation power, P_0, in arbitrary units, for different rf frequency detunings. These results are consistent with figure 4.7. The slight differences come from slight changes in the electronics over time. As before, we see that P_0 increases with increasing detuning, and is lowest near the center of the line shape, where the larger numbers of atoms available to be outcoupled cause the signal to saturate at lower powers.

Note that, for the PES data, we scaled the signal for frequencies lower than ν_0 as well as higher. We did this to be certain that the increased power wasn't outcoupling signal from the center of the line shape; if it had been, extra signal would have appeared at negative frequencies as well. This also allowed us to reduce the noise in the negative detuning region.

For PES data, we also vary the pulse duration as we change frequencies—a total duration of 300 μs for $\nu < 34$ kHz and 100 μs for $\nu > 34$ kHz. We find that the ratio of the saturation powers, P_0, of two different pulse durations is equal to the ratio of the pulse durations (see figure B.1). In the linear regime (away from saturation effects), this means that the number of atoms outcoupled is scaled by the ratio of pulse durations, as you would expect.
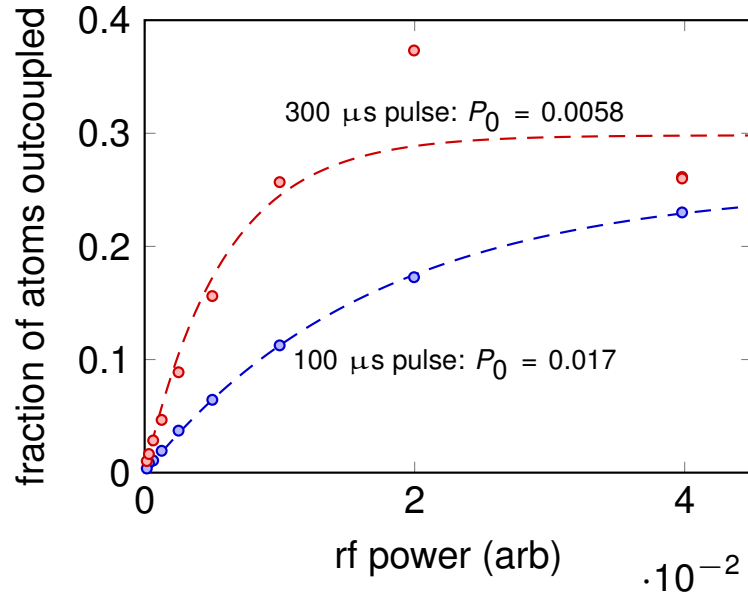
Figure B.1: **Fraction of atoms outcoupled vs rf power.** At a detuning of $\nu = 80$ kHz, we measured the number of atoms outcoupled by a 300 μs pulse and a 100 μs pulse. (Here, the quited pulse duration corresponds to four times the $1/e^2$ amplitude half width.) For data taken at this detuning, we use the 100 μs pulse and, staying in the linear regime, increase the number of atoms by a factor of three to compare it with data taken at small detunings using a 300 μs pulse.

Appendix C

Comparing PES of a homogeneous sample to trap-averaged data

C.1   Back-bending of EDCs

To compare the nearly homogeneous data with previously published trap-averaged data, we use the analysis described in Ref. [73]. Specifically, independent Gaussian fits to fixed-k traces through the PES data are used to find a dispersion $E(k)$. Figure C.1**a** shows the nearly homogeneous PES data for $(k_F a)^{-1} = 0.1$, with white points marking the centers from the Gaussian fits. Figure C.1**b** shows the fixed-k traces through the data, which are often called energy distribution curves, or EDCs. These plots can be compared to figures 1 and 2 of Ref. [73], which show trap-averaged data at $(k_F a)^{-1} \approx 0.15$ and $T/T_C = 1.24$. We find that the PES results for a nearly homogeneous gas are qualitatively similar to the trap-averaged results. Specifically, in both cases we see dispersions that exhibit large energy widths and back-bending.

In the two-mode model, the combination of the positively dispersing coherent part and the incoherent part can produce a spectral function that exhibits back-bending. To demonstrate this, in figure C.2 we calculate the dispersion with the two-mode model using parameters similar to those from our fits and find the peak using the same analysis technique as was in Ref. [73]. The resulting dispersion clearly shows a BCS-like back-bending.
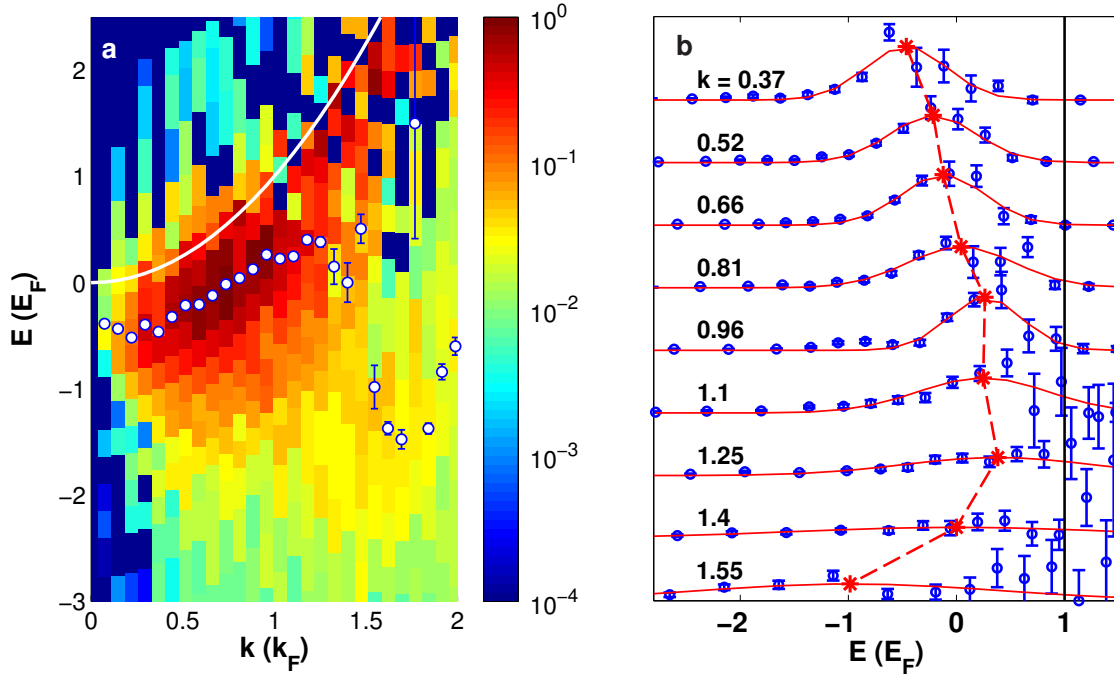
Figure C.1: **Gaussian fits to PES data at $(\mathbf{k_F a})^{-1} = 0.1$. a**, The white circles indicate the centers from weighted Gaussian fits to EDCs at fixed k. The white line shows the free-particle dispersion, $E = k^2$. **b**, Individual EDCs (blue points) are shown, along with the fitted Gaussian (red lines). Here, each EDC is individually normalized to have the same area, as in Ref. [73]. A solid black line marks $E = E_F$. Red stars show the center of each Gaussian, and the dashed red line is a guide to the eye.
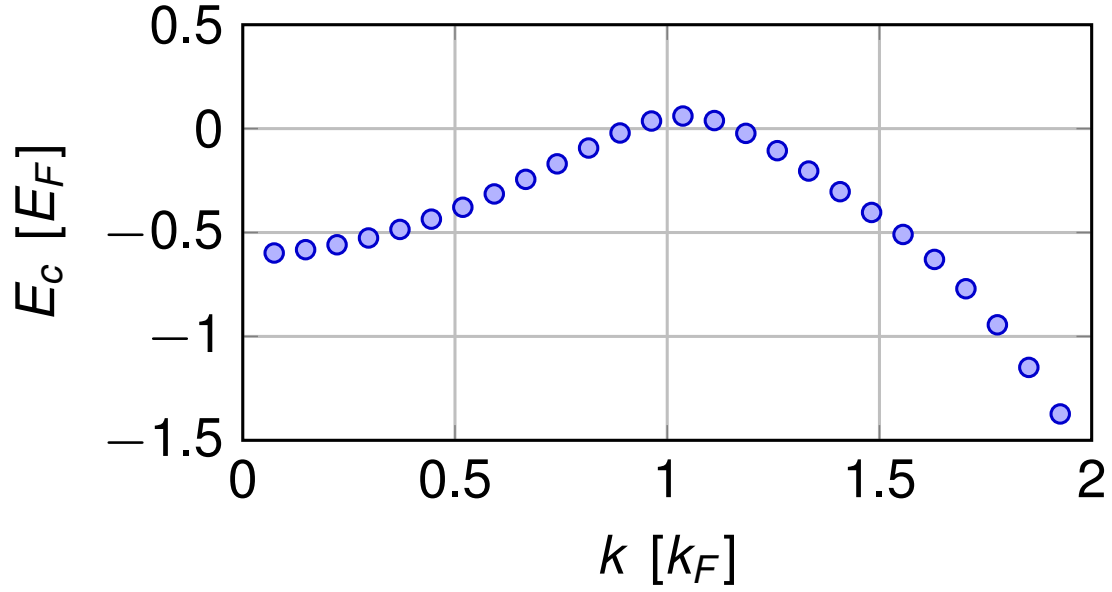
Figure C.2: **Back-bending in the two-mode model.** We generate a simulated spectral function using the two-mode model with the following parameters: $Z = 0.2$, $m^* = 1.2$, $T = 0.25$, $E_0 = -0.5$, $\mu = -0.5$, $E_p = 0.5$, $T_p = 0.75$. Each point in this figure was then obtained by fitting the spectral function at a given momentum k by the Gaussian function $Ae^{-(E-E_c)^2/2\sigma^2}$. In the fits, the value of σ was constrained to be above the experimental resolution.

Appendix D

Derivation of the single-particle spectral function for atoms bound in thermal pairs

As the title of this section might suggest, understanding what we expect thermal pairs to look like in our PES signal is not straightforward. PES measures the energies and momenta of single particles, which means that in addition to outcoupling the atom to a weakly interacting state, the rf photon must also overcome the binding energy of the pair.

To derive the functional form of our model, we first consider a single stationary pair that is dissociated by absorbing an rf photon. For rf dissociation, energy conservation gives

$$- E_p + h\nu = E_{\rm rel}, \tag{D.1}$$

where $E_{\rm rel} = \frac{\hbar^2 k_{\rm rel}^2}{m}$ is the relative kinetic energy of the two resulting atoms after dissociation and $E_p = \frac{\hbar^2}{mR^2}$ is the binding energy corresponding to a bound wave function $\phi(r) = \sqrt{\frac{2}{R}} e^{-r/R}$. On the other hand, in PES [1], the single-particle energy E is given by

$$E + h\nu = \frac{\hbar^2 k^2}{2m}, \tag{D.2}$$

where $\hbar k$ is the momentum of the spin-flipped atom. If the pair is initially at rest, the two resulting atoms will have momenta $\hbar \mathbf{k}_{\rm rel}$ and $-\hbar \mathbf{k}_{\rm rel}$, so that combining equations D.2 and D.1, we find $E = -E_p - \frac{\hbar^2 k^2}{2m}$. Here, we can see that pair dissociation yields a negative, quadratic single-particle dispersion.

The amplitude of the signal as a function of k can be obtained from the normalized rf line

shape for the dissociation of a weakly bound molecule, which was derived by Chin and Julienne [91]:

$$F(E_{\text{rel}}) = \frac{2}{\pi} \frac{\sqrt{E_{\text{rel}} E_p}}{(E_{\text{rel}} + E_p)^2}, \tag{D.3}$$

where $\int_0^\infty F(E_{\text{rel}}) dE_{\text{rel}} = 1$ and we have assumed that the final state is weakly interacting. Equation D.3 can be rewritten in terms of k_{rel} to give

$$G(k_{\text{rel}}) = \frac{\hbar^3}{\pi^2 m^{3/2}} \frac{\sqrt{E_p}}{(\hbar^2 k_{\text{rel}}^2/m + E_p)^2}, \tag{D.4}$$

where $\int_0^\infty G(k_{\text{rel}}) 4\pi k_{\text{rel}}^2 dk_{\text{rel}} = 1$. This line shape is highly asymmetric and has an extent in k_{rel} that scales as $\sqrt{E_p}$, or equivalently $1/R$. At high k_{rel}, $G(k_{\text{rel}})$ falls off as $1/k_{\text{rel}}^4$, which is consistent with Tan's contact.

If the pair is moving, then combining equation D.2 and D.1 gives

$$E = -E_p - \frac{\hbar^2 k_{\text{rel}}^2}{m} + \frac{\hbar^2 k^2}{2m}. \tag{D.5}$$

In PES, we apply rf with detuning ν, measure k for the spin-flipped atom, and extract E using equation D.2. From equation D.5, we see that for the dissociation of non-stationary pairs, data with a particular k (but variable ν) can, in principle, yield E anywhere in the range $-E_p - \frac{\hbar^2 k^2}{2m} \leq E \leq -E_p + \frac{\hbar^2 k^2}{2m}$, where the lower limit corresponds to a stationary pair and the upper limit corresponds to a pair with the maximum possible center-of-mass momentum, $\hbar \mathbf{K}_{\text{cm}} = 2\hbar \mathbf{k}$.

To model the center-of-mass momentum distribution of non-condensed pairs, we assume a Maxwell-Boltzmann distribution with an effective temperature T_p:

$$P(K_{\text{cm}}) = \left(\frac{\hbar^2}{4\pi k_b m T_p} \right)^{3/2} e^{-\frac{\hbar^2 K_{\text{cm}}^2}{4k_b m T_p}}, \tag{D.6}$$

where k_b is the Boltzmann constant and $\int_0^\infty P(K_{\text{rel}}) 4\pi K_{\text{cm}}^2 dK_{\text{rel}} = 1$. The product of the functions in equations D.6 and D.4 gives the transition probability as a function of $\mathbf{K}_{\text{cm}}$ and $\mathbf{k}_{\text{rel}}$. We change variables to $\mathbf{k}$ and $\mathbf{k}_{\text{rel}}$ and integrate over the angles to find the transition probability as a function of k and k_{rel}:

$$H(k, k_{\text{rel}}) = \frac{4\hbar^4}{\pi^{3/2} m^2} \sqrt{\frac{E_b}{k_b T_p}} \frac{k k_{\text{rel}} e^{-\frac{2\hbar^2(k^2 + k_{\text{rel}}^2)}{k_b m T_p}} \left(e^{\frac{\hbar^2(k + k_{\text{rel}})^2}{k_b m T_p}} - e^{\frac{\hbar^2(-k + k_{\text{rel}})^2}{k_b m T_p}} \right)}{(\hbar^2 k_{\text{rel}}^2/m + E_b)^2}, \tag{D.7}$$

where $\int_0^\infty \int_0^\infty H(k, k_{\text{rel}}) \mathrm{d}k \mathrm{d}k_{\text{rel}} = 1$. Finally, we change variables to E and k to derive the PES signal (equation 5.4 in the main text):

$$I_p(k, E) = \Theta\left(-E_p - E + k^2\right) \frac{8k\sqrt{\frac{E_p}{T_p}}e^{\frac{E_p + E - 3k^2}{T_p}}\sinh\left(\frac{2\sqrt{2}k\sqrt{-E_p - E + k^2}}{T_p}\right)}{\pi^{3/2}\left(E - k^2\right)^2} \quad . \tag{D.8}$$

In this last step, we also changed to dimensionless parameters (k, E, E_p, and T_p) normalized by k_F and E_F.